ABSTRACT

Title of Dissertation: ORIGIN OF THE ANOMALOUS SULFUR ISOTOPE COMPOSITION OF THE RUSTENBURG LAYERED SUITE (BUSHVELD COMPLEX), SOUTH AFRICA

Nivea Maria de Assis Magalhães, Doctor of Philosophy, 2019

Dissertation directed by: Associate Professor Sarah C. Penniston-Dorland
Professor James Farquhar
Department of Geology

The 2.06 Ga Bushveld Magmatic Province (BMP) hosts the largest platinum group element (PGE) reserve of the world that occurs mainly as sulfide-rich layers within the Rustenburg Layered Suite (RLS), and also in mineralized layers of the Waterberg Project (WP). Despite extensive studies, many questions remain on the origin and evolution of this large igneous province, and on the source of sulfur that allowed for the extensive PGE mineralization.

This study looks systematically into the multiple sulfur isotope composition of the RLS, finding that all layers show the presence of a mass-independently fractionated sulfur component ($\Delta^{33}S \neq 0$), which are all distinguishable from the expected $\Delta^{33}S$ value of the mantle. The exogenic sulfur reflects contamination by Archean surface-derived material (e.g. sediments, altered

oceanic crust). Such contamination can occur in many different stages of the evolution of these intrusions: either by assimilation of wall rock during ascent and emplacement, or in a staging chamber in the lower crust, or by recycling of crustal material in an ancient subduction zone.

The WP, an intrusion related to the BMP that was emplaced off-craton, has a similar sulfur composition to the Main Bushveld Series of the RLS. It is, however, a separate intrusion that crystallized in a separate magma chamber and was emplaced in a different unit than the RLS, which suggests that the contamination of the parental magma occurred at a deeper level, prior to emplacement of magma in the upper crust. Rocks from the Vredefort Dome, used as a proxy for the sulfur composition of the lower crust underneath that region, yield a sulfur composition that cannot account for the composition of the RLS or the WP. Finally, the sub-continental lithospheric mantle has been studied through xenoliths carried by the Premier Kimberlite. These xenoliths, such as what was observed in sulfide inclusions in diamond, also have $\Delta^{33}S \neq 0$, evidencing that the sub-continental lithospheric mantle may contain recycled sulfur that contributed this sulfur to primitive magmas during the Bushveld magmatic event.

ORIGIN OF THE ANOMALOUS SULFUR ISOTOPE COMPOSITION OF THE RUSTENBURG LAYERED SUITE (BUSHVELD COMPLEX), SOUTH AFRICA

by

Nivea Maria de Assis Magalhães

Dissertation submitted to the Faculty of the Graduate School of the
University of Maryland, College Park, in partial fulfillment
of the requirements for the degree of
Doctor of Philosophy
2019

Advisory Committee:
Associate Professor Sarah C. Penniston-Dorland, Chair
Professor Ahmet Aydilek, Dean's Representative
Dr. Richard W. Carlson
Professor James Farquhar
Professor Roberta L. Rudnick

Foreword

A portion of the research presented in this dissertation was previously published as a peer-reviewed journal article. I made substantial contributions to the relevant aspects of the jointly authored work included in this dissertation. Following is a summary of the contributions made by each author for the published paper.

Chapter 2.

Magalhães, N., Penniston-Dorland, S., Farquhar, J., Mathez, E.A. (2018) Variable sulfur isotope composition of sulfides provide evidence for multiple sources of contamination in the Rustenburg Layered Suite, Bushveld Complex. *Earth and Planetary Science Letters*. **492** 163-173. DOI: 10.1016/j.epsl.2018.04.010

I helped develop new techniques for sulfur measurements, performed all the analytical work, interpreted the data and wrote the manuscript. Dr. Penniston-Dorland contributed with experimental design, interpretation of the data, and assisted with writing of the manuscript. Dr. Farquhar helped with valuable knowledge of sulfur isotope techniques, interpreting the data, and assisted with writing. Dr. Mathez has collected the samples, and assisted with writing of the manuscript.

Acknowledgements

First and foremost, I would like to thank my advisors, Sarah Penniston-Dorland and James Farquhar, for their patience, support, and mentorship throughout my journey at University of Maryland. I am grateful for the opportunity to have worked with them, and to have learned so much from them, not only about sulfur isotopes in the Bushveld (and subduction zones on the side), but also about life. I truly appreciate all the dedication to provide me with the best conditions to do my research and all the opportunities that were given to me as part of this project. I also want to express my deep gratitude to Dr. Doug Rumble and Dr. George Cody, who kindly allowed me to spend time as a visiting investigator at the Geophysical Laboratory of the Carnegie Institution for Science, where I was able to collect a lot of really interesting data and experience the ins and outs of another work environment. I would also like to extend my appreciation to Dr. Richard Carlson and Dr. Roberta Rudnick for acting as members of my committee, and for all the very valuable advice given over the years. I thank Dr. Aydilek's role as the Dean's Representative in my committee.

This project has been supported by NSF grants EAR-1551196 (to S. Penniston-Dorland) and EAR-1461180 (to M. Feineman), GSA Student Grant (awarded to N. Magalhães), and a Science Without Borders Fellowship from the Brazilian government (BEX-1113/36-5). Funding for presentation of my research was also provided by the University of Maryland, both through the Earth System Science Interdisciplinary Committee (ESSIC) and the Goldharber Award.

I would like to thank Dr. Maureen Feineman and Dr. Grant Bybee for the opportunity to be a mentor at The Geochemistry School of the AfricaArray Project. It took a while, but I (think) finally convinced Maureen of my crazy ideas about sulfur in the mantle! Also, the memories of our fieldwork in South Africa always bring a smile to my face!

A huge thanks to Dr. Emma Bullock, who is probably one of the most welcoming and warm person I have met in this journey! Her smile made my time at the EPMA at Carnegie much brighter and happier.

Both of my research groups are thanked, in special Will Hoover, Kayleigh Harvey, James Dottin, Dr. Joost Hoek, Dr. Jabrane Labidi, for all the science discussions and for teaching me so

much about subduction zones and meteorites, and allowing me to vent when the mass spectrometer wouldn't properly work.

There are too many friends who have helped me through these years in the United States, far away from my home country. I would like to acknowledge a few by name, in no particular order: Bruna Fiume, Andrea Mundl, Leo Hund, Valentina Mazzotti, Kristel Izquierdo, Silvia Bachini, Miriam Sharp, Thays Nostre, Claudia Tokashiki, Franziska Weber, Claudia dos Santos, Thais Cardoso, Ana Carolina Kloth, Marianna Garcia, Scott Wipperfurth, Valeria Terence, Teresa Fornaro, and Mariana Burdelis. There are way too many people that came into my life (and some who are gone) that were essential for my growth. A huge shootout to my fellow graduate students and to the postdoctoral researchers at Carnegie Institution for Science, I loved beer hour and Mario Kart, and kayaking and drunk bodycombat in Halloween costumes. I hope wherever I end up, I always find such a happy bunch like you guys.

I would like to thank Dorothy Brown, Tood Karwoski, Suzanne Martin, Michelle Montero, and Joanna Patterson, for all the administrative help and technical support.

Mom, thanks so much for feeding the curiosity in that child that wanted to explore the world. Thank you for understanding that my journey would take me places far away from home. You believed in me more than I think I ever did. Thank you for the willingness to lend your ear for me to vent for hours on end even when you couldn't help me with anything but listen (Felix also listens, but he doesn't really have an option). A genuine thank you also to my little cousins Carolina and Gabriela, that are not so little anymore, because I know how much it hurt to see me leave and not knowing if I would ever come back to see them. Both of you are always in my heart.

Table of Contents

Foreword ii

Acknowledgements iii

Table of Contents v

List of Tables ix

List of Figures x

Chapter 1: Introduction 1

1.1. The Bushveld Magmatic Province 1

1.2. PGE Mineralization 4

1.3. Sulfur isotopes 6

1.4. Outline of dissertation 10

Chapter 2: Variable sulfur isotope composition of sulfides provide evidence for multiple sources of contamination in the Rustenburg Layered Suite, Bushveld Complex 12

2.1. Abstract 12

2.2. Introduction 13

2.3. Geological Background 16

2.3.1. The Rustenburg Layered Suite (RLS) 16

2.3.2. Isotope composition of the RLS 17

2.4. Methodology 20

2.4.1. Sulfide characterization 20

2.4.2. Sulfur extraction 20

2.5. Results 23

2.6. Discussion 27

2.6.1. Source of surface-derived sulfur in the RLS 31
2.7. Conclusions 41
Chapter 3: The sulfur composition of the Lower Bushveld Series 43
3.1. Abstract 43
3.2. Introduction 44
3.3. Background 45
3.3.1. The Clapham Section 45
3.3.2. Occurrence of anhydrite in mafic magmas 47
3.4. Methodology 50
3.5. Results 54
3.5.1. Petrography 54
3.5.2. Sulfur Isotopes 64
3.6. Discussion 71
3.6.1. Rationale for collection of Thode extracts 71
3.6.2. Sulfur isotope composition of the Lower Bushveld Series and its geological significance 75
3.7. Conclusions: Implications for sulfur source and processes occurring during emplacement of the RLS 81
Chapter 4. Multiple sulfur isotope composition of the Waterberg Project shows that upper crustal assimilation did not play a major role in magma contamination 84
4.1. Abstract 84
4.2. Introduction 85
4.3. The Waterberg Project 86
4.4. Methods 89
4.5. Results 90
4.6. Discussion 92

4.7. Conclusions 97

Chapter 5: Investigating the origin of anomalous sulfur in the Rustenburg Layered Suite, Bushveld Complex: the sub-continental lithospheric mantle as a potential source 99

5.1. Abstract 99

5.2. Introduction 100

5.3. The Premier Kimberlite 101

5.4. The Sub-Continental Lithospheric Mantle underneath the Kaapvaal Craton 104

5.5. Samples and Methods 105

5.5.1. Petrography and Mineral Chemistry 106

5.5.2. Sulfur Isotopes 106

5.6. Results 108

5.6.1. Petrographic Observations of selected samples 108

5.6.2. Sulfur Isotopes 117

5.7. Discussion 119

5.8. Conclusions 126

6. Conclusions 128

6.1. Overview 128

6.2. Summary 129

6.2.1. Chapter 2 129

6.2.2. Chapter 3 130

6.2.3. Chapter 4 131

6.2.4. Chapter 5 132

6.3. Future directions 132

Appendix A 136

Appendix B 152

References 158

List of Tables

Table 2.1. Sulfur Isotope Composition Of Bushveld Samples. 26

Table 2.2. Sulfur Isotope Composition Of Rocks From The Vredefort Dome. 36

Table 3.1. Mineral Composition Of Orthopyroxene From Samples Studied. Results Shown Here Correspond To Average Of All Measurements Of Orthopyroxene In A Sample (Total Amount Given By N). The Mg# Is Calculated Based On The Average Composition. 57

Table 3.2 Mineral Composition Of Clinopyroxenes From The Clapham Section. Results Shown Here Correspond To Average Of All Measurements Of Clinopyroxene In A Sample (Total Amount Given By N). Measurements Of Exsolved Cpx From Sample Ch7 49.59 Are Also Presented. 58

Table 3.3. Mineral Composition Of Plagioclase From The Clapham Section. Results Shown Here Correspond To Average Of All Measurements Of Plagioclase In A Sample (Total Amount Given By N). 59

Table 3.4. Composition Of Olivine From The Clapham Section. Results Shown Here Correspond To Average Of All Measurements Of Olivine In A Sample (Total Amount Given By N). 61

Table 3.5. Sulfur Isotope Composition Of Total Sulfide Extracts From The Clapham Core, Organized By Stratigraphic Depth. 68

Table 3.6. Sulfur Isotope Composition Of The Thode Extracts From The Clapham Core, Organized By Stratigraphic Depth. 69

Table 3.7. Sulfur Composition Of The Water-Soluble Sulfate From Bus Samples**.** 70

Table 3.8. Values Calculated For The $\Delta_{\text{thode Extract-Sulfide}}$ In Each Sample. 74

Table 4.1. Multiple Sulfur Isotope Data Of The Waterberg Project. 91

Table 5.1. Mineral Chemistry Data Of Olivine, Orthopyroxene, Clinopyroxene, And Garnet, From Peridotite Xenoliths From The Premier Kimberlite. 110

Table 5.2. Sulfide Mineral Chemistry Of Sample Phn5247. 113

Table 5.3. Multiple Sulfur Isotope Composition Of The Peridodite And Eclogites Xenoliths From The Premier Kimberlite, Along With Analyses Of Kimberlite Matrix Samples. 119

List of Figures

Figure 1.1. Map Of Bushveld Magmatic Province Igneous Bodies In The Context Of The Geography Of Sourthern Africa. The Vredefort Dome And The Premier Kimberlite Are Not Related To The Bmp, But Are Considered Locations Of Interest For This Thesis. Figure Adapted From Walker (2010). 2

Figure 1.2. Evolution Of $\Delta^{33}s$ Over Geological Time. Data Compilation By Johnston (2011). 10

Figure 2.1. Map Of The Bushveld Complex And Stratigraphic Column Of The Rls With The Approximate Location Of The Samples Used In This Study (After Penniston-Dorland Et Al., 2012). 16

Figure 2.2. Multiple Sulfur Isotope Composition Of The Rustenburg Layered Suite, Bushveld Complex, Compared To Uncontaminated Mantle Values Given By Morb Composition (Gray Rectangle; Data From Sakai Et Al., 1984; Chaussidon Et Al., 1991; Peters Et Al., 2010). Grey Diamonds Represent Data From This Study, While White Triangles Are Critical And Main Zones Samples Studied In Penniston-Dorland Et Al. (2012). Select Northern Limb Samples (Black Circles) Were Also Plotted For Comparison (Penniston-Dorland Et Al., 2008). Error Bars Are 2σ Uncertainty. 25

Figure 2.3. Variation Of The $\Delta^{33}s$ Composition According To Stratigraphic Position. Error Bars Are 2σ Uncertainty. 28

Figure 2.4. Diagram Comparing The Sulfur Δ33s Composition Of The Rustenburg Layered Suite With Previously Existing Data For Other Isotope Systems. A Relationship Between The Isotope Composition Of Sulfur, Strontium, And Neodymium Can Be Seem As Shifts In Composition Are Related To Stratigraphy. Oxygen Isotope Values Do Not Present A Correlation To The Other Systems. Values Of (87sr/86sr)I Were Plotted After Kruger (2004), End Data After Maier Et Al. (2000), And Δ18o Data After Harris Et Al. (2005). 29

Figure 2.5a. Multiple Sulfur Isotope Composition Of The Transvaal Supergroup Rocks Located At The Transvaal Basin (+) Compared To The Rustenburg Layered Suite (Data From Penniston-Dorland Et Al. 2008, Guo Et Al. 2009) And Vredefort Dome Sulfur Isotope Composition, As Seen In Figure 2.5b. The Sedimentary Rocks Show A Highly Variable Composition, Both In $\Delta^{34}s$ And $\Delta^{33}s$, Compared To The Igneous Rocks Of The Rls And The Metamorphic Rocks Of The Vredefort Dome. 33

Figure 2.5b. Composition Of The Vredefort Dome (Squares, Other Symbols As In Figure 2.2) Rocks Compared To The Rustenburg Layered Suite (This Study; Penniston-Dorland Et Al, 2008; 2012), And The Uncontaminated Mantle Composition (Morb Data, Sakai Et Al., 1984, Chaussidon Et Al., 1991; Peters Et Al., 2010). All The

Δ^{33}s Values Of The Vredefort Dome Rocks Are Lower Than The Maximum Values Of The Rls, Which Suggests That These Rocks Are Not End Members Of Mixing With Magma With Uncontaminated Mantle Composition. Error Bars Are 2σ Uncertainty. 36

Figure 3.1. (A) Location Of The Study Area Within The Country Of South Africa; **(B)** Location Of The Boreholes Ch6 And Ch7, Where The Samples In This Study Were Collected. 47

Figure 3.2. Detailed Stratigraphy Of The Drill Cores Ch6 And Ch7, Showing Their Lithologies And Unit Subdivision. White Circles Correspond To Samples Analyzed. The Floor Rock Is The Magaliesberg Quartzite Of The Pretoria Group (Transvaal Supergroup). Sketched After Wilson, 2015. 49

Figure 3.3. Mineral Composition Of The Studied Samples From The Clapham Core. This Figure Does Not Present Modal Percentages, And The Variation In The Amount Of Each Mineral Between Samples Is Not Portrayed. 54

Figure 3.4. A. Wo-En-Fs Classificatory Diagram For Pyroxenes From Drill Core Ch7. B. Variation Of Mg# With Depth In Orthopyroxene (Blue Circle) And Olivine (Green Square). 56

Figure 3.5. A. An-Ab-Or Classificatory Diagram For Feldspar Shows Two Distinct Groups Of Feldspar: The Predominant Is Plagioclase; The Ca-Rich Variety. In A Lesser Amount, K-Feldspar (Orthoclase) Is Also Present. **B.** Ca-Na-K Compositional Map Of Feldspar From Sample Ch7 1108.46, Showing A "Euhedral" Ca-Rich Core, With Strong Zoning Filling In For The Interstitial Spaces, Where An "Anhedral" Na-Rich Rim Formed. 56

Figure 3.6. A. Scan Of Thin Section Ch7 708.24, Where It Is Possible To See Cumulate Olivine Enclosed By Biotite; **B.** Cumulate Olivine In Sample Ch7 580.51, Where The Intercumulus Material Is Clinopyroxene. 61

Figure 3.7. Images Showing Diverse Anhydrite Textures Observed In Samples Ch7 970.00 And Ch7 1108.46. **3.7a.** Coexisting Sulfides And Anhydrite; **3.7b.** Fe-Ni-S-Cu-Ca Compositional Map Of The Coexisting Sulfide And Anhydrite From Figure A; **3.7c.** Pyrite Grains Growing On The Rim Of An Anhydrite Crystal, **3.7d.** Inclusion Of Anhydrite In Zoned Orthopyroxene; **3.7e.** Sulfide Aggregate With Magnetite In The Core; **3.7f**. Anhydrite Associated With Apatite. 63

Figure 3.8. Sulfur Isotope Composition Of Total Sulfide, Thode Extract, And Soluble Sulfate Obtained For Samples Of The Clapham Core. The Mantle Field Was Determined With Data From Sakai Et Al. (1983), Peters Et Al.

(2010) And Labidi Et Al. (2012). Main Bushveld Series Data Recalculated From Penniston-Dorland Et Al. (2012) And Magalhães Et Al. (2018) (Appendix A). 66

Figure 3.9. A) Variation Of $\Delta^{34}s$ With Stratigraphic Depth Of The Clapham Core. **B.** Variation Of $\Delta^{33}s$ With Stratigraphic Depth. Grey Rectangle Corresponds To The Mantle Value (Sakai Et Al., 1983; Labidi Et Al., 2012). Values For $\Delta^{34}s$ And $\Delta^{33}s$ Are In The Permil (‰) Unit. 67

Figure 3.10. Venn Diagram Exemplifying The Overlap Between Phases Containing Different Sulfur Species (Sulfide, Sulfate) And What Is Extracted By Each Method. Note That The Thode Extracts Intersect Both Fields For Water-Soluble Sulfate And Chromium Reducible Sulfur, With The Potential To Extract Almost All The Phases In A Sample. 73

Figure 3.12. Variation Of $\Delta^{33}s$, $\Delta^{34}s$ And $^{87}sr/^{86}sr_{(I)}$ With Depth In The Clapham Section. The $^{87}sr/^{86}sr_{(I)}$ Data Are In-Situ Measurements In Plagioclase From Wilson Et Al. (2017). 76

Figure 3.13. Comparison Of The $\Delta^{34}s$ Values For Total Sulfide, Thode Extracts, And Water-Soluble Sulfate. 80

Figure 4.1. Geological Map Of The Northern Limb Of The Rustenburg Layered Suite, Evidencing The Location Of The Waterberg Project (Does Not Crop Out). The Stratigraphic Column Of The Wp Is Described On The Right, With Emphasis On The Mineralized Zones F And T. Figure From Matthew Mccreesh. 88

Figure 4.2. Multiple Sulfur Isotope Composition Of The Waterberg Project (Red Circles), And Its Host Rock, A Sulfur-Rich Granofels (Green Circle). The Orange Field Denotes The Range Of Compositions For The Rls (Penniston-Dorland Et Al., 2012; Magalhães Et Al., 2018), While The Gray Rectangle Represents The Composition Of Sulfur From Mantle-Derived Morb Glass (Labidi Et Al., 2012; 2013; 2014; Labidi And Cartigny, 2015). Error Bars Are 2σ. 90

Figure 4.3. Variation Of The Sulfur Isotope Composition Of The Waterberg Project In The Context Of Stratigtaphic Column (Error Bar Is 0.016‰, 2σ). 94

Figure 4.4. Mixing Calculations Of Sulfur And Oxygen Isotope Compositions Between Three Distinct Reservoirs: Mantle, And Granitoid And Metasediments From The Vredefort Dome. Rustenburg Layered Suite Data Is Plotted As Blue Diamonds. Mantle Composition As Obtained By Labidi Et Al. (2014) For Sulfur, And Muehlenbachs And Clayton (1976) For Oxygen. Oxygen Data Of The Vredefort Dome Was Estimated From Fagereng Et Al., 2008, And The Rls Was Extracted From Harris Et Al. (2005). The Sulfur Isotope Data Was Obtained By Penniston-Dorland Et Al. (2012) And Magalhães Et Al. (2018). 96

Figure 5.1. Map Of Southern Africa Showing The Location Of The Kaapvaal-Zimbabwe Craton And Location Of The Premier Kimberlite (White Circle). Other Kimberlite Intrusions Are Jwaneng,, Orapa, And Venetia. The Green Area Reflects The Extent Of The Bushveld Magmatic Province. Figure Sketched After Richardson And Shirey, 2008. 105

Figure 5.2. Different Textures Observed In Peridotite Xenolith Samples. 5.2a. Hand Sample Of The Sample Frb1655 (Spinel Harzburgite), With Large Crystals And Little Deformation; **5.2b.** Hand Sample Of Sample Frb1309 (Garnet Lherzolite), Displaying More Fine Grained Minerals, With Little Deformation; **5.2c.** Sample Phn5247 (Spinel Harzburgite) With Coarse Grain Size, Without Evidence For Ductile Deformation Or Significant Serpentinization, Plane Polarized Light. **5.2d.** Statically Recrystallized Grains Of Olivine Form The Matrix Of This Sample, Which Also Have Large Orthopyroxene And Garnet Porphyroclasts, Plane Polarized Light (Sample Phn5239, Garnet Harzburgite). 109

Figure 5.3.A. Sulfide Grain In Sample Phn5247 (Spinel Harzburgite) Consists Of An Association Of Pentlandite And Pyrrhotite, Which Are Being Altered Into Magnetite. **3b.** Close Up Look At The Association Between Pyrrhotite (Medium Gray), Pentlandite (Lighter Grey), And Magnetite (Darker Gray). **3c And 3d:** Compositional Map Of Sulfides From Sample Phn5247, Showing The Textural Relationships Between Pentlandite, Pyrrhotite, Magnetite, And Chalcopyrite (When Present). Pentlandite Is Also Being Exsolved From Pyrrhotite. 112

Figure 5.4 Images Of Sulfides From Sample Frb 1309 (Garnet Lherzolite). **A.** Bse Image Of Pseudo-Sulfide Shape, Surrounded By Serpentine, Which Is Now An Aggregate Of Sulfides Surrounded By Serpentine. **B.** Bse Image Of Sulfide (Brighter Regions) Surrounded By Magnetite, Which Implies A High Degree Of Oxidation And Loss Of Sulfur; **C.** Compositional Map Of Sulfides From Figure 5.A. A Closer Look At This Grain Shows A Multi-Component Assemblage, With Magnetite (Red), Heazlewoodite (Cyan), And Chalcopyrite (Blue).**D.** Compositional Map Of Sulfide From Sample 5b. Red Colors Showing The Magnetite Surrounding The Heazlewoodite (Cyan). The Blue Spot Is Chalcopyrite**.** 114

Figure 5.5. A. Eclogite Hand Sample Frb 908d2, Sulfide Within Garnet Crystal **B.** Eclogite Hand Sample Frb 908d2. **C**. Bse Image Of Pyrite Grain With Inclusions Of Matrix Minerals (Dark Spots) And Other Sulfides, Such As Galena (Bright Spots) **D.** Bse Image Of Interstitial Pyrite With No Inclusions Or Association With Other Sulfides. 115

116

Figure 5.6. A. Photograph Of Hand Sample Frb1367-21. Note The Lack Of Large Crystals; **B.** Photograph Of Hand Sample Frb 900c2, Where It Is Possible To Distinguish A Large Crystal That Has Been Replaced By Serpentine. 116

Figure 5.7. Diagram Of $\Delta^{34}s$ Versus $\Delta^{33}s$ Showing Sulfur Isotope Composition Data Of Sulfides From The Matrix And Peridotite (Green Circle), Eclogite (Blue Circle), And Matrix Of The Premier Kimberlite (Red Circles). The Green Field Denotes The Known Composition Of The Lower Bushveld Series In The Clapham Section (Chapter 3), The Yellow Area Denotes De Composition Of The Main Bushveld Series (Chapter 2), And The Blue Area Corresponds To The Composition Of The Waterberg Project (Chapter 4). Sulfur Isotope Composition Of The Unaltered Mantle (Peters Et Al., 2010; Labidi Et Al., 2012) Is Represented By A Dotted Box. 118

Figure 5.8. Mixing Calculation Between S And Os For Different Reservoirs. E-Type Sulfide Inclusions (Out Of Picture, Farquhar Et Al., 2001; Richardson And Shirey, 2008) And Peridotite Xenoliths (Green Star, Carlson Et Al., 1999; This Study) Were Evaluated As Possible Compositional End Members For A Starting Composition Similar To A Mantle Melt (Yellow Star, Labidi Et Al., 2014; Meisel Et Al., 1996). The Blue Diamonds Correspond To Samples From The Critical Zone Of The Rls (Schoenberg Et Al, 1999; Magalhães Et Al., 2018). 125

Chapter 1: Introduction

1.1. The Bushveld Magmatic Province

Large igneous provinces (LIP) are short duration (< 5Ma) magmatic events that inject a high volume of magma (> 0.1Mkm^3; Bryan and Ernst, 2007), into the crust. These processes are not related to plate boundary processes (such as subduction), and the mechanism of formation remains uncertain, with mantle plume (Richards et al., 1989; Campbell, 2007) and lithospheric delamination (Elkins-Tanton et al., 2005) being proposed as possible models. Their distribution in time is widespread, but older examples tend to be not as well preserved. Some large magmatic provinces have been associated with both mass extinction events (Wignall, 2001; Ernst and Youbi, 2017), and mineral deposits (Mekhonoshin et al., 2016).

The Bushveld Magmatic Province (BMP) is a large igneous province that comprises a group of intrusive and extrusive bodies of similar age that outcrop in Southern Africa. This LIP intruded the Kaapvaal Craton around 2.06-2.05 Ga (Zeh et al., 2015), and encompasses mafic-ultramafic suites, felsic rocks and a carbonatite. It extends over a large geographic area, from Botswana (Molopo Farms Complex) in the west, to the border between South Africa and Mozambique (Phalaborwa Carbonatite Complex) to the east (Figure 1.1). The BMP is thought to have formed from a mantle plume (Hatton, 1995; Wilson et al., 2017), given the volume of magma emplaced and the estimated ultramafic composition of the parental magma (Wilson et al., 2017).

The most famous intrusion of the BMP is the Rustenburg Layered Suite (RLS) due to its reserves of platinum group elements (PGE). The RLS is a mafic-ultramafic layered intrusion that

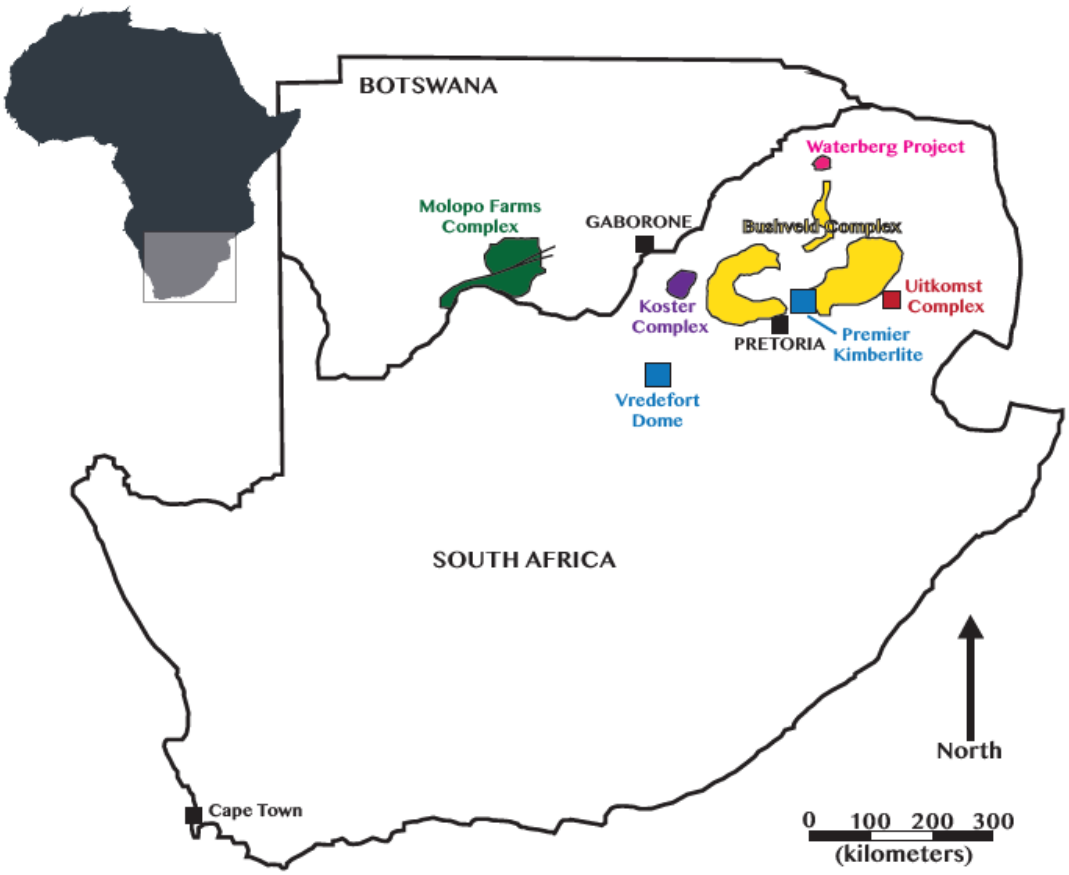

Figure 1.1. Map of Bushveld Magmatic Province igneous bodies in the context of the geography of Sourthern Africa. The Vredefort Dome and the Premier Kimberlite are not related to the BMP, but are considered locations of interest for this thesis. Figure adapted from Walker (2010).

has been studied since the beginning of the 20th century (Wagner, 1929). It covers an area in excess of 65,000 km^2, twice the size of the state of Maryland, and its volume has been estimated to reach up to 650,000 km^3 (Cawthorn and Walraven, 1998). The RLS is spatially associated with the Rooiberg Volcanics, Rashoop Granophyres and Lebowa Granite Suite, and together constitute what is known as the Bushveld Complex. Both informally and in the literature, the terms Bushveld or Bushveld Complex have been used to refer to the mafic-ultramafic

counterpart (RLS), given its predominant importance over the other suites. In this thesis, these terms will not be used interchangeably.

The intrusion has five different limbs, denominated Eastern, Western, Southern, Northern, and Far Western (also known as Koster Complex). Connectivity between the Eastern and Western limbs has been suggested by Cawthorn and Webb (2001), but still remains controversial. The RLS can be divided in the Lower Bushveld Series and Main Bushveld Series (Wilson et al., 2017). The first encompasses the Basal Ultramafic Sequence, the Marginal Zone, and the Lower Zone, which represent the earlier magmas of the intrusion. The Main Bushveld Series contains the Critical Zone, Main Zone, and Upper Zone. There is still a lack of consensus on major questions about the RLS origin and evolution, such as how this intrusion was emplaced (Kruger, 2005; Mungall et al., 2016), the source of contamination (McCandless et al., 1999; Maier et al., 2000; Zirakparvar et al., 2014; Magalhães et al., 2018), and competing hypotheses over the composition of parental magmas (Maier et al., 2000; Wilson et al., 2017).

The other intrusion that this thesis will focus on is the Waterberg Project (WP), a newly described intrusion situated in the southern margin of the Limpopo Belt (Huthmann et al., 2016; Kinnaird et al., 2017). The WP was discovered recently through a combination of geological and geophysical surveys, and although its 2.05 Ga age and geochemistry link it to the BMP (Huthmann et al., 2018), it is inferred to be a completely separate intrusion from the RLS (Kinnaird et al., 2017; Huthmann et al., 2018). The WP is also a PGE mineralized body, with two distinct mineralized layers, but the mineralization has different characteristics compared to the RLS (McCreesh et al., 2018).

1.2. PGE Mineralization

The RLS PGE reserves represent 75% of the known PGE reserves in the world. The ore occurs as a concentration of PGE-rich sulfides in a few layers within the intrusion, such as the Merensky Reef, UG2 chromitite, both located in the Upper Critical Zone, and the Platreef, which occurs exclusively in the Northern Limb.

Sulfur is essential in the concentration of PGEs because of its role in PGE geochemistry. Sulfur saturation in a magma and formation of an immiscible sulfide liquid are called upon by most models that seek to explain the PGE reserves. This sulfide immiscible liquid would interact with large quantities of silicate magma and "extract" the PGE from the magma (Campbell et al., 1983, Mavrogenes and O'Neill, 1999). In some models, the sulfur necessary for the saturation results from assimilation of the country rock. The Transvaal Supergroup, composed of sedimentary rocks with variable age from 2.6 to 2.0 Ga (Lenhardt et al., 2012) is the country rock for the Bushveld Complex and is therefore regarded as a potential source of crustal material possibly assimilated by the RLS. In other models the final concentration of PGEs is caused by other processes, such as the migration of late fluids (Boudreau and McCallum, 1992) or sulfide self-destruction (Kerr and Leitch, 2005), but these models still call for an earlier stage of sulfur saturation to occur within the magma.

In this thesis, information from the four stable sulfur isotopes is used to evaluate the sources of sulfur and processes that fractionate sulfur in the various parts of the BMP. Two measures are used, $\delta^{34}S$, which describes the variations of $^{34}S/^{32}S$, and $\Delta^{33}S$ which describes the deviation of $\delta^{33}S$ from the expected terrestrial fractionation line. This approach allows for one to identify the presence of anomalous Archean sulfur by using $\Delta^{33}S$, and builds upon previous studies that only focused on $\delta^{34}S$ (Buchanan et al., 1981). Hypotheses constructed in the prior

studies using only $\delta^{34}S$ led to the conclusion that evidence for surface-derived sulfur was lacking. Thus, while surface-derived sulfur was required by some of the ore genesis models, it was generally inferred that all sulfur would come from a pristine, mantle source. Tracing $\Delta^{33}S$, as is done here, provides an additional window into sulfur that allows for better tracing of the signature of Archean exogenic sulfur (sedimentary, or derived from other rocks that interacted with mass-independently fractionated sulfur from Archean oceanic and atmospheric reservoirs).

Penniston-Dorland et al. (2008) used multiple sulfur isotopes to evaluate the magma-country rock interaction at the Platreef, a PGE-rich layer in the Northern Limb. In that location, there is clear evidence for interaction between the magma and the country rock, and many studies postulated that this would have caused the sulfur saturation and subsequent precipitation of the PGE-rich layer (Buchanan et al., 1981; Sharman-Harris et al., 2005). However, that study showed that while there is, indeed, interaction between the magma and the sediments of the Transvaal Supergroup, there is evidence for fluid transport and advection into the host rock (i.e. from the intrusion rather than into the intrusion). A second finding was that the Archean exogenic component did not disappear deeper within the RLS, further away from the contact. This result opened up the possibility that the primary magmatic sulfur composition of the RLS was not what we consider mantle-like.

Penniston-Dorland et al (2012) explored this further, aiming to understand if other parts of the intrusion had this same signature. They observed that samples from the UG2 layer and a few samples of the Critical and Main Zones, collected in the Eastern and Western Limbs, also had this seemingly uniform value of sulfur isotopic composition. In this line of thought, further work was then necessary to understand very basic questions on whether this signature was homogeneous within the intrusion or even if it was present in the other layers.

1.3. Sulfur isotopes

Sulfur (S) is a non-metal with atomic number equals to 16. Sulfur has twenty-five known isotopes, but only four of them are stable, with mass 32, 33, 34 and 36. Their natural abundances are: ^{32}S 95.02%, ^{33}S 0.75%, ^{34}S 4.21%, and ^{36}S 0.02% (Coplen *et al.*, 2002). It behaves as a chalcophile element; for this reason it is possible that most of the sulfur is currently located in Earth's core, which makes it difficult to estimate its concentration in the bulk Earth (McDonough & Sun, 1995). There is a range of sulfur contents reported for fertile mantle; from values less than 100 ppm to values up to 300 ppm (Mitchell & Keays, 1981; Garuti *et al.*, 1984; Lorand, 1990). Mid-Ocean ridge basalt (MORB) analyses are consistent with higher values and suggest an upper-mantle value of 250±50 ppm (McDonough & Sun, 1995). However, metasomatic processes might increase the amount of S in the mantle wedge up to ~500ppm (de Hoog *et al.*, 2001).

Sulfur occurs with oxidation states from -2 to +6 (S^{2-}; S^0; SO_2; SO^{-2}_4). It is introduced as sulfur dioxide and hydrogen sulfide and other S-bearing gases to the atmosphere; it accumulates as sulfate in the oceans; and it is an important mineral-forming element in sedimentary, metamorphic, and igneous rocks. In a magma, sulfur partitions between water-rich volatile phases and sulfur-bearing minerals, in either sulfide and/or sulfate form (Fincham and Richardson, 1954). The transition between sulfide-dominated to sulfate-dominated systems occurs in a narrow oxygen fugacity interval, close to FMQ buffer conditions (Jugo *et al.*, 2005; Jugo, 2009). Oxidized and high water content basaltic magmas can carry up to 1.5 wt% of sulfate (Jugo *et al.*, 2005), while in reduced magmas the saturation of sulfur depends on the concentration of an immiscible Fe-S-O melt phase, which is controlled by temperature and quantity of Fe in the melt (Liu *et al.*, 2007).

The sulfur cycle can be tracked using isotope measurements. Urey (1947) and Bigeleisen and Mayer (1947) were the first to describe the thermodynamic basis for isotope partitioning (fractionation). When the first-order control on isotopic fractionation relates directly to the role of mass in partitioning of energy (chemical or physical), isotopic fractionations are referred to as mass-dependent fractionation (MDF). Both equilibrium and kinetic isotope effects can be mass-dependent. However, they can also reflect contributions to the partition function from factors other than mass (e.g. nuclear radius, nuclear spin, factors that influence rates of state-to-state transitions in reaction kinetics) and are then referred to as mass-independent.

The equilibrium isotope effect derives from the exchange of isotopes between two coexisting phases (e.g. pyrite and chalcopyrite) when reactions are fully reversible and free energy associated with isotopic substitution is minimized. Isotope partitioning is analogous to element partitioning between two or more different minerals. For sulfur, free energy differences associated with isotopic substitution arise because of the effect of mass on vibrational, translational and rotational motions of sulfur atoms and groups in different materials. Equilibrium constants are temperature-dependent, and isotopic fractionations are generally more prominent at low temperature.

Kinetic isotope effects stem from a physical phenomenon where reaction rates depend on isotope composition (e.g. $C^{16}O_2$ and $C^{18}O_2$ may react at different rates because the C - ^{18}O bond is stronger than the C - ^{16}O bond); in many cases the molecule containing the lighter isotope reacts more quickly because the difference in zero point energy between the reactant state and the transition state is smaller, and this affords a rate advantage.

The sulfur isotopic composition of materials are reported using the delta (δ) notation, which is reported with reference to the ^{32}S isotope (equations 1.1 to 1.3):

$$\delta^{33}S = \left[\frac{\left(\frac{^{33}S}{^{32}S}\right)_{sample}}{\left(\frac{^{33}S}{^{32}S}\right)_{V-CDT}} - 1\right] \quad (1.1)$$

$$\delta^{34}S = \left[\frac{\left(\frac{^{34}S}{^{32}S}\right)_{sample}}{\left(\frac{^{34}S}{^{32}S}\right)_{V-CDT}} - 1\right] \quad (1.2)$$

$$\delta^{36}S = \left[\frac{\left(\frac{^{36}S}{^{32}S}\right)_{sample}}{\left(\frac{^{36}S}{^{32}S}\right)_{V-CDT}} - 1\right] \quad (1.3)$$

where the values are expressed in permil (‰). Note that the factor of 1000 is omitted following IUPAC recommendation and the 1000 is included with the permil symbol.

Mass-independent fractionation (MIF), on the other hand, is a process where the fractionation observed cannot be explained solely by the difference in isotope masses and hence deviates from the expected values defined by MDF. It is less common, and can be a product of photochemical (Farquhar et al., 2001) or spin-forbidden reactions (Turro, 1983). These anomalies are quantifiable in terms of a capital delta (Δ) notation (equations 1.4 and 1.5):

$$\Delta^{33}S = \delta^{33}S - [(1 + \delta^{34}S)^{0.515} - 1] \quad (1.4)$$

$$\Delta^{36}S = \delta^{36}S - [(1 + \delta^{34}S)^{1.9} - 1] \quad (1.5)$$

which describe the deviation of a $\delta^{33}S$ (or $\delta^{36}S$) from a mass dependent reference frame defined by the $\delta^{34}S$. The capital delta is also described in permil and the factor of 1000 is not included in this definition.

The distribution of sulfur with different isotopic characteristics ($\delta^{34}S$, $\Delta^{33}S$ and $\Delta^{36}S$) in different terrestrial reservoirs has been documented by numerous studies of the past decades. Farquhar et al. (2000) recognized mass-independent fractionation of sulfur in the geological record preserved in metasedimentary rocks of Archean/Early Proterozoic age. Sedimentary rocks that are older than ~2.4Ga usually show a distinct mass-independent fractionation signature for sulfur isotopes, while younger rocks lack it (Figure 1.2). The interpretation for such abrupt change correlates the rise of oxygen in the atmosphere to the disappearance of MIF from the record (Farquhar et al., 2000; Pavlov & Kasting, 2002; Johnston, 2011; Halevy, 2013). Farquhar et al. (2000) noted that the reason for the disappearance of the MIF signal as the atmosphere composition became more oxidizing was that photochemical reactions involving SO_2 that previously took place in the atmosphere were not possible in an oxygen-rich atmosphere. Pavlov and Kasting (2002) extended this connection to the way that atmospheric oxygen levels affect how sulfur exits the atmosphere. At low oxygen levels, a second channel for deposition of zero-valent sulfur emerges that allows for the mass independent signal to be effectively transferred to surface environments. The transfer of sulfur to the rock record occurs via pyrite formation processes (e.g., Ono et al., 2003; Farquhar et al., 2013; Rickard et al., 2017) and hydrothermal reactions that form sulfate minerals or reduce sulfate to sulfide (e.g., Ueno et al., 2009). Transfer of mass independent sulfur from surface reservoirs to deeper mantle reservoirs has been inferred from sulfide inclusions in diamond (Farquhar et al., 2002; Thomassot et al., 2009) and from ocean island basalts containing HIMU and EMI components (Cabral et al., 2013; Delavault et al., 2016).

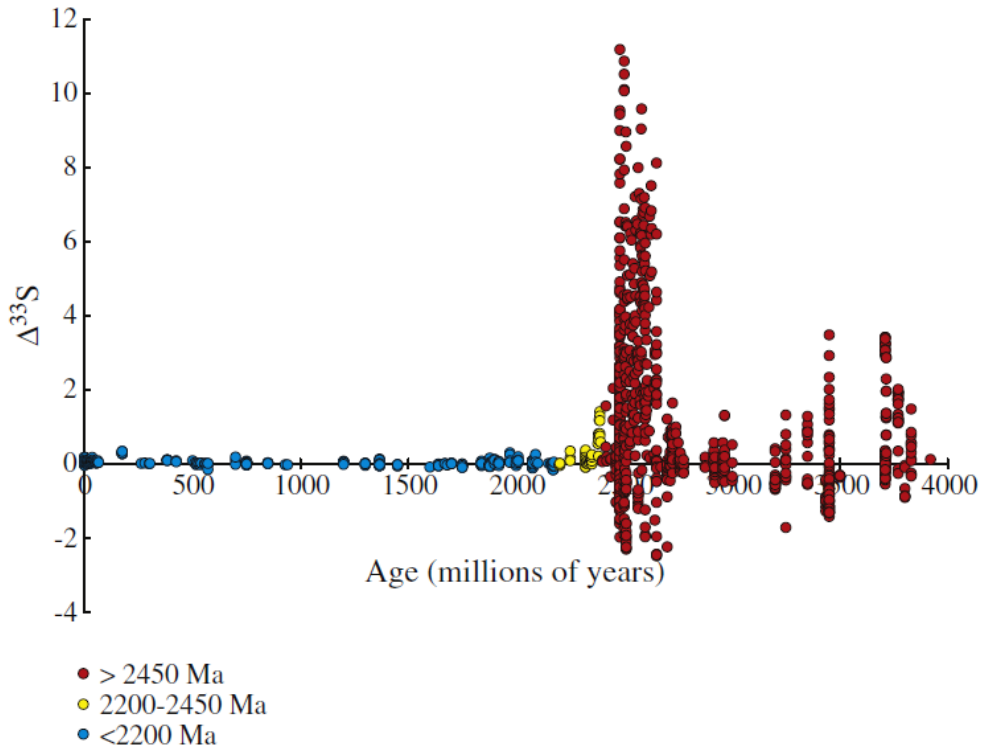

Figure 1.2. Evolution of $\Delta^{33}S$ over geological time. Data compilation by Johnston (2011).

1.4. Outline of dissertation

The primary aim of this thesis is to answer questions regarding the source of anomalous sulfur in the Rustenburg Layered Suite. Insights on the sulfur composition can provide information on which stage of the RLS evolution the contamination occurred, which materials are likely to have been the source of the sulfur, and whether any PGE formation model can be favored. This work also provides a window to understand questions related to the shallow mantle underneath the continents (sub-continental lithospheric mantle).

This dissertation is divided into 6 chapters and appendices A-B. Chapter 2 addresses basic questions on whether anomalous sulfur is present in the Main Bushveld zones, and assesses whether there is variability of the sulfur isotopic composition in different layers, such as what is

seen in radiogenic isotope systems. Chapter 3 gathers mineral chemistry and sulfur isotope data for the Lower Bushveld Series, which is a newly described portion of the RLS that might represent the first magmas of this intrusion. This chapter aims to evaluate the story of these most primitive magmas and how those relate to the information described in Chapter 2, for a more global view of the RLS. A discussion on practices for sulfur measurement in rocks is also presented. Chapter 4 will argue that the anomalous sulfur in the RLS is not a result of upper crustal contamination by looking at the Waterberg Project, a genetically related intrusion that is hosted by a different country rock. Chapter 5 describes peridotite and eclogite xenoliths from the Premier Kimberlite to evaluate whether the sub-continental lithospheric mantle could be a source of anomalous sulfur for the RLS. Chapter 6 summarizes the work presented and discusses remaining outstanding questions and future directions for research.

Appendix A consists of the raw mineral chemistry data obtained for Chapter 3 and of backscattered electron (BSE) images of mineral textures that were not essential for the main text. Appendix B consists of BSE images of mineral textures in xenoliths and kimberlite matrix, particularly focusing on the sulfide minerals.

Chapter 2: Variable sulfur isotope composition of sulfides provide evidence for multiple sources of contamination in the Rustenburg Layered Suite, Bushveld Complex

2.1. Abstract

The Rustenburg Layered Suite (RLS) of the Bushveld Complex (BC) is famous for its platinum group element (PGE) ore, which is hosted in sulfides. The source of sulfur necessary to generate this type of mineralization is inferred to be the host rock of the intrusion. The RLS has a sulfur isotopic signature that indicates the presence of Archean surface-derived material ($\Delta^{33}S \neq 0$) in the magma. This signature, with an average value of $\Delta^{33}S = 0.112 \pm 0.024$‰, deviates from the expected $\Delta^{33}S$ value of the mantle of 0 ± 0.008‰. Previous work suggested that this signature is uniform throughout the RLS, which contrasts with radiogenic isotopes which vary throughout the igneous stratigraphy of the RLS.

In this study, samples from key intervals within the igneous stratigraphy were analyzed, showing that $\Delta^{33}S$ values vary in the same stratigraphic levels as Sr and Nd isotopes. However, the variation is not consistent; in some levels there is a positive correlation and in others a negative correlation. This observation suggests that in some cases distinct magma pulses contained assimilated sulfur from different sources. Textural analysis shows no evidence for late addition of sulfur. These results also suggest that it is unlikely that large-scale assimilation and/or efficient mixing of host rock material in a single magma chamber occurred during emplacement.

The data do not uniquely identify the source of sulfur in the different layers of the RLS, but the variation in sulfur isotope composition and its relationship to radiogenic isotope data calls

for a reevaluation of the models for the formation and evolution of the RLS, which has the potential to impact the knowledge of how PGE deposits form.

2.2. Introduction

Platinum group elements (PGEs) are of significant economic importance due to their technological application. The Paleoproterozoic Rustenburg Layered Suite (RLS) of the Bushveld Complex (BC) is the world's largest mafic-ultramafic layered intrusion, and it is host to the largest reserves of platinum group elements (PGEs) on Earth. Although it has been the subject of many petrologic, geochemical and geophysical studies, many questions remain on the origin and evolution of this fascinating intrusion and its PGE-rich layers.

The enrichment of PGEs in the ore horizons of the Bushveld has been explained by a variety of models that generally involve exchange of sulfide-rich horizons with large volumes of silicate melt in either closed-system magma chamber or open-system magma conduit environments (e.g. Campbell et al., 1983; Mavrogenes and O'Neill, 1999; Kerr and Leitch, 2005). Therefore, sulfur can be a powerful tool to investigate the source and timing of crustal contamination in the RLS, which has a direct impact on assessing the formation of sulfide-hosted PGE ore. The Transvaal Supergroup, a 2.6-2.0 Ga sequence of sedimentary and volcanic rocks in the Kaapvaal Craton (Walraven, 1997), is usually considered a source for the sulfur in the intrusion and therefore plays a part in precipitation of PGE sulfides.

Mass independent fractionation (MIF, $\Delta^{33}S \neq 0$) of sulfur isotopes was widespread during the Archean, as the anoxic atmosphere on early Earth facilitated the occurrence of photochemical reactions that produced it (Farquhar et al., 2001). The production of MIF ended after the Great

Oxidation Event (GOE) at approximately 2.4 Ga, and its presence in rocks, particularly those with ages younger than the GOE, has been associated with an Archean surface material component. This MIF is not known to result from mass-dependent magmatic processes; and for this reason any MIF present in the RLS should be a direct result of assimilation of materials with a surface-derived signal, such as the aforementioned sedimentary rocks from the Transvaal Supergroup.

The current hypothesis for the origin of the RLS infers a mantle source for its parental magmas, which may have originated from a plume (Hatton, 1995; Wilson, 2012), and are not expected to carry any MIF signature. The method of emplacement in the crust is still debated; evidence for sill-like, out-of-sequence emplacement comes from U-Pb geochronology (Mungall et al., 2016), in opposition to crystal deposition in a constantly replenished magma chamber (Kruger, 2005, and references therein). A variety of different isotopic signatures provide evidence for crustal contamination of the magmas, including high $(^{87}Sr/^{86}Sr)_i$ and low ε_{Nd} values observed throughout the stratigraphy of the RLS (Kruger, 2005; Maier et al., 2000; and references therein). The Os isotopic composition is more radiogenic than expected for magmas with a mantle component (e.g., McCandless et al., 1999), and the Hf isotopic compositions also cannot be explained using the depleted mantle model (Zirakparvar et al., 2014). However, the timing and the source of contamination remain largely unconstrained. Lead isotope analysis in plagioclase and sulfides point to a complex evolution of the system, with both minerals not recording the original Pb isotopic composition of the parent magmas (Mathez and Waight, 2003).

Stable isotope systems also point to an interaction between the magmas and a material with a crustal signature (Harris et al., 2005; Penniston-Dorland et al., 2008; 2012). Whereas

radiogenic isotope signatures vary throughout the intrusion in a systematic and correlatable fashion, which is thought to reflect different magma pulses and/or different sources of contamination, there is no discernible systematic change in the values of the calculated oxygen isotope composition of the magma. This lack of variation was interpreted to suggest that homogenization of the contaminant took place in a staging chamber before magma ascension and emplacement in the upper crust (Harris et al., 2005) and calls for a decoupling of the behavior of oxygen isotopes and others such as Sr and Nd.

Initial findings using multiple sulfur isotopes in the Platreef, an ore horizon in the Northern Limb of the RLS (Penniston-Dorland et al., 2008), indicated the presence of an Archean surface-derived sulfur component (MIF, $\Delta^{33}S \neq 0$) in the magma, suggesting that the RLS itself has a surface-derived sulfur signature that is unrelated to assimilation of the local Archean host rock. Penniston-Dorland et al. (2012) analyzed fifteen samples from other parts of the intrusion and observed the same apparently uniform S isotope signature of $\Delta^{33}S = 0.11 \pm 0.02$. In this paper, we report the multiple sulfur isotopic composition of bulk rock samples for the entire stratigraphy of the RLS in order to assess if there is variability in $\Delta^{33}S$ such as what is observed in radiogenic systems, or whether it is homogeneous as seen in the oxygen isotopes. When considering the model of emplacement as sill-like (Mungall et al., 2016), if there is one single contaminant in the magma, the sulfur isotope composition is expected to vary directly with radiogenic isotopes. This covariation is used to provide insight into the origin of the crustal contamination, evolution of the magmas, constrain the source(s) of sulfur, and the mechanisms operating during the magmatic evolution of the Rustenburg Layered Suite that might be responsible for the PGE-rich layer formation.

2.3. Geological Background

2.3.1. The Rustenburg Layered Suite (RLS)

The Bushveld Complex intruded the sedimentary rock sequence of the Transvaal Supergroup in Northeastern South Africa at 2.06 Ga (Buick et al., 2001) and includes four different igneous suites: the volcanic rocks of the Rooiberg Group, the mafic-ultramafic Rustenburg Layered Suite (RLS), the Lebowa Granite Suite and the Rashoop Granophyre (Figure 2.1). The RLS, which is the focus of this study, outcrops in three main areas, classified after their geographical disposition: Eastern, Western and Northern Limbs.

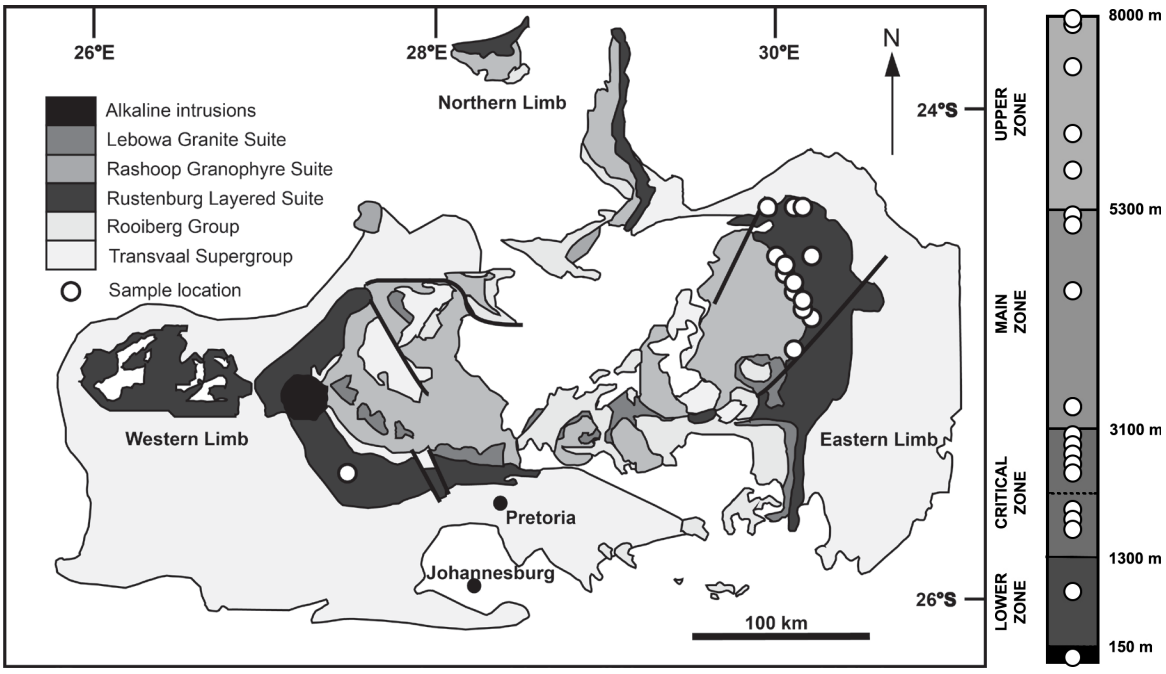

Figure 2.1. Map of the Bushveld Complex and stratigraphic column of the RLS with the approximate location of the samples used in this study (after Penniston-Dorland et al., 2012).

The Rustenburg Layered Suite (RLS) is a bowl-shaped layered mafic-ultramafic intrusion composed of progressively more fractionated cumulus rocks towards the top (Figure 2.1). The intrusion is subdivided vertically into several zones. Above the basal Marginal Zone, which marks the contact between the magma and the floor rocks of the intrusion, is the Lower Zone, which is dominated by pyroxenite and harzburgite (Cameron, 1978). The overlying Critical Zone is subdivided into the Lower Critical and Upper Critical Zones. The former mostly consists of pyroxenite interbedded with chromitite layers, whereas the Upper Critical Zone possesses layers of norite and anorthosite. The latter includes the well-known UG2 Chromitite layer and the Merensky Reef (in the Eastern and Western Lobes) and the Platreef (in the Northern Limb), which are PGE–ore layers (Cawthorn and Walraven, 1998). Above this is the Main Zone, which consists of gabbro and gabbronorite, and the Upper Zone, which is a layered sequence of magnetite-gabbro, gabbronorite, anorthosite, and diorite (VanTongeren and Mathez, 2010). The layers were originally thought to form from mineral deposition in a large single magma chamber, however new models have challenged that belief, as U-Pb ages suggests out-of-order emplacement (Mungall et al., 2016). The entire RLS sequence is about 7-8 km at its thickest (Cawthorn and Walraven, 1998).

2.3.2. Isotope composition of the RLS

The Rb-Sr and Sm-Nd isotope systems provide evidence for crustal contamination of the magma. The $(^{87}Sr/^{86}Sr)_i$ values for the RLS rocks are high relative to primitive mantle and are variable within the stratigraphy, ranging from 0.705 to 0.709 (Kruger, 2005). These correlate inversely with the negative $\varepsilon_{Nd(2.06Ga)}$ values of -5.3 to -7.9 (Maier et al., 2000). Variation of both $(^{87}Sr/^{86}Sr)_i$ and ε_{Nd} values appear also to be correlated with stratigraphy, which Maier et al.

(2000) interpret as related to the composition of different parental RLS magmas, serving as evidence for multiple magma pulses. Lead isotopes highlight that not only there is a disequilibrium between sulfide and plagioclase, but also a range of Pb isotope compositions require multiple sources for Pb, which indicates a contribution from the host rock (Mathez and Waight, 2003), suggesting that the Transvaal Supergroup is one potential source of crustal contamination in the magma.

Osmium isotope analysis of laurite (RuS_2) from ore horizons of the RLS yield $^{187}Os/^{186}Os$ values ranging from 1.28 to 1.60, which are more radiogenic than expected for a mantle-derived magma (McCandless et al., 1999). Radiogenic Os isotopic compositions of sulfide inclusions in diamonds from peridotite xenoliths in the Premier Kimberlite, an intrusion located in the same geographical area as the RLS that brings xenoliths from the mantle underneath that region suggest that the sub-continental lithospheric mantle might be the source of crustal contamination of the Bushveld Complex, and subsequently the Rustenburg Layered Suite (Richardson and Shirey, 2008).

The Hf isotope composition of the RLS is homogeneous and distinct from the depleted mantle reservoir at 2.06 Ga, as the measured $\varepsilon_{Hf(2.06Ga)}$ of the RLS varies from −9.0 to −6.8, values that overlap within the uncertainty of the measurements (Zirakparvar et al., 2014). These values suggest the occurrence of crustal contamination, but simple calculations of mixing of a primitive mantle-derived liquid with crustal material from the Limpopo Belt (chosen as a proxy for crustal composition because it is Archean crust, and also due to its close proximity to the RLS) cannot generate the Hf concentrations, $^{176}Hf/^{177}Hf$ ratios and major-element compositions observed in the RLS. Zirakparvar et al. (2014) suggest that the crustal Hf compositions are a

characteristic of the magma source, and hypothesize that this source might be the metasomatized sub-continental lithospheric mantle.

Analyses of oxygen isotopes in plagioclase, pyroxene and olivine from the RLS suggest a magmatic value of $\delta^{18}O$ up to 7.1‰, which is higher than expected for mantle-derived basaltic rocks (5.7‰; Muehlenbachs and Clayton, 1976), supporting the hypothesis of contamination from crustal sources (Harris et al., 2005). However, there is no systematic change in the oxygen isotope values throughout the stratigraphy of the RLS such as the ones observed in $(^{87}Sr/^{86}Sr)_i$, $\varepsilon_{Nd(2.06Ga)}$ and $^{187}Os/^{188}Os$ profiles.

Sulfur isotopes further support the hypothesis of magma contamination. One of the models of formation of the Platreef had proposed that the sulfur in the Platreef was incorporated in the magma due to local interaction between the country rock and the magma (Harris and Chaumba, 2001). Yet, Penniston-Dorland et al. (2008) found that although sulfur isotopes recorded evidence for interaction between the host rock and the mafic magma within 5 meters of the contact between units, a surface-derived sulfur signature ($\Delta^{33}S$) was present in samples physically distant from the contact. The data in the Penniston-Dorland *et al.* (2012) study of rocks from the Critical and Main Zones in the Eastern and Western Limbs show a uniform value of $\Delta^{33}S = 0.11 \pm 0.02$‰ ($2\sigma$) that is similar to that of the Platreef. This homogeneity led the authors to suggest the possibility that whatever processes added this surface-derived sulfur signal to the RLS took place prior to final emplacement of the magma in the crust.

2.4. Methodology

2.4.1. Sulfide characterization

The samples reported in this paper were collected in the Eastern Bushveld (except for B-4, Figure 2.1; Table 2.1). The dataset encompasses surface samples and drill core pieces from the entire RLS stratigraphy, from the Lower Zone to the Upper Zone, and also includes two granophyre samples from the roof of the intrusion that are described as differentiates from the Upper Zone magma. We chose samples that cover the entire depth of the intrusion, but focused on parts of the stratigraphy that showed the most significant variation in the radiogenic isotope profile.

Characterization of the sulfide phases was conducted using reflected light petrography of polished thin sections. Energy-dispersive spectroscopy (EDS) analysis was conducted using a JEOL 8900R electron probe microanalyzer (EPMA) at University of Maryland to confirm mineral identities.

2.4.2. Sulfur extraction

The multiple sulfur isotope composition was analyzed in bulk rock samples from different zones within the RLS stratigraphy. Approximately 10 grams of material of each sample was manually crushed using a steel mortar and pestle and then crushed further with a ceramic mortar and pestle, in order to guarantee that the rock was pulverized and sieved to a grain size smaller than 250 μm.

Sulfur was extracted from sulfide minerals by reaction with a heated Cr(II) solution in 5N HCl, in a boiling flask, purged with nitrogen. This combination was used in order to extract

sulfur present in sulfide and disulfide forms. The reaction of the sulfides with these solutions releases hydrogen sulfide gas (H_2S) that is carried by the nitrogen through a condenser and a bubbler filled with MilliQ water and then trapped in a 0.3M $AgNO_3$ solution, where it reacts and precipitates silver sulfide (Ag_2S). The experiment is set up for a reaction time of at least three hours (Canfield et al., 1986).

After these procedures were carried out, some samples did not yield enough silver sulfide to guarantee a reliable analysis due to their low sulfur concentration. A new experimental procedure was developed in order to enable the measurement of these samples. For those analyses, larger amounts of rock powder (up to ca. 80 grams) were used and a magnet stir bar was placed into the boiling flask to mix the sample and the solution using a magnetic stirrer.

After the sulfur extraction was completed, the silver sulfide samples were then stored in a dark box for at least 7 days, after which they were washed in a multistage process with MilliQ water and 1M NH_4OH. They were subsequently dried at 50°C.

Weighed aliquots of the dried silver sulfide (approximately 3 mg) were sealed in aluminum foil capsules and placed into heated Ni vessels. Fluorine gas was added and left overnight to react with the silver sulfide to produce SF_6. The resulting SF_6 is separated from possible byproducts (e.g. HF) through a thorough purification process that involves cryogenic separation, passivation, and gas-chromatography. After purification, the SF_6 samples were frozen into glass fingers in a manifold and were subsequently analyzed using a ThermoFinnigan MAT253 gas source mass spectrometer in the Stable Isotope Laboratory of the University of Maryland.

The sulfur isotopic composition of materials is reported using the delta (δ) notation, which is referenced to the ^{32}S isotope, using the V-CDT (Vienna-Canyon Diablo Troilite) standard (equations 1.1 and 1.2). The correction value was obtained after the Wing and Farquhar (2015) calibration.

$$\delta^{33}S = \left[\frac{\left(\frac{^{33}S}{^{32}S}\right)_{\text{sample}}}{\left(\frac{^{33}S}{^{32}S}\right)_{\text{V-CDT}}} - 1\right] \quad (1.1)$$

$$\delta^{34}S = \left[\frac{\left(\frac{^{34}S}{^{32}S}\right)_{\text{sample}}}{\left(\frac{^{34}S}{^{32}S}\right)_{\text{V-CDT}}} - 1\right] \quad (1.2)$$

Variations in mass independent compositions are quantifiable in terms of a capital delta (Δ) notation, as seen in Equation 1.3:

$$\Delta^{33}S = \delta^{33}S - [(1 + \delta^{34}S)^{0.515} - 1] \quad (1.3)$$

The uncertainty in the measurements for samples with high sulfur concentration is estimated from the long-term laboratory reproducibility of fluorinations of IAEA-S1, which yields 2σ variations of $\delta^{33}S$=0.15‰; $\delta^{34}S$=0.30‰; and $\Delta^{33}S$=0.016‰. We estimate that the chemical extraction of sulfur will not affect the values of $\Delta^{33}S$, but could double the uncertainty of $\delta^{33}S$ and $\delta^{34}S$. For samples with low concentration of sulfur, the reproducibility was based on

11 repeat analyses of sample ECG (Ellicott City Granodiorite): δ^{33}=0.43‰; δ^{34}S=0.84‰; and Δ^{33}S=0.023‰ (2σ).

2.5. Results

Sulfur is present in its reduced form (sulfide) in all samples; the most abundant sulfide minerals are pentlandite [$(Fe,Ni)_9S_8$], chalcopyrite ($CuFeS_2$), pyrite (FeS_2), and pyrrhotite ($Fe_{1-X}S$). Sample DT28 909.1, of the UG2 chromitite, also had PGE sulfides such as cooperite (PtS) and laurite (RuS_2), generally associated spatially with pentlandite, either as an inclusion or just in contact with each other. The δ^{34}S values of all the samples analyzed in this study range from -1.19‰ to 3.27‰, whereas those for Δ^{33}S range from 0.057‰ to 0.157‰, with an average of 0.110±0.030‰ (1σ) (Table 2. 1). The sulfur isotope data obtained for the samples, including the associated granophyres (average: 0.153‰), are generally comparable with measurements of the sulfur isotopic composition of samples previously published in the literature for the Western and Eastern Limbs, and parts of the Northern Limb (Penniston-Dorland et al., 2008, 2012; Figure 2.2). The calculated average after adding the data from Penniston-Dorland et al. (2012) is 0.112‰±0.024‰ (1σ).

All the samples have a sulfur signature that differs from mid-ocean ridge basalts (MORB), used in this study as a proxy to represent the sulfur composition of the uncontaminated mantle (MORB is by far the best-documented mantle reservoir for sulfur isotopes, especially Δ^{33}S measurements). Despite being sourced from the depleted mantle, MORB has a similar range of sulfur composition as uncontaminated ocean island basalts (OIB), which result from plume ascension into the crust (Sakai et al., 1984; Peters et al., 2010; Labidi et al, 2012);

however, OIB can incorporate recycled components. Measurements of MORB composition (Sakai et al., 1984; Peters et al., 2010) yielded values that range from -2‰ to +2‰, ($\delta^{34}S$); however, Labidi et al. (2012) demonstrated that a different chemistry extraction technique produced a narrower range, mostly negative (from -1.8‰ to 0.02‰), challenging the previous knowledge. The refined $\Delta^{33}S$ value is 0±0.008‰ (Peters et al., 2010; Labidi et al., 2012), lower than any value found in the RLS. We chose to use the larger range of $\delta^{34}S$ values to represent the MORB composition (Figure 2.2) with the aim to show that despite some compositional overlap, the RLS sulfur differs from any measurement of MORB samples. A significant number of $\delta^{34}S$ data from the RLS cluster between +1‰ and +2‰, more positive than the MORB values of Labidi et al. (2012), with a few samples displaying higher values up to 3.27‰. Only one sample presents a $\delta^{34}S$ composition within the Labidi et al. (2012) MORB range, a negative value of -1.19‰ (B06-060). All the samples fall outside the $\Delta^{33}S$ MORB composition.

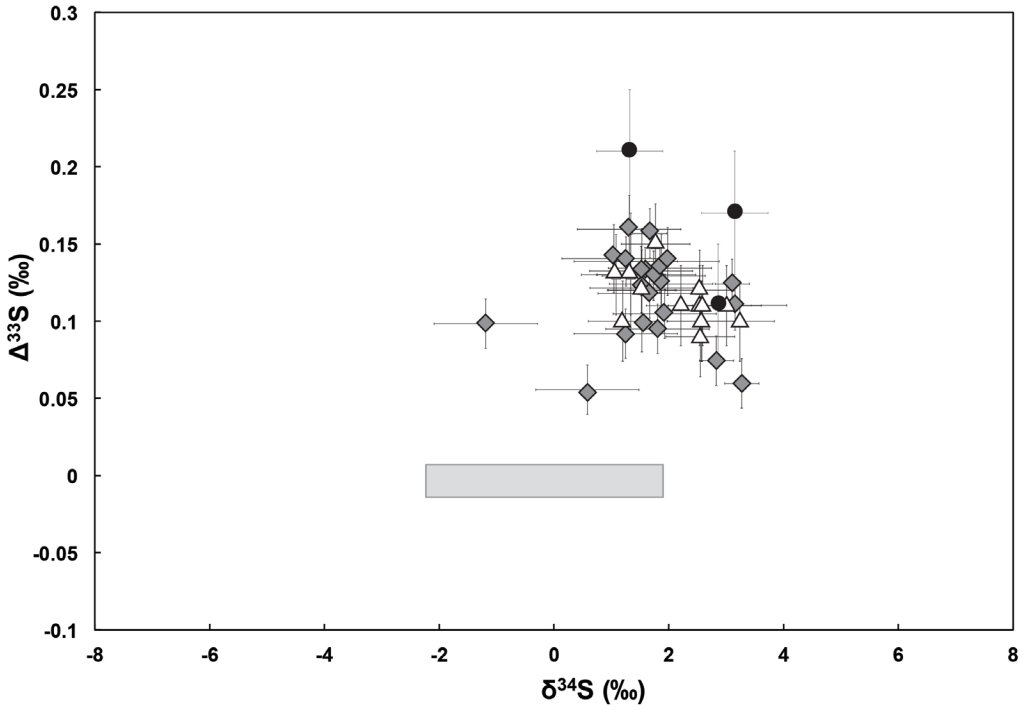

Figure 2.2. Multiple sulfur isotope composition of the Rustenburg Layered Suite, Bushveld Complex, compared to uncontaminated mantle values given by MORB composition (gray rectangle; data from Sakai et al., 1984; Chaussidon et al., 1991; Peters et al., 2010). Grey diamonds represent data from this study, while white triangles are Critical and Main Zones samples studied in Penniston-Dorland et al. (2012). Select Northern Limb samples (black circles) were also plotted for comparison (Penniston-Dorland et al., 2008). Error bars are 2σ uncertainty.

Table 2.1. Sulfur isotope composition of Bushveld samples.

Sample	$\delta^{33}S$	$\delta^{34}S$	$\Delta^{33}S$	Rock Type	BC Zone	Location
BC16-05D	1.74	3.27	0.060	Norite	Marginal Zone	Eastern Limb
LZ10-02	1.27	2.34	0.067	Harzburgite	Lower Zone	Eastern Limb
TW477 660.3	0.89	1.57	0.078	Orthopyroxenite	Lower Critical Zone	Eastern Limb
TW477 440.57	0.36	0.58	0.057	Orthopyroxenite	Lower Critical Zone	Eastern Limb
TW477 202.15	1.09	1.93	0.101	Orthoyroxenite	Lower Critical Zone	Eastern Limb
DT28 910.3	0.90	1.58	0.087	Orthopyroxenite	Upper Critical Zone	Eastern Limb
DT28 909.1	1.72	3.10	0.124	Chromitite	Upper Critical Zone	Eastern Limb
DT28 904.7	0.85	1.42	0.113	Orthopyroxenite	Upper Critical Zone	Eastern Limb
DT28 847.2	0.94	1.58	0.122	Orthopyroxenite	Upper Critical Zone	Eastern Limb
B-4	0.97	1.68	0.103	Anorthosite	Upper Critical Zone	Western Limb
MP24D2	1.02	1.68	0.157	Orthopyroxenite	Upper Critical Zone	Eastern Limb
B90-01	1.66	2.97	0.129	Norite	Main Zone	Eastern Limb
B07-018	1.09	1.86	0.131	Gabbro	Main Zone	Eastern Limb
B06-060	0.68	1.04	0.144	Orthopyroxenite	Main Zone	Eastern Limb
B06-061	-0.51	-1.19	0.098	Norite	Main Zone	Eastern Limb
B06-011	0.91	1.52	0.132	Magnetitite	Upper Zone	Eastern Limb
B06-024	0.92	1.54	0.123	Troctolite	Upper Zone	Eastern Limb
B06-026	0.78	1.25	0.131	Gabbro	Upper Zone	Eastern Limb
B07-039	0.94	1.57	0.131	Diorite	Upper Zone	Eastern Limb
B10-054	1.16	1.98	0.145	Granophyre	Granophyre Suite	Eastern Limb
B10-042	0.83	1.31	0.161	Granophyre	Granophyre Suite	Eastern Limb

Figure 2.3 presents the $\Delta^{33}S$ data arranged in order of estimated stratigraphic height. The sample BC16-05D, which was collected at the contact of a norite with a calcsilicate rock, is plotted with an arbitrary depth equal to zero. The values of $\Delta^{33}S$ for samples lower in the stratigraphy (Marginal and Lower Zone) are distinctly different from the granophyre samples at the top of the intrusion: they have systematically lower values than the Upper Zone and granophyres. Variations in $\Delta^{33}S$, Nd, and Sr isotope profiles, can be found in the same stratigraphic levels for the three isotope systems (Figure 2.4; Maier et al., 2000; Kruger, 2005, this study). The correlation is not systematic; in some places, increases in $^{87}Sr/^{86}Sr_i$ are associated with increases in $\Delta^{33}S$, for example at the lowest part of the Main Zone, but in other places they are inversely correlated, such as in the Upper Zone. The Upper Zone is characterized by a $\Delta^{33}S$ composition of 0.132‰ and $^{87}Sr/^{86}Sr_i$ of 0.7073, the Main Zone is characterized by average $\Delta^{33}S$ equal to 0.120‰ and $^{87}Sr/^{86}Sr_i$ within the 0.708-0.709 range; the Critical Zone has a variable isotopic profile for both sulfur and strontium isotopes, and the Lower Zone has $\Delta^{33}S$ of 0.067‰ and $^{87}Sr/^{86}Sr_i$ between 0.705 and 0.707. When available, the ε_{Nd} data negatively correlate with Sr (Maier et al., 2000).

2.6. Discussion

The sulfur isotopic composition of the Rustenburg Layered Suite appears to be homogeneous laterally over large geographic distances, although further testing of this hypothesis is needed; $\Delta^{33}S$ values of samples from the Main Zone of both Eastern and Western Lobes overlap within uncertainty of measurement (4 samples from the Eastern Lobe have $\Delta^{33}S$=0.12-0.13; 2 samples from the Western Lobe have $\Delta^{33}S$=0.13-0.14; Penniston-Dorland et

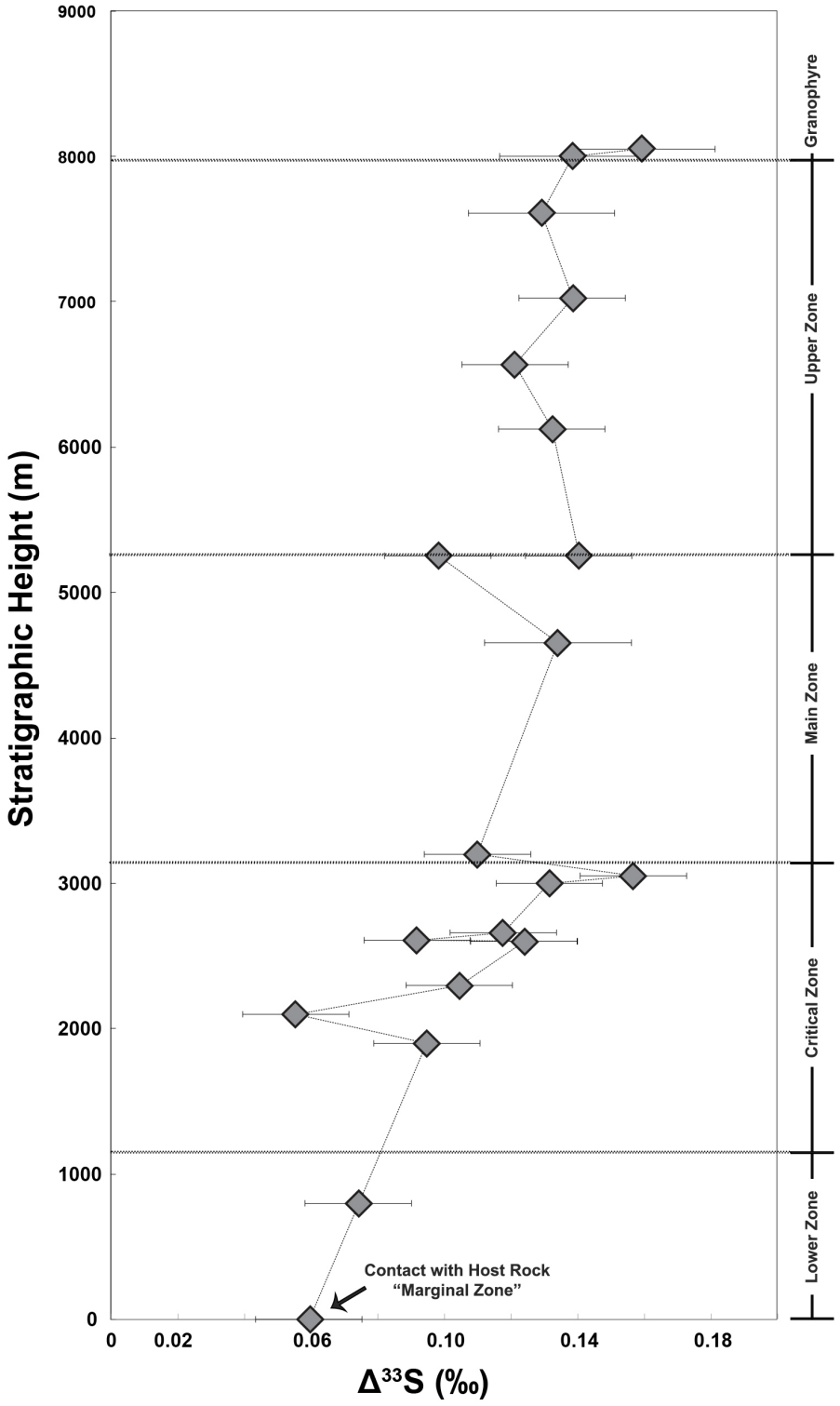

Figure 2.3. Variation of the $\Delta^{33}S$ composition according to stratigraphic position. Error bars are 2σ uncertainty.

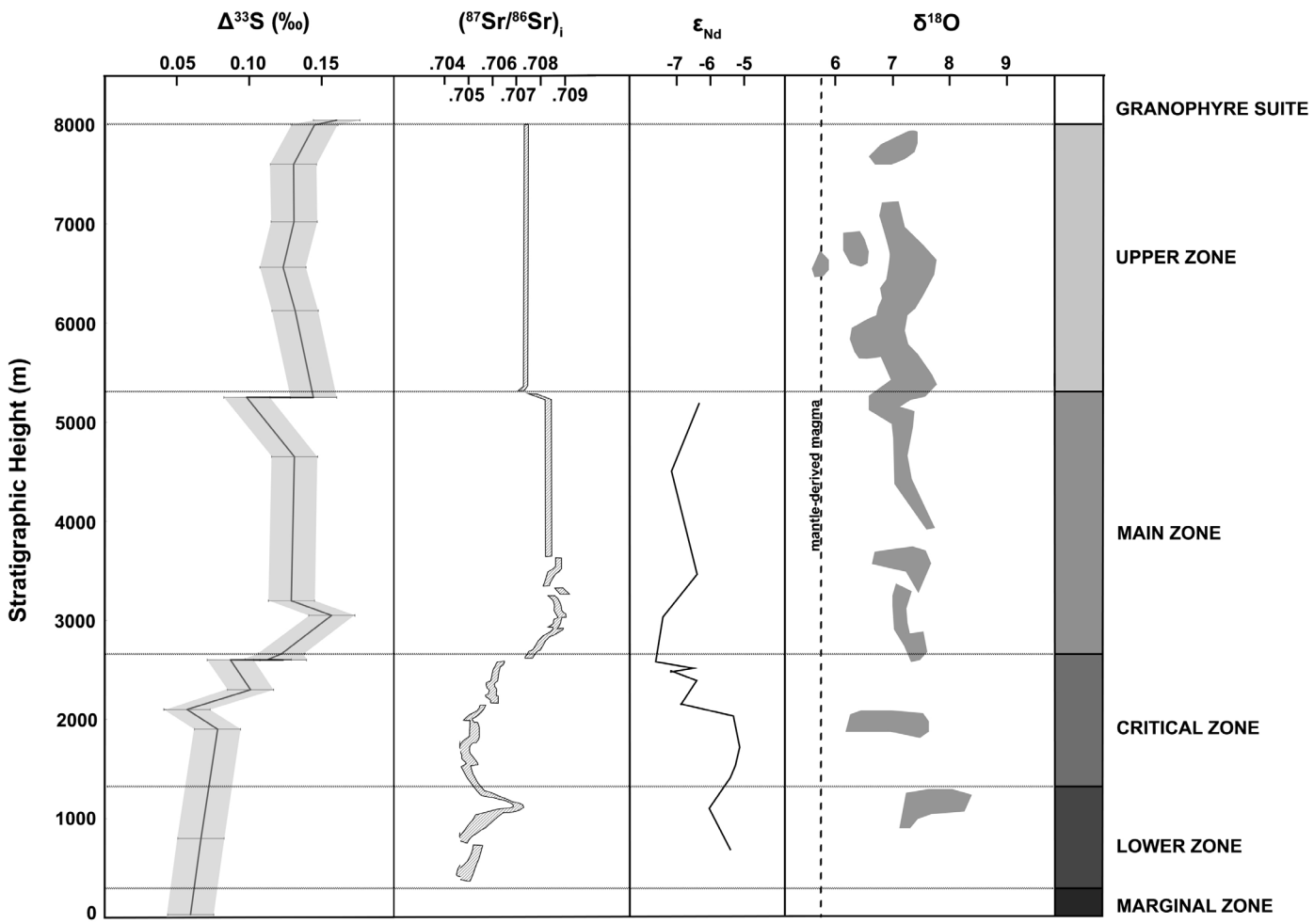

Figure 2.4. Diagram comparing the sulfur Δ33S composition of the Rustenburg Layered Suite with previously existing data for other isotope systems. A relationship between the isotope composition of sulfur, strontium, and neodymium can be seem as shifts in composition are related to stratigraphy. Oxygen isotope values do not present a correlation to the other systems. Values of (87Sr/86Sr)i were plotted after Kruger (2004), εNd data after Maier et al. (2000), and δ18O data after Harris et al. (2005).

al., 2012, this study). Additionally, the similarity of the $\Delta^{33}S$ signature of the Upper Zone (average: 0.132‰) and the granophyre at the roof of the intrusion (average: 0.153‰), which overlap within the uncertainty of measurement, suggests that the granophyre may be genetically related to the cumulus mafic rocks, instead of resulting from melting of crustal rocks at depth, reinforcing the findings of VanTongeren et al. (2016).

Subtle variations in $\Delta^{33}S$ values with increasing stratigraphic height within the intrusion occur and can be linked to variations in other isotope systems such as $^{87}Sr/^{86}Sr_i$ and ε_{Nd}. The lack of a systematic correlation suggests the addition of different materials instead of a single contaminant for the intrusion, as the relationship between sulfur and the other elements cannot be explained simply by different amount of contamination of the magma with the same material. While increases in $\Delta^{33}S$ are associated with increases in $^{87}Sr/^{86}Sr_i$ values in the Critical and Main Zones, increases in $\Delta^{33}S$ are associated with decreases in $^{87}Sr/^{86}Sr_i$ in the Upper Zone. These differences in contaminants likely relate to different pulses of magma, with different pulses assimilating different materials. On a smaller scale, the variability in strontium and sulfur isotopes observed in the Critical Zone ranges from 0.057‰ to 0.157‰ for $\Delta^{33}S$, and $^{87}Sr/^{86}Sr_i$ between 0.705 and 0.707. The highest $\Delta^{33}S$ values are observed in the Merensky Reef and UG2 ore horizons. This variation implies that the Critical Zone was formed by pulses of the same magma that assimilated the same material but in different proportions, congruent with sill-like out of order emplacement of the layers. The magma that originated the Upper Zone is likely to have gone through homogenization before emplacement, given its very uniform average isotope composition of 0.132‰±0.008‰, 1 s.d..

The decrease observed in both $\delta^{34}S$ and $\Delta^{33}S$ at the top of the Main Zone (Figures 2.3 and 2.4) occurs just below the Pyroxenite Marker, a layer that marks the transition between the Main

and Upper Zones. The occurrence of this layer is also thought to coincide with a new pulse of magma (e.g., VanTongeren and Mathez, 2013), which further suggests that the occurrence of a distinguishable shift of the isotope profiles directly reflects different magma pulses with different isotope characteristics. The inverse behavior of $\Delta^{33}S$ and $^{87}Sr/^{86}Sr_i$ at the boundary between the Main and Upper Zones also highlights the possibility that these zones have been contaminated by different materials with different isotopic characteristics.

2.6.1. Source of surface-derived sulfur in the RLS

Hypotheses on what is the source of the anomalous sulfur of the Rustenburg Layered Suite and how it acquired its isotopic composition include (a) assimilation of the host rock during emplacement; (b) contamination by crustal rocks during a staging chamber phase, which would have been then homogenized; (c) contamination during passage of the melt through the sub-continental lithospheric mantle, which would already have a non-zero $\Delta^{33}S$ composition, or (d) the original composition of an asthenospheric source that already had an anomalous sulfur signature. These hypotheses are not mutually exclusive.

The lack of a systematic variation between $\Delta^{33}S$, $(^{87}Sr/^{86}Sr)_i$, and ε_{Nd}, shows that the Rustenburg Layered Suite has incorporated sulfur from at least more than one source during its history, so there may not be a unique solution to this question. Petrographic analysis has provided little evidence for extensive post-magmatic processes, which suggests that the RLS sulfur isotope $\Delta^{33}S$ signature is not a result of homogenization or late addition of sulfur by hydrothermal fluids. Below, each of these sources of sulfur are further discussed.

2.6.1.1. Assimilation of S upon emplacement: Transvaal Supergroup as a contaminant

One explanation for the crystallization of PGE sulfides in the RLS invokes large-scale contamination and sulfur addition into an unsaturated mafic magma (e.g. Mavrogenes and O'Neill, 1999). One possible source for this sulfur could be assimilated Transvaal Supergroup sedimentary rocks. However, many studies have shown that the different formations of the Transvaal Supergroup, the host rock for the RLS, have highly variable $\delta^{34}S$ and $\Delta^{33}S$ (Kaufman et al., 2007; Guo et al., 2009). The average values of $\delta^{34}S$ and $\Delta^{33}S$ of the Rustenburg Layered Suite are, respectively, +1.86‰±0.88‰ and 0.112‰±0.024‰ and are relatively homogeneous when compared to the variability of Transvaal sedimentary rocks values. The sedimentary rocks in the Transvaal Basin vary in $\delta^{34}S$ between -14.47‰ and +20.67‰, and $\Delta^{33}S$ between -0.36‰ to +5.04‰ (Figure 2.5a). There is a high degree of variability in local sedimentary rocks in lithology, layer thickness, sulfur concentration and sulfur isotopic composition.

The expanded dataset detailed in this study includes samples from different stratigraphic layers that likely represent multiple pulses of magma. For the different pulses of magma to have such a narrow $\Delta^{33}S$ composition when compared to the ranges observed in the surrounding sedimentary rocks it would require both efficient mixing and a fortuitous combination of amount of assimilation and host rock $\Delta^{33}S$ composition to result in a similar $\Delta^{33}S$. Although efficient mixing needs to have happened if the compositions are indeed homogeneous laterally (Penniston-Dorland et al, 2012), the isotope variability is still recorded in the intrusion vertically (given the variations in $\Delta^{33}S$).

Calculations performed by Penniston-Dorland *et al.* (2012) show that if the contaminant of the RLS magma were a Transvaal shale containing 1 wt% sulfur with an average $\Delta^{33}S$

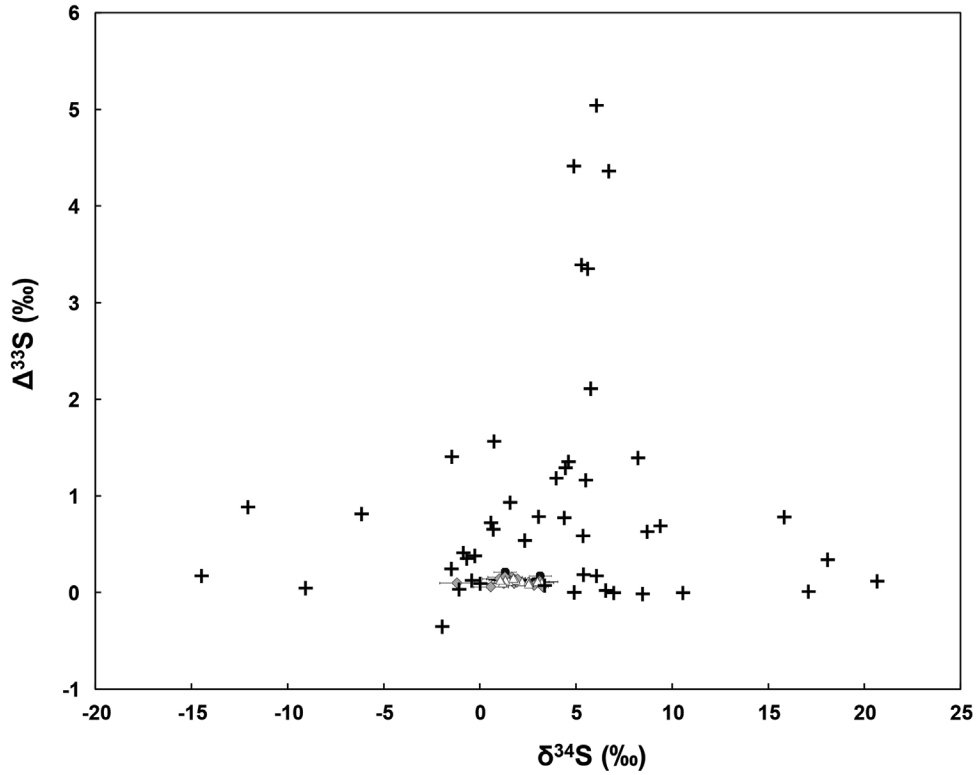

Figure 2.5a. Multiple sulfur isotope composition of the Transvaal Supergroup rocks located at the Transvaal Basin (+) compared to the Rustenburg Layered Suite (data from Penniston-Dorland et al. 2008, Guo et al. 2009) and Vredefort Dome sulfur isotope composition, as seen in Figure 2.5b. The sedimentary rocks show a highly variable composition, both in $\delta^{34}S$ and $\Delta^{33}S$, compared to the igneous rocks of the RLS and the metamorphic rocks of the Vredefort Dome.

composition of 2.8‰, the minimum amount of 0.3 wt% shale would have been necessary to create the RLS average $\Delta^{33}S$ composition. Higher amounts of assimilation, such as needed to explain oxygen isotopes (~40%) or trace elements (˜70%), are in direct contrast to the measured sulfur composition and to the estimate of sulfur concentration in the RLS (800 ppm), requiring assimilation of materials with a much lower sulfur concentration.

The lack of a higher $\Delta^{33}S$ signature in the sample at the base of the stratigraphic column, which is in direct contact with sedimentary rocks (sample BC15-05D), contrasts to what is observed in the Platreef of the Northern Limb, where high $\Delta^{33}S$ values are observed at the contact with the floor rocks (Penniston-Dorland et al., 2008; Sharman et al., 2013). This suggests that assimilation of wall rock upon emplacement may not dictate the sulfur isotopic composition of the intrusion.

2.6.1.2. Contamination by deep crustal rocks in a staging chamber

One hypothesis for the formation of the Rustenburg Layered Suite postulates the existence of a staging chamber in the lower crust, in which the magma resided before the final emplacement into the upper crust, and where it would have assimilated the surrounding material (e.g. McCandless et al., 1999). If the rocks from the lower crust in the Kaapvaal Craton have an anomalous sulfur isotopic composition, it could explain the sulfur isotope composition of the RLS.

Previously published data present conflicting requirements for contamination by deep crustal rocks, including varying amounts of assimilation required and varying types of material assimilated. While the radiogenic osmium isotopic composition may be explained by assimilation of 5% of mafic granulite into tholeiitic magma during a staging chamber phase in the lower crust (McCandless et al., 1999), such assimilant may not provide the necessary Sr to produce the observed radiogenic Sr isotopic compositions (Schoenberg et al., 1999). Harris et al. (2005) considered two possible regions as proxies for the lower to middle crust when calculating the amount required to produce the elevated oxygen isotopic composition observed in the RLS: Archean basement rocks of the Vredefort impact structure and those of the southern marginal

zone of the Limpopo Belt. These calculations indicate that the oxygen isotope composition requires a much greater amount of assimilated lower crust, of up to 36-41%. A higher amount of assimilant is also required by the trace element composition of the RLS, requiring up to 70% contamination (Maier et al., 2000). In addition, the Hf isotopic compositions of the RLS (Zirakparvar et al., 2014) argue against the existence of a staging chamber, as calculations show that no amount of mixing between a komatiitic magma, representative of the primitive Bushveld-magma, and gneiss or sediments from the lower crust, using rocks from the Limpopo Belt as a proxy, could produce the observed Hf compositions (Zirakparvar et al., 2014).

We have analyzed samples from the Vredefort Dome, a 2.02 Ga impact crater located approximately 300 km southwest of the RLS that exhumed rocks of the middle to lower crust (Lana et al., 2003), using the same protocols described in the methodology section. Samples of the Limpopo Belt were not available for study. The analyzed samples include metasedimentary rocks, metagranitoids, and metamafites. The $\delta^{34}S$ of these rocks varies from 0.74‰ to 5.22‰ and the $\Delta^{33}S$ varies between -0.010‰ and 0.145‰ (Figure 2.5b; Table 2.2). These compositions are in a similar range as the RLS. However, the maximum $\Delta^{33}S$ value observed is still slightly lower than that observed in the RLS, and we did not find any composition that when mixed with an uncontaminated mantle could have produced the RLS composition. The concentration of sulfur in some of these rocks is very low, at times less than 100 ppm (as evidenced by the wet chemistry stage). Although unlikely, it is possible that such low concentrations could have been caused by devolatilization upon impact, and therefore would not correspond to the original concentration, and a shift in $\delta^{34}S$ could occur. However, devolatilization is not expected to alter the $\Delta^{33}S$ values. A similar range of $\delta^{34}S$ compositions have been observed in lower crustal granulite-facies rocks from Australia (Hammerli et al., 2016), which suggests that if

devolatilization occurred, it did not significantly impact the $\delta^{34}S$ values of the Vredefort Dome rocks.

Table 2.2. Sulfur isotope composition of rocks from the Vredefort Dome.

Sample	$\delta^{33}S$	$\delta^{34}S$	$\Delta^{33}S$	Rock type
VF14-004B	1.23	2.41	-0.010	Pseudotachylite
VF14-008A	2.44	4.45	0.145	Metasediment
VF14-008B	2.45	4.49	0.139	Metasediment
VF14-008C	2.78	5.22	0.095	Metasediment
VF14-016	0.71	1.22	0.079	Granitoid
VF14-018	0.38	0.74	0.003	Wehrlite
VF14-019C	1.11	2.00	0.080	Granitoid

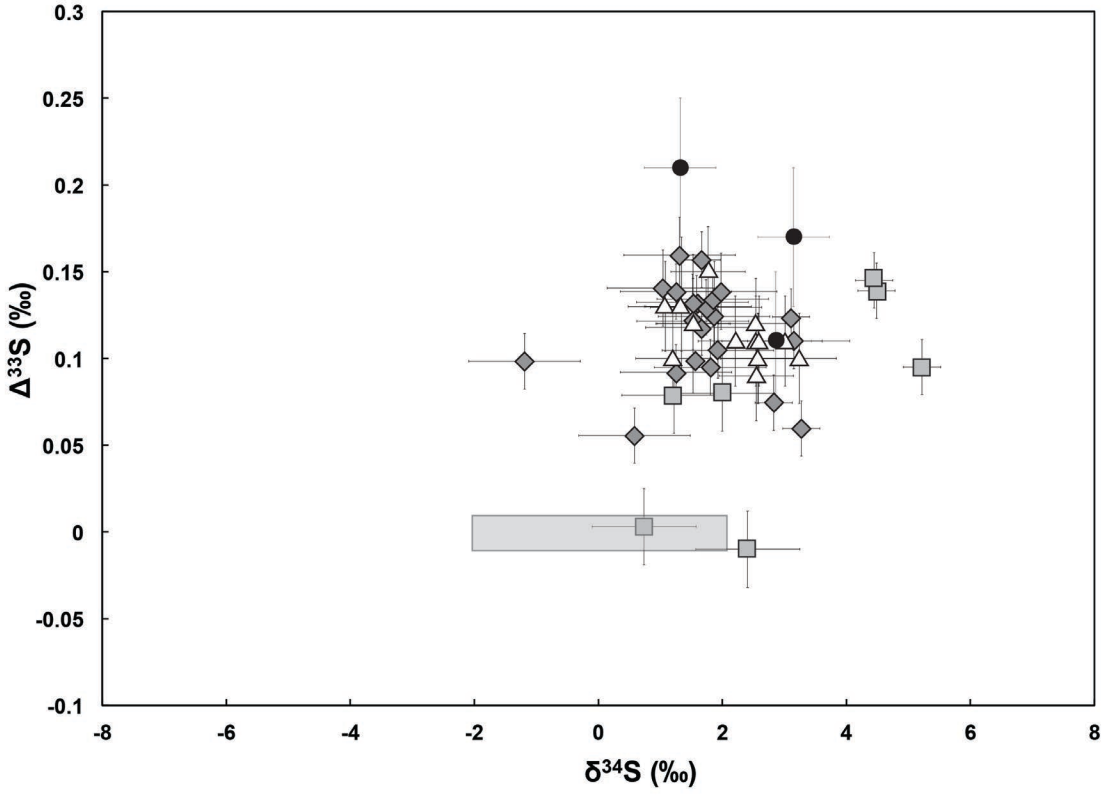

Figure 2.5b. Composition of the Vredefort Dome (squares, other symbols as in Figure 2.2) rocks compared to the Rustenburg Layered Suite (this study; Penniston-Dorland et al, 2008; 2012), and the uncontaminated mantle composition (MORB data, Sakai et al., 1984, Chaussidon et al., 1991; Peters et

al., 2010). All the $\Delta^{33}S$ values of the Vredefort Dome rocks are lower than the maximum values of the RLS, which suggests that these rocks are not end members of mixing with magma with uncontaminated mantle composition. Error bars are 2σ uncertainty.

Given the calculations performed by Penniston-Dorland et al. (2012), it is not possible to reconcile the concentration of sulfur in these rocks and their isotopic composition in a realistic way such that they could have, alone, generated the composition of the RLS. However, the actual composition of the middle and lower crust underneath the intrusion is not known, and might differ from the data presented in this study.

2.6.1.3. The sub-continental lithospheric mantle as a contaminant

The Kaapvaal Craton has seen many episodes of amalgamation, including the subduction of the Witwatersrand Block underneath the Kimberley Block at ~2.9 Ga and the formation of the Limpopo Belt from 3.0 to 2.0 Ga, dominated by a major tectonothermal event at 2.6 Ga (e.g. Kamber et al, 1995; Schmitz et al., 2004), resulting from the collision between the Zimbabwe and Kaapvaal Cratons. The sub-continental lithospheric mantle (SCLM) underneath the Kaapvaal Craton has experienced multiple episodes of melting and metasomatism during its geological history (e.g. Carlson et al, 2005; Shu et al., 2013; and references therein). Growth of the SCLM in this area is thought to have started early in the Archean, with reported ages of 3.4 Ga in Eastern Kaapvaal (Eglington and Armstrong, 2004). Rhenium depletion model ages in mantle xenoliths range from 3.7 to 2.0 Ga, some of which overlap with the timing of the Bushveld magmatic event (Carlson et al., 1999; Richardson and Shirey, 2008) reflecting extensive melt depletion related to crustal growth. The SCLM was also modified during the Bushveld magmatic event at approximately 2.06 Ga (Richardson and Shirey, 2008), which further supports the hypothesis that the SCLM beneath the Kaapvaal Craton interacted with the

magma that generated the RLS. Later, some portions of the craton have experienced an episode of metasomatism at 1.3 Ga (Shu et al., 2013).

Mantle recycling of ancient surface (likely oceanic) reservoirs with sulfur MIF compositions is suggested by anomalous sulfur isotopic compositions (non-zero $\Delta^{33}S$) preserved by sulfide inclusions in diamonds from the Orapa and Jwaneng kimberlites, both located in edges of the Kaapvaal Craton in Botswana (Farquhar et al., 2002; Thomassot et al., 2009). The sulfide inclusions in diamonds from the Orapa kimberlite yield values of $\Delta^{33}S$ from -0.11‰ to +0.61‰ (Farquhar et al., 2002), while in the Jwaneng Kimberlite, the $\Delta^{33}S$ values range from -0.5‰ to +0.9‰ (Thomassot et al., 2009). These values suggest that S concentrations in SCLM of 200 to 20,000 ppm would be required to reach the mass fractions of SCLM contaminant predicted by Os isotopes (Penniston-Dorland et al., 2012; Richardson and Shirey, 2008).

Evidence for recycling of sulfur into the mantle can be found in both modern and fossil subduction zones. Isotope data from modern arc volcanic rocks suggest that sulfur is recycled by subduction today and transferred from subducting slabs to the mantle wedge beneath volcanic arcs. Basaltic arc volcanic rocks from Indonesia preserve positive $\delta^{34}S$ values of +2.0‰ to +7.8‰, and despite possible fractionation caused by degassing or sulfur loss, the data still can be interpreted as enrichment of the mantle source by addition of slab-derived sediments (De Hoog et al., 2001). Eclogite-hosted sulfides also preserve elevated $\delta^{34}S$, suggesting the role of metamorphic fluids in transferring sulfur within the slab during subduction (Evans et al., 2014). In the Mariana Island Arc, Alt et al. (1993) described $\delta^{34}S$ values of up to 21‰ in volcanic rocks, a value similar to the present-day seawater sulfate $\delta^{34}S$ value of ~21‰, suggesting that the sulfur composition derived from seawater sulfate-related sources. Evidence from both $\Delta^{33}S$ and $\delta^{34}S$ of

fossil magmatic arc rocks from the Glenburgh Terrane in Western Australia also indicates cycling of Archean sulfate and sulfide in a subduction setting (Selvaraja et al., 2017).

Melting and melt depletion cannot explain the observed non-zero $\Delta^{33}S$ signature as these are mass-dependent processes, but recycling of sulfur during subduction and metasomatism could transfer material bearing a non-zero $\Delta^{33}S$ signature to the SCLM (Selvaraja et al., 2017). Evidence for incorporation of crustal material in the SCLM is also observed in other systems, such as Re-Os (Richardson and Shirey, 2008), although the sulfur composition constrains that this material needs to be of Archean age. The occurrence of MIF in sulfides from Orapa and Jwaneng Kimberlites suggests that sulfur MIF signatures are present in at least some parts of the SCLM underlying the Kaapvaal Craton. Despite the lack of a MIF signature, transfer of a surface signature due to mantle metasomatism was inferred to produce the variability in $\delta^{34}S$ values in sulfides from xenoliths in the Bultfontein Kimberlite, located in the southern portion of the craton (Giuliani et al., 2016), further adding evidence to a heterogeneity of the SCLM underneath the Kaapvaal Craton. Work on peridotite and eclogite xenoliths from the Premier Kimberlite, geographically associated with the RLS, is currently being done in order to assess whether this hypothesis is viable.

2.6.1.4. Asthenospheric mantle source with a $\Delta^{33}S \neq 0$

Studies of rock and mineral chemistry indicate a mantle origin for the primary magma of the RLS, likely originating from a mantle plume given the calculated initial composition and volume of magma produced in this event (Hatton, 1995; Wilson, 2012). The most primitive magma is found in the lower part of the intrusion (Wilson, 2012), although its Sr isotope composition is unlike that expected of uncontaminated mantle.

Studies on the isotopic composition of asthenospheric mantle are constrained by the rarity of material available, and what is known results mostly from indirect observation. It is possible to distinguish multiple geochemical reservoirs in the mantle based on different isotope characteristics (White, 2015). These reservoirs (HIMU, EMI, EMII, DMM, among others) are sampled by the ascension of mantle-originated magma to the crust; for some of these reservoirs, the isotopic signatures reflect addition of surface-derived material to the mantle. However, this classification is done mostly for modern basalts.

Evidence for recycled sulfur in the asthenospheric mantle comes from anomalous $\Delta^{33}S$ sulfur compositions of primary magmatic sulfide inclusions in olivine phenocrysts from Mangaia, Cook Islands, which samples the HIMU reservoir (e.g., Cabral et al., 2013). Although it is not possible to infer at which depth the contamination took place, Mangaia samples Archean material that was subducted into the mantle. Delavault et al. (2016) also observed negative $\Delta^{33}S$ values (down to -0.8‰) in sulfides from Pitcairn, of the Pitcairn-Gambier chain in the Pacific. The same authors also modeled the source age to be 2.5 to 2.6 Ga. Further evidence for recycling comes from other isotope systems, such as elevated $\delta^{18}O$ values of OIB (Eiler et al., 1997), and light $\delta^{13}C$ values of diamonds from a Cretaceous kimberlite in Brazil (Walter et al., 2011). Recycling of surface material in the mantle below the Kaapvaal Craton is seen in the Jagersfontein kimberlite, where diamonds present light $\delta^{13}C$ signatures (ranging from -17.4‰ to -23‰) and their majorite inclusions have high $\delta^{18}O$ values (+8.5‰ to +10‰) (Ickert et al., 2015).

Findings of recycled sulfur in both Mangaia and Pitcairn could open the possibility that the mantle plume that originated the Bushveld Complex and the Rustenburg Layered Suite originally contained this signature; however, the RLS composition would not fall within a field

of any known end-member defined by Sr and Nd isotopes. Therefore, although the present knowledge points towards the recycling of surface material into the asthenospheric mantle, we do not expect that the sulfur isotope composition of the RLS comes from recycled component in the primitive magma.

2.7. Conclusions

The Rustenburg Layered Suite, a mafic-ultramafic intrusion that is part of the Bushveld Complex, has a sulfur isotope composition that reflects the presence of a surface-derived material in the magma. This study reveals subtle variations in $\Delta^{33}S$ in the igneous stratigraphy of this intrusion. The RLS was likely formed by the injection of multiple pulses of magma, and the correlation of variations in sulfur isotopes with variations in $^{87}Sr/^{86}Sr_i$ and ε_{Nd} further supports that hypothesis. However, the lack of systematic correlation between these isotopic systems and $\Delta^{33}S$ shows that these variations cannot be accounted for by assimilation of a single contaminant in different proportions and calls for multiple contaminants.

Sedimentary rocks of the Transvaal Supergroup or rocks from the lower crust are possible sources of surface sulfur in the RLS. It is unlikely that contamination occurred during emplacement, since the isotopic compositions appear laterally homogeneous over large scales (except in particular circumstances; e.g., Penniston-Dorland et al., 2008; Sharman et al., 2013). Homogenization of assimilated crustal material may have occurred in a staging chamber prior to intrusion, regardless of the small-scale variations in S, Sr, and Nd within the stratigraphy. Slight increases of $\Delta^{33}S$ values coincide with the UG2 Chromitite and Merensky Reef, suggesting that surface-derived sulfur may have played a part in the formation of the PGE-rich layers.

It is also possible that the interaction between a rising asthenospheric magma and a compositionally altered SCLM could have provided the magma with anomalous sulfur. Evidence for such interaction is seen in multiple studies and encompasses Bushveld-like Re depletion ages, depletion in Pt and Pd and Sr, Nd and Os isotopic composition of mantle xenoliths, and the SCLM-like trace element chemistry pattern of the Lower Zone (Carlson et al., 1999; Maier et al., 2005; Richardson and Shirey, 2008, Wilson et al., 2017). However, it is unlikely that the asthenospheric source of the RLS magma had a signal of surface-derived sulfur such as what is observed in ocean island basalts, given how different the processes that generate these magmas are.

At this point, there is no way to reconcile the petrogenetic constraints from the multiple isotopic systems into one single story. Although the presence of a MIF sulfur component implies the presence of Archean surface material in a mantle-derived magma, sulfur isotopes alone do not provide conclusive evidence for one source of sulfur over the others. The results of this study suggest that sulfur from multiple sources were incorporated into the magma in order to generate the measured Sr, S, and Nd isotope compositions and that different layers assimilated sulfur from different sources.

Chapter 3: The sulfur composition of the Lower Bushveld Series

3.1. Abstract

The Basal Ultramafic Sequence (BUS) was recently discovered and described as the most basal unit of the Rustenburg Layered Suite (RLS). The BUS, together with the Marginal Zone, and the Lower Zone, form the Lower Bushveld Series (LBS) and represent the early stages of the emplacement of the RLS.

Previous work has shown that the RLS has a sulfur signature unlike that expected from a melt derived from unaltered mantle ($\Delta^{33}S = 0 \pm 0.008‰$), and that subtle shifts of composition within the stratigraphy suggest that there are multiple contaminants in this intrusion. In this study, we look at the sulfur composition of the LBS as sampled by a drill core at the Clapham Section. In addition to sulfide, some samples of the BUS have primary sulfate, which makes it one of the few localities worldwide of a mafic magma with sulfate.

Like the RLS, the Lower Bushveld Series also has a non-zero $\Delta^{33}S$, unlike primitive mantle, and exhibits some variability in $\Delta^{33}S$ with stratigraphic depth. The BUS has the lowest values in the entire RLS (avg. sulfide $\Delta^{33}S = 0.057‰$) and the Marginal Zone, considered residual liquid from the BUS, has the highest values of $\Delta^{33}S$, up to 0.322‰. These higher values for the Marginal Zone are associated with layers with pelite xenoliths. The lack of any levels with sulfur having $\Delta^{33}S = 0$ in any of the RLS units, including the most primitive magmas (BUS) continues to support the hypothesis that the intruded melts carried a mass independent signature at the time of injection, and keeps open the possibility that some part of the $\Delta^{33}S$ signature originates at the source of primitive Bushveld magmas.

3.2. Introduction

The Marginal and the Lower Zones of the Bushveld were often considered to be the lowermost zones of the Rustenburg Layered Suite, until a mining drill core exposed rocks beneath the Marginal Zone, subsequently named as the Basal Ultramafic Sequence (Wilson, 2015). The Basal Ultramafic Sequence (BUS), a 750m layered sequence that comprises ultramafic and mafic rocks, represents the most primitive part of the Rustenburg Layered Suite. The BUS records the first stage of emplacement of the intrusion, which has been shown to have a different, more primitive composition than the Lower Zone, indicating a different initial magma composition and also different evolution story (Wilson et al., 2017). The grouping of the Lower Zone, Marginal Zone, and BUS is referred to as the "Lower Bushveld Series" (Wilson et al., 2017; LBS).

In this chapter I present the first multiple sulfur isotopic composition data of the LBS and assess how it relates to what is observed in the main Bushveld series. Being the earliest magmas of the RLS, the LBS can be regarded as the most representative sample available of the initial magma composition (Wilson, 2015), and could therefore better represent the initial sulfur isotopic composition of the intrusion. Insight from the sulfur isotope composition of these rocks and comparisons with other BMP rocks may also provide important insights into the larger question of whether the deep melts already carried a signal of exogenic sulfur.

Unlike the Main Bushveld Series (MBS), the LBS is not mineralized. Moreover, the BUS and the Lower Zone contain anhydrite, a calcium sulfate. The occurrence of anhydrite in the LBS was first described by Wilson et al. (2017), but no further studies have been conducted since then. Therefore, this chapter will also explore the relationships between sulfide and sulfate, by

examining the sulfur isotope composition in the light of petrography of silicate, sulfide, and sulfate minerals.

3.3. Background

3.3.1. The Clapham Section

Until recently, the Marginal Zone was considered to be the most basal sequence in the RLS, given evidence for interaction of the magma with the footwall rocks. However, drill core sampling of the Clapham Section, a compartment in the Eastern Limb of the Rustenburg Layered Suite, revealed that in some locations, the Marginal Zone is underlain by the Basal Ultramafic Sequence (BUS). The Clapham Section has been sampled via three drill cores totaling 2100m in length (Wilson, 2012; Wilson, 2015; Wilson et al., 2017), two of which were analyzed for this study, CH6 and CH7. The drill cores sample all units of the LBS (Figures 3.1a; 3.1b).

The BUS comprises harzburgite, dunite, and orthopyroxenites that accumulated in structural troughs and were inferred to have crystallized from an ultramafic primitive magma with 19 wt% MgO (Wilson, 2015). Occurrences of these ultramafic rocks have been described in three locations: Olifants River, Clapham, and Burgersfort, and each location presents a different stratigraphy, which reinforces the interpretation that their crystallization occurred separately. These rocks contain sulfide, but anhydrite has also been observed. This was the first observation of anhydrite in the Rustenburg Layered Suite. Since then, anhydrite has also been described in the Northern Limb (Yudovskaya et al 2018), where it was proposed to be the product of in-situ assimilation of an anhydrite-rich host rock. Observations from the BUS are also relevant because

they bear on the question of whether a similar assimilation process is supported for rocks crystallized deeper/earlier in the evolution of the BMP.

In the Clapham Section, the Marginal Zone is ca. 430 meters thick and mostly consists of norite and orthopyroxenite, having been thought to have developed directly from accumulation of low-density felsic magma that resulted from the fractional crystallization of the BUS (Wilson, 2015; Wilson et al., 2017). Xenoliths of country-rock within norites mark the interaction between the magma and the metapelites forming roof of the magma chamber (Wilson, 2015). Replenishment of the chamber with new incoming magma is responsible for a reversal in pyroxene composition at the contact between Lower and Marginal Zones (Wilson, 2015).

Discontinuities in geochemical trends in the BUS, Marginal Zone, and Lower Zone, show that the magma that was being emplaced was not of uniform composition at the time of emplacement. Four geochemical reservoirs are needed to explain the observed mineral compositions (e.g. Mg# in olivine and orthopyroxene), trace element patterns, and Sr isotope compositions. These include contributions from the primitive mantle, subcontinental lithospheric mantle (SCLM), lower crust of the Kaapvaal Craton, and metapelites of the Pretoria Group (Wilson et al., 2017), based on field, petrological, and isotopic evidences.

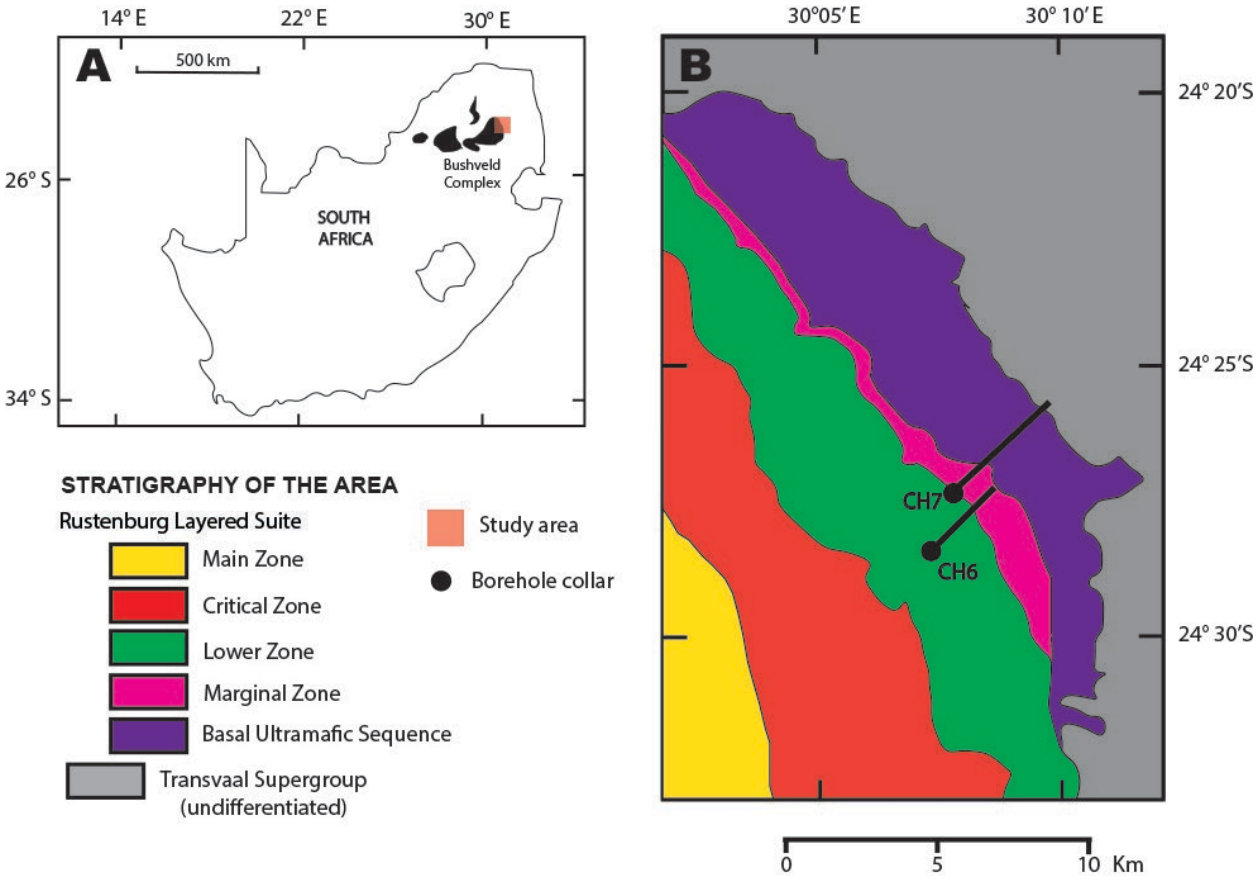

Figure 3.1. (a) Location of the study area within the country of South Africa; **(b)** location of the boreholes CH6 and CH7, where the samples in this study were collected.

3.3.2. Occurrence of anhydrite in mafic magmas

The first occurrence of anhydrite in the Rustenburg Layered Suite was described by Wilson et al. (2017). They reported magmatic anhydrite as an ubiquitous mineral in the BUS, and as well as in samples from the Lower Zone. Anhydrite-bearing mafic rocks were recently discovered in the Northern Limb (Turfspruit farm), but such occurrence was interpreted by Yudovskaya et al. (2018) to be the result of assimilation of anhydrite-rich sediments by an ultramafic melt.

Globally, the occurrence of anhydrite-bearing magmas is uncommon and typically associated with arc magmatism (Luhr, 2008; Ripley et al., 2010). The first reported occurrence of primary magmatic anhydrite was found in the trachyandesitic pumices from the El Chichón volcano in Mexico (Luhr et al., 1984), which contained anhydrite both in the matrix of the pumice but also as inclusions in the silicate minerals. Other occurrences of primary magmatic anhydrite include Mt. Pinatubo dacites (Evans and Scaillet, 1997), Julcani rhyodacites (Drexler and Munoz, 1995), Piedras Grandes andesite (Matthews et al., 1999), Eagle Mountain andesite (Parat et al., 2002), and Redoubt Volcano andesites (Nye et al., 1994; Swanson and Kearney, 2008), among others. These intermediate-to-felsic magmas are water-rich and oxidized (>NNO+1; Luhr, 1998), with a main mineralogy of hornblende and plagioclase. Experimental work by Carroll and Rutherford (1988) and Jugo et al. (2005) showed that sulfide and sulfate can coexist in a magma under a restricted range of oxygen fugacities, between ΔFMQ +1.5 and ΔFMQ +2, where sulfide is stable with values below ΔFMQ +1.5, and sulfate will be the sulfur species when the oxygen fugacity is above ΔFMQ +2. One factor that may contribute to the scarcity of magmatic anhydrite in the geological record could be its high water solubility; Luhr et al. (1984) demonstrated that anhydrite was completely dissolved from the rocks within one year of exposure to surface conditions.

The Kharaelakh intrusion in the Noril'sk region (Russia) is the only location, aside from the RLS, where coexisting sulfide and sulfate have been reported in mafic magmas (Li et al., 2009; Ripley et al., 2010). Kharaelakh (previously known as NW Talnakh; Ripley et al., 2010) is a Ni-Cu-(PGE) mineralized sill, formed during the magmatism that generated the Siberian Traps, another large igneous province (Starostin et al., 2011). At this location, assimilation of a sulfate-bearing country rock, where the sulfate has high $\delta^{34}S$ (18.8‰-22.8‰), is required to produce the

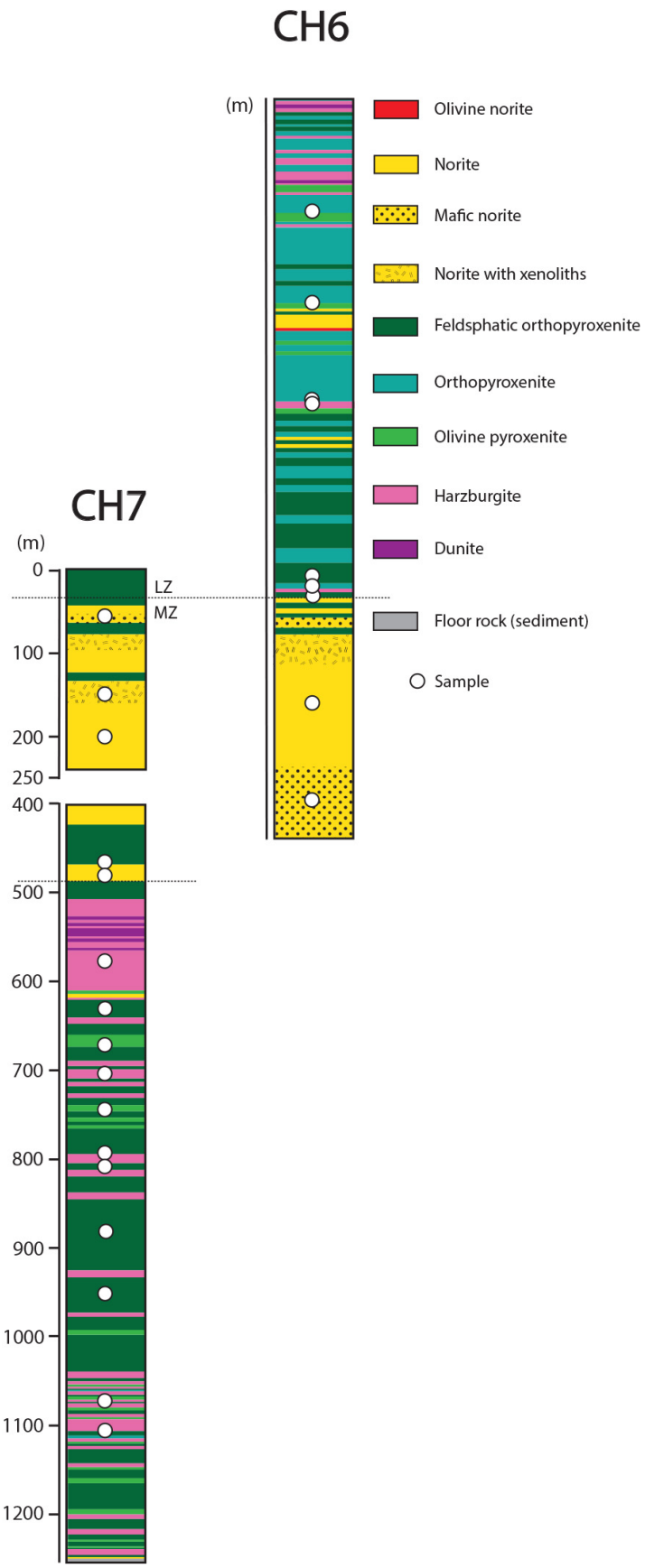

Figure 3.2. Detailed stratigraphy of the drill cores CH6 and CH7, showing their lithologies and unit subdivision. White circles correspond to samples analyzed. The floor rock is the Magaliesberg quartzite of the Pretoria Group (Transvaal Supergroup). Sketched after Wilson, 2015.

higher $\delta^{34}S$ sulfide values (chalcopyrite values of 9.3‰-13.2‰) and to explain the presence of anhydrite in the rock (Ripley et al., 2010). Therefore, the sulfide values would represent a mixture between a mantle-derived sulfide, and sulfate-reduced sulfide, while the sulfate would represent the preserved sedimentary anhydrite.

3.4. Methodology

The 25 samples studied here come from the two distinct drill cores (CH6 and CH7, Figures 3.2) through the Clapham Section, which have been described in more detail by Wilson (2015). Eleven samples represent the BUS, seven samples represent the Marginal Zone, and seven samples from the Lower Zone. The depth was calculated based on their known depth within each core, adjusted to the composite depth of the Clapham Section described by Wilson (2015). The mineral abbreviations used in this chapter are: opx (orthopyroxene), cpx (clinopyroxene), ol (olivine), plag (plagioclase), kfs (K-feldspar), bt (biotite), sulf (sulfides), anh (anhydrite), rt (rutile), ap (apatite), and chr (chromite). The estimate of ferric iron (Fe^{3+}) was made through charge balance based on the charge relationship between cation and oxygen (Droop, 1987).

Ten samples were chosen for petrographic and mineral chemical analyses based on lithology and stratigraphic position, aiming to cover a diverse range of rock types in the different units of the LBS. The thin sections were made using oil instead of water, in order to preserve potential anhydrite. The mineral chemistry of silicate, sulfide, and sulfate phases was determined using the JEOL 8530F electron probe microanalyzer (EPMA) at the Geophysical Laboratory, Carnegie Institution for Science. The WDS (wave-dispersive X-ray spectroscopy) operating

conditions were: accelerating voltage of 15 kV, beam current of 20 nA, and variable beam diameter from 1-5μm, depending on size of the mineral. Analyses reported in this study have compositional totals between 99.5 wt% and 101.5 wt%. The same equipment was used to take backscatter electron (BSE) images. Whenever the grain was too small to conduct a satisfactory WDS measurement, the identification was done using a qualitative method (EDS – energy-dispersive X-ray spectroscopy), using accelerating voltate of 15 kV, aperture of 60 μm, and working distance of 8 mm.

The multiple sulfur isotope composition of various forms of sulfur were measured. Individual aliquots of sample rock powder were extracted using a chromium reduction method (described below) to yield data referred to as "total sulfide". A separate set of individual aliquots of sample rock powder were extracted using a solution known as "Thode" solution (also described below), referred henceforth to as "Thode extracts". Initially, these experiments were conducted to test for sulfate extraction; however it was found that the Thode solution extracts total monosulfide and total sulfate. This extract is not referred to as total sulfur because the efficacy of Thode solution for extracting disulfide (pyrite) is not efficient, but pyrite concentrations are generally low in these samples, meaning that the Thode extracts are good proxies for total sulfur. A third form of sulfur (referred to as "water-soluble sulfate") was extracted from water-soluble fractions using this same Thode solution. All analyses were conducted at the Stable Isotope Laboratory of the University of Maryland, College Park.

The chromium solution consists of a mixture of 20 mL of 5N HCl and 20 mL of a 0.3M Cr (II) reducible solution (Canfield et al., 1986). Samples are reacted with this solution in a heated boiling flask that is purged with flowing nitrogen gas to carry evolved hydrogen sulfide from the solution. The reaction is allowed 3 hours to complete. The Thode solution (Thode et al.,

1961; Arnold et al., 2014) is a mixture of concentrated hydrochloric, hydriodic, and hypophosphorous acids (52%, 32%, 16%, by volume; Thode et al., 1961; Arnold et al., 2014). Samples are reacted with Thode solution in a heated boiling flask, also with a 3-hour reaction time and also with evolved hydrogen sulfide carried by flowing nitrogen gas. In both cases, the hydrogen sulfide is passed through a condenser and a water trap to remove chloride and then collected as silver sulfide (Ag_2S) by reaction with 20 mL of a 0.03M silver nitrate solution.

Deoxygenated MilliQ water was used to extract water-soluble sulfate, in a step previous to the sulfur extraction chemistry. The sulfate was then precipitated as $BaSO_4$ by addition of 1 mL of 1M $BaCl_2$. This $BaSO_4$ was centrifuged, and reacted with Thode solution under the same conditions as described above. As there was no evidence for insoluble sulfate from petrographic studies or in the BUS literature, the residue was not analyzed. The expression $\Delta_{sulfate\text{-}sulfide}$ (c.f. O'Neil, 1986) will also be used to represent the difference in $\delta^{34}S$ values between sulfate and sulfide.

Silver sulfide precipitates were aged for at least one week in the dark, and then washed in 6 steps with MilliQ water and ammonium hydroxide. Once dry, 3 mg of silver sulfide were weighed and put into an aluminum capsule. The capsule was dropped inside a Ni vessel heated to 250°C, and fluorine was added and left to react overnight. The reaction produces the gas SF_6, which is then separated cryogenically and by gas chromatography from the leftover fluorine and other contaminants. After purification, the SF_6 is stored in glass fingers in a manifold, and analyzed for the sulfur isotope composition using the the Finnigan MAT 253 dual inlet isotope ratio mass spectrometer by monitoring SF_5+ ion beams at 127, 128, 129, and 131 Da.

The sulfur isotopic composition is described in terms of the delta (equation 3.1) and capital delta (equation 3.2) notations,

$$\delta^{3X}S = \left[\frac{\left(\frac{^{3X}S}{^{32}S}\right)_{\text{sample}}}{\left(\frac{^{3X}S}{^{32}S}\right)_{\text{REF}}} - 1\right] \quad (3.1)$$

$$\Delta^{33}S = \delta^{33}S - [(1 + \delta^{34}S)^{0.515} - 1] \quad (3.2)$$

which are reported in units of permil (‰) relative to independent measurements of CDT (Canyon Diablo Troilite), since a V-CDT value for $\Delta^{33}S$ and $\Delta^{36}S$ has not been established. This is consistent with the procedure done in our recent meteorite studies (Antonelli et al., 2014; Dottin et al., 2018). On this scale, IAEA S-1 will have a $\delta^{34}S$ of -0.394‰ and $\Delta^{33}S$ and $\Delta^{36}S$ of 0.116‰ and -0.795‰, respectively. Independent measurements indicate that the $\Delta^{33}S$ and $\Delta^{36}S$ of the Earth is within error of 0‰ for both capital delta values (Labidi et al., 2013; Wing and Farquhar, 2015). Errors are based on long-term standard reproducibility of fluorinations of IAEA-S1, which yields 2σ variations of $\delta^{33}S$±0.15‰; $\delta^{34}S$±0.30‰; and $\Delta^{33}S$±0.016‰. For purposes of comparison, we also have renormalized data from prior studies of Penniston-Dorland et al., 2012, and Magalhães et al., 2018, to this same scale. Those data are presented in Appendix A.

Samples of metasediments from the Magaliesberg Quartzite, Lakenvalei Quartzite, and Vermont Pelite were also analyzed for their sulfur isotopic composition, but have not yielded any sulfur (i.e. they do not contain sulfur).

3.5. Results

3.5.1. Petrography

The ten samples described in detail encompass the Marginal Zone and the BUS, and thus these two units will be the focus of this study. The main mineral phases in these rocks are orthopyroxene, clinopyroxene, and plagioclase, always coexisting. Olivine, biotite, quartz, and K-feldspar are present in some samples in significant quantities (>10 modal %), but appear only in specific samples. Accessory phases include chromite, apatite, zircon, rutile, magnetite, sulfides (pyrrhotite, pentlandite, pyrite, and chalcopyrite), and anhydrite (Figure 3.3).

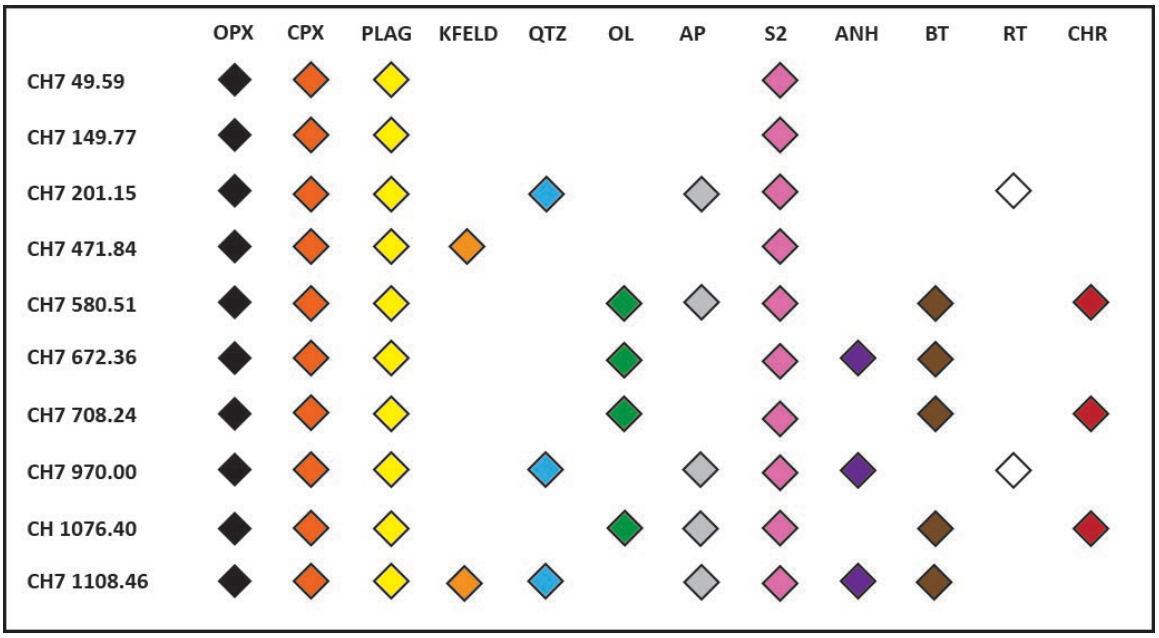

Figure 3.3. Mineral composition of the studied samples from the Clapham Core. This figure does not present modal percentages, and the variation in the amount of each mineral between samples is not portrayed.

3.5.1.1. Pyroxenes

Both orthopyroxene and clinopyroxene are present in all the rocks. Orthopyroxene is very enstatite-rich, from En_{68} to En_{88}. Clinopyroxene has a diopside composition (Table 3.1, Figure 3.4a). Neither orthopyroxene nor clinopyroxene exhibit growth zoning, but overgrowths of a different composition are observed in Opx in a few samples. Exsolution lamellae of clinopyroxene within orthopyroxene is common (Appendix A, Figure A.4), and can range from very fine grained needle-like lamellae to large "blebs". The fine-grained lamellae can interfere with the pyroxene analysis (Figure 3.4a).

The orthopyroxenes are Mg-rich, with a Mg# from 71.5 up to 89.9 (Table 3.1, Figure 3.4b). The Marginal zone orthopyroxenes present consistently lower values of Mg#, while it is variable in the BUS, with slightly lower values in the bottom of the rock pile and higher values in the upper portion. The findings are consistent with the behavior observed by Wilson (2015), who reported a similar behavior of orthopyroxene in the Clapham Section.

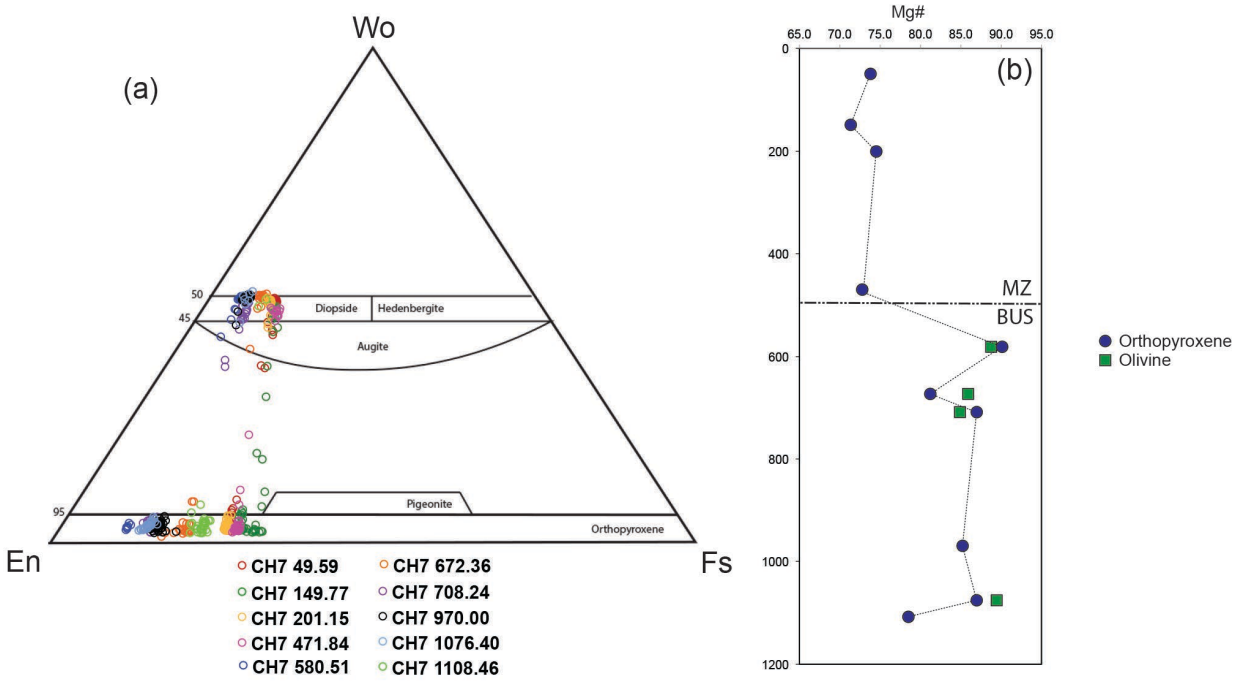

Figure 3.4. a. Wo-En-Fs classificatory diagram for pyroxenes from drill core CH7. b. Variation of Mg# with depth in orthopyroxene (blue circle) and olivine (green square).

3.5.1.2. Feldspar

Plagioclase is the dominant feldspar in the LBS samples. Minor anhedral K-feldspar provides evidence for exsolution of high temperature ternary feldspars on cooling (see Fig 3.5a). The composition of plagioclase varies from sample to sample and even within samples, encompassing a wide range of anorthite contents, from An_{85} to An_{30}. Most samples have zoned interstitial plagioclase, always in a pattern of a Ca-rich core to a Na-rich rim. In some cases, it is

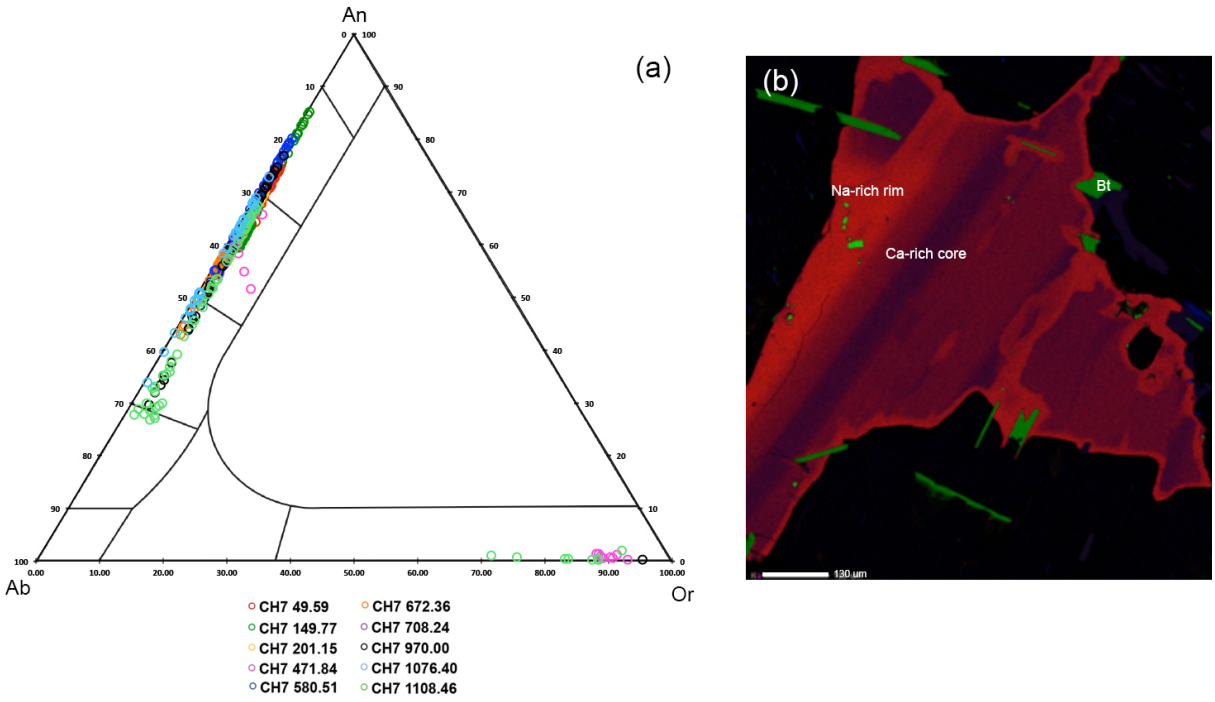

Figure 3.5. a. An-Ab-Or classificatory diagram for feldspar shows two distinct groups of feldspar: the predominant is plagioclase; the Ca-rich variety. In a lesser amount, K-feldspar (orthoclase) is also present. **b.** Ca-Na-K compositional map of feldspar from sample CH7 1108.46, showing a "euhedral" Ca-rich core, with strong zoning filling in for the interstitial spaces, where an "anhedral" Na-rich rim formed.

Table 3.1. Mineral composition of orthopyroxene from samples studied. Results shown here correspond to average of all measurements of orthopyroxene in a sample (total amount given by n). The Mg# is calculated based on the average composition.

ORTHOPYROXENE										
Sample	CH7	149.77	201.15	471.84	580.51	672.36	708.24	970.00	1076.40	1108.46
n	21	37	44	33	8	24	15	28	32	30
Na2O	0.02	0.01	0.01	0.01	0.02	0.02	0.07	0.03	0.02	0.03
FeO	16.79	18.47	16.69	17.83	6.77	12.71	8.42	9.65	8.77	13.99
TiO2	0.13	--	0.18	--	0.14	0.11	--	--	0.05	--
K2O	0.00	0.00	0.00	0.00	0.00	0.00	0.00	0.00	0.00	0.00
Al2O3	1.11	0.80	0.82	0.96	1.14	1.32	1.41	1.18	1.35	1.34
MgO	26.77	26.00	27.24	26.79	33.98	30.54	31.04	31.30	32.59	28.67
MnO	0.31	--	0.29	--	0.16	0.23	--		0.18	--
Cr2O3	0.31	0.11	0.24	0.18	0.35	0.33	0.54	0.32	0.53	0.25
CaO	1.41	1.20	1.05	0.91	1.04	0.95	2.80	1.91	1.19	1.18
SiO2	54.18	54.41	54.46	54.44	56.65	54.40	55.87	55.60	56.49	54.36
NiO	0.06	0.06	0.06	0.07	0.09	0.12	0.11	0.09	0.14	0.10
Total	101.08	101.05	101.06	101.19	100.34	100.73	100.28	100.08	101.32	99.90
Mg#	74.0	71.5	74.4	72.8	89.9	81.1	86.8	85.3	86.9	78.5

Table 3.2 Mineral composition of clinopyroxenes from the Clapham Section. Results shown here correspond to average of all measurements of clinopyroxene in a sample (total amount given by n). Measurements of exsolved Cpx from sample CH7 49.59 are also presented.

CLINOPYROXENE											
Sample	49.59	49.59 Exs	149.77	201.15	471.84	580.51	672.36	708.24	970.00	1076.40	1108.46
#	25	8	25	15	12	14	17	15	23	7	2
Na_2O	0.31	0.34	0.25	0.33	0.34	0.48	0.57	0.33	0.34	0.50	0.42
FeO	6.78	6.19	7.25	6.25	7.11	2.81	5.14	6.25	5.57	3.48	5.17
TiO_2	0.24	0.24	--	0.34	--	0.27	0.32	0.34	--	0.25	
K_2O	0.00	0.00	0.00	0.01	0.00	0.00	0.04	0.01	0.70	0.00	0.00
Al_2O_3	1.82	1.73	1.40	1.34	1.71	2.00	2.92	1.34	2.33	2.29	1.43
MgO	15.89	15.51	16.11	15.95	15.60	17.49	16.08	15.95	21.36	16.92	16.15
MnO	0.17	0.15	--	0.15	--	0.08	0.11	0.15	--	0.09	--
Cr2O3	0.61	0.66	0.21	0.45	0.32	0.97	0.78	0.45	0.50	0.86	0.32
CaO	22.49	23.56	21.94	23.10	22.26	23.15	22.74	23.10	14.78	23.46	23.36
SiO2	52.65	52.85	53.54	53.16	53.10	53.34	52.06	53.16	54.63	53.42	52.97
NiO	0.05	0.05	0.04	0.04	0.04	0.06	0.06	0.04	0.07	0.07	0.05
Total	101.01	101.29	100.74	101.11	100.48	100.67	100.84	101.11	100.28	101.35	99.86

Table 3.3. Mineral composition of plagioclase from the Clapham Section. Results shown here correspond to average of all measurements of plagioclase in a sample (total amount given by n).

FELDSPAR										
Sample	CH7 49.59	149.77	201.15	471.84	580.51	672.36	708.24	970.00	1076.40	1108.46
#	37	52	39	43	27	24	26	33	31	64
SiO_2	49.79	51.66	51.62	54.97	51.90	52.82	50.31	54.80	53.11	56.40
TiO_2	0.02	0.02	0.02	0.04	0.02	0.02	0.03	0.02	0.02	0.02
Al_2O_3	30.35	31.11	30.84	28.34	29.15	29.88	32.41	29.82	30.23	28.60
FeO	0.95		0.22		0.49	0.22			0.07	
MgO	1.13		0.02		1.85	0.02			0.01	
CaO	14.21	13.77	13.05	10.24	11.76	11.76	14.91	11.66	11.90	10.41
Na_2O	2.84	3.63	3.98	3.98	4.33	4.78	3.27	4.66	4.79	5.27
K_2O	0.19	0.28	0.21	2.51	0.17	0.12	0.06	0.23	0.06	0.33
BaO	0.00	0.03	0.00	0.13	0.02	0.01	0.05	0.04	0.03	0.01
SrO	0.05	0.08	0.05	0.10	0.06	0.09	0.07	0.07	0.09	0.07
Total	99.54	100.58	100.01	100.29	99.75	99.71	101.11	101.30	100.30	101.11
Avg. An	71.76	66.28	63.71	58.76	59.50	53.05	71.29	60.01	57.80	52.83

possible to distinguish a subhedral to euhedral core of plagioclase, and compositional zoning towards a more Na-rich plagioclase composition, where the borders of the crystals are very Na-rich (Figure 3.5b). K-Feldspar is a minor occurrence in few samples and is usually is associated with the interstitial phases.

3.5.1.3. Olivine

Olivine is present in only four of the analyzed samples. In three of those, it is the main mineral constituent and forms euhedral grains in a cumulate texture. The most abundant interstitial material varies from biotite in sample CH7 708.24, to clinopyroxene in sample 580.51. In sample 672.36, olivine is rare and only two grains were found in the thin section.

The Mg# of the olivine of all samples is high. (Table 3.4; Figure 3.4), with values from 85-89. This is a small range of variation when compared to orthopyroxene.

3.5.1.4. Accessory phases

Biotite is a main mineral in sample 708.24, as it appears as an intercumulus mineral, surrounding olivine (Figure 3.6a). However, biotite appears as small grains in other samples. Biotite is interpreted to be igneous in origin. Apatite is present in many samples and has varying textures, from euhedral to anhedral. It has compositional variation in some samples, while in others it is homogeneous. It can be rich in Cl and/or F (Appendix A). Quartz appears as an intercumulus phase in a few samples, but never associated to olivine, usually as large shapeless grains. Biotite and apatite compositions can be found in Appendix A.

Table 3.4. Composition of olivine from the Clapham Section. Results shown here correspond to average of all measurements of olivine in a sample (total amount given by n).

OLIVINE				
Sample	580.51	672.36	708.24	1076.40
n	30	2	140	40
Na_2O	0.00	0.00	--	0.00
FeO	9.35	13.42	14.11	12.45
TiO_2	0.01	0.00	0.01	0.01
K_2O	0.00	0.00	--	0.00
Al_2O_3	0.01	0.01	0.02	0.01
MgO	49.45	45.67	44.29	46.79
MnO	0.14	0.17	0.19	0.15
CaO	0.02	0.00	0.02	0.01
SiO_2	40.64	39.73	41.19	40.26
NiO	0.49	0.84	0.46	0.69
Total	100.11	99.85	100.29	100.38
Mg#	88.8	85.9	84.8	89.4

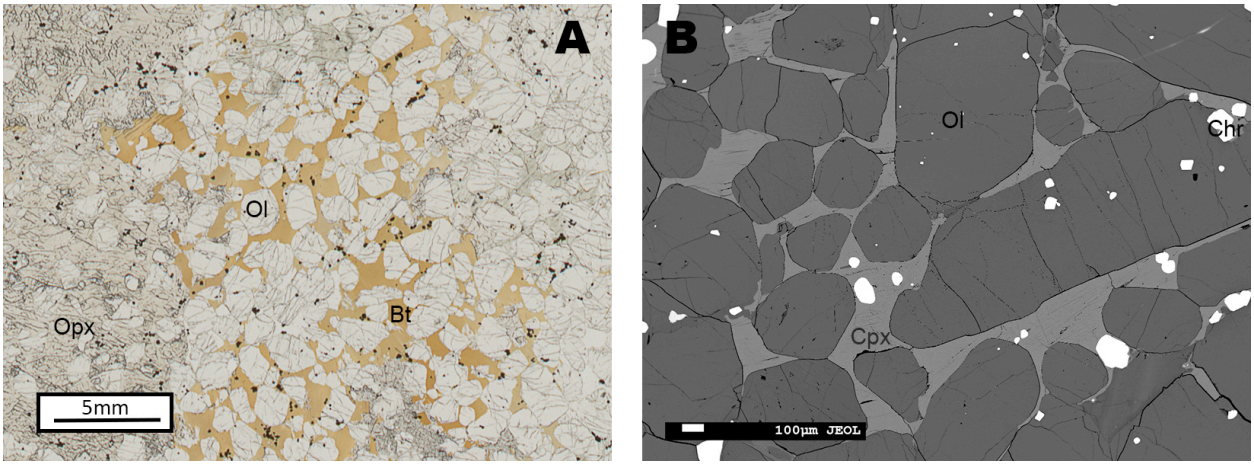

Figure 3.6. a. Scan of thin section CH7 708.24, where it is possible to see cumulate olivine enclosed by biotite; **b.** Cumulate olivine in sample CH7 580.51, where the intercumulus material is clinopyroxene.

3.5.1.5. Sulfur-bearing phases

All samples analyzed contain sulfides as accessory minerals. The sulfides are pentlandite (pn; $[Fe,Ni]_9S_8$), chalcopyrite (ccp; $FeCuS_2$), pyrite (py; FeS_2), and pyrrhotite (po; $Fe_{1-x}S$), that occur as single grains or in mineral aggregates that show intergrowth and/or exsolution features (Figures 3.7a; 3.7b). In most samples, the sulfide grains are very small (< 20μm), and not abundant.

We observe anhydrite (anh; $CaSO_4$) in three thin sections (CH7 672, CH7 970, and CH7 1108). Following the chemistry procedure described in the methods section, we identify significant concentrations of soluble sulfate in at least 5 samples within the CH7 core (the three aforementioned, plus CH7 749.68 and CH7 884.85); considering the presence of anhydrite in some samples, we will proceed with the assumption that the soluble sulfate present in these other samples is also anhydrite.

When present, anhydrite can be as abundant as the sulfides. Anhydrite is normally found as single crystals up to >200μm in diameter (Figure 3.7a), that are commonly surrounded by small grains of pyrite (Figure 3.7c), suggesting reduction on cooling. Anhydrite has also been observed as an inclusion in pyroxene (Figure 3.7d), and in contact with larger sulfides (Figure 3.7a, 3.7b) or associated with apatite (Figure 3.7f). In the samples with anhydrite, sulfide can also be associated with grains of magnetite (mag), including encapsulating it (Figure 3.7e).

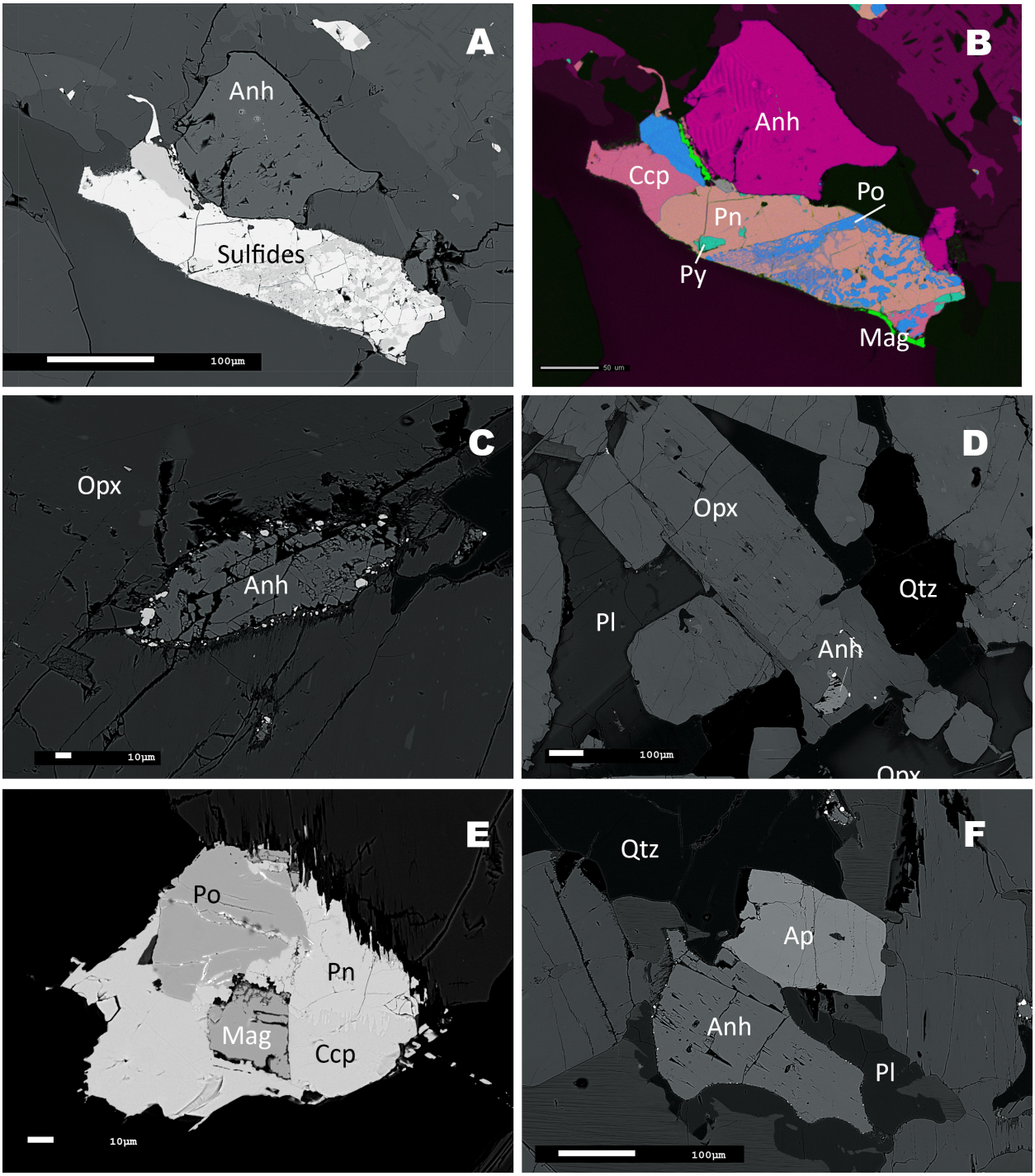

Figure 3.7. Images showing diverse anhydrite textures observed in samples CH7 970.00 and CH7 1108.46. **3.7a.** Coexisting sulfides and anhydrite; **3.7b.** Fe-Ni-S-Cu-Ca compositional map of the coexisting sulfide and anhydrite from figure a; **3.7c.** Pyrite grains growing on the rim of an anhydrite crystal, **3.7d.** inclusion of anhydrite in zoned orthopyroxene; **3.7e.** Sulfide aggregate with magnetite in the core; **3.7f**. anhydrite associated with apatite.

3.5.2. Sulfur Isotopes

The sulfur isotope composition of total sulfide, water-soluble sulfates, and the Thode extracts (proxy for total sulfur) of the Clapham core is given in Tables 3.5, 3.6, and 3.7, and shown in Figure 3.8. We compare these values to the previously measured values of the adjacent units of the Rustenburg Layered Suite (Penniston-Dorland et al., 2012; Magalhães et al., 2018), and to the values of MORB (Sakai et al., 1984, Chaussidon et al., 1991, Peters et al., 2010, Labidi et al., 2014), representing an uncontaminated mantle. The sulfur isotopic composition is variable in both $\delta^{34}S$ and $\Delta^{33}S$ for both sulfide and sulfate in this drill core; this variability occurs both within and between units (Figure 3.9).

The sulfur isotopic composition of the Clapham Core sulfides shows clear distinctions between the three zones of the LBS: $\Delta^{33}S$ = 0.057‰ (±0.018 s.d.), $\delta^{34}S$ = 3.29 (±2.99‰ s.d.) for the sulfides in the BUS; $\Delta^{33}S$ = 0.216‰ (±0.087 s.d.) and low $\delta^{34}S$ = 2.02‰ (±1.14 s.d.) in the Marginal Zone; $\Delta^{33}S$ = 0.106‰ (±0.040 s.d.), $\delta^{34}S$ = -0.18‰ (±4.71 s.d.) in the Lower Zone. $\Delta^{33}S$ is resolved from zero in all cases and has the most positive values in the Marginal Zone. The $\delta^{34}S$ is markedly positive for the BUS compared to the other zones. The Lower Zone has $\Delta^{33}S$ and $\delta^{34}S$ that are most similar to that already seen in the RLS (Chapter 2). The high $\Delta^{33}S$ values observed for the Marginal Zone (up to 0.322‰ in sulfides) are not accompanied by significant changes in $\delta^{34}S$ values (1.08‰-4.36‰), except for one Thode extract sample with a $\delta^{34}S$ of -22.71‰.

Omitting one significant exception from the Marginal Zone with $\delta^{34}S$ = -22.8‰, the $\delta^{34}S$ for Thode extract sulfur is, on average, similar to those observed for sulfide in the Lower and Marginal Zones (Lower Zone: 1.45‰±2.01‰, Marginal Zone: 1.95‰±0.52‰), and slightly higher in the BUS, where $\delta^{34}S$ = 4.52‰±2.34‰. Only five samples, all from the BUS, yielded

water-soluble sulfate in measurable quantities, compatible with the slightly higher $\delta^{34}S$ in the Thode extract values. The $\delta^{34}S$ is more positive than the sulfide (4.12‰±2.84‰ s.d.), while the $\Delta^{33}S$ for these are within error of the sulfides ($\Delta^{33}S$ =0.070‰±0.17‰ s.d.). The five measured $\Delta^{34}S_{sulfate\text{-}sulfide}$ range from 0.4 to 4.0‰ with a median value of 2.9 ‰ which corresponds to an equilibrium sulfate-sulfide fractionation temperature of ~1200°C (calculated using Eldridge et al., 2016). Note that I interpret the $\delta^{34}S$ value of sample CH7 749.68 (0.45‰) as not representative of the value of actual anhydrite, given the similarity with the values of the sulfides (0.08‰).

While the average $\Delta^{33}S$ matches between measurements of sulfides and water-soluble sulfates, ten samples exhibit differences in $\Delta^{33}S$ between sulfide and total sulfur greater than 0.020‰, and three samples exhibit differences in $\Delta^{33}S$ greater than 0.050‰ (0.06‰, 0.10‰, and 0.11‰). The two most extreme samples exhibit different $\delta^{34}S$ by 11‰ and 24‰ between total sulfur and sulfide analyses.

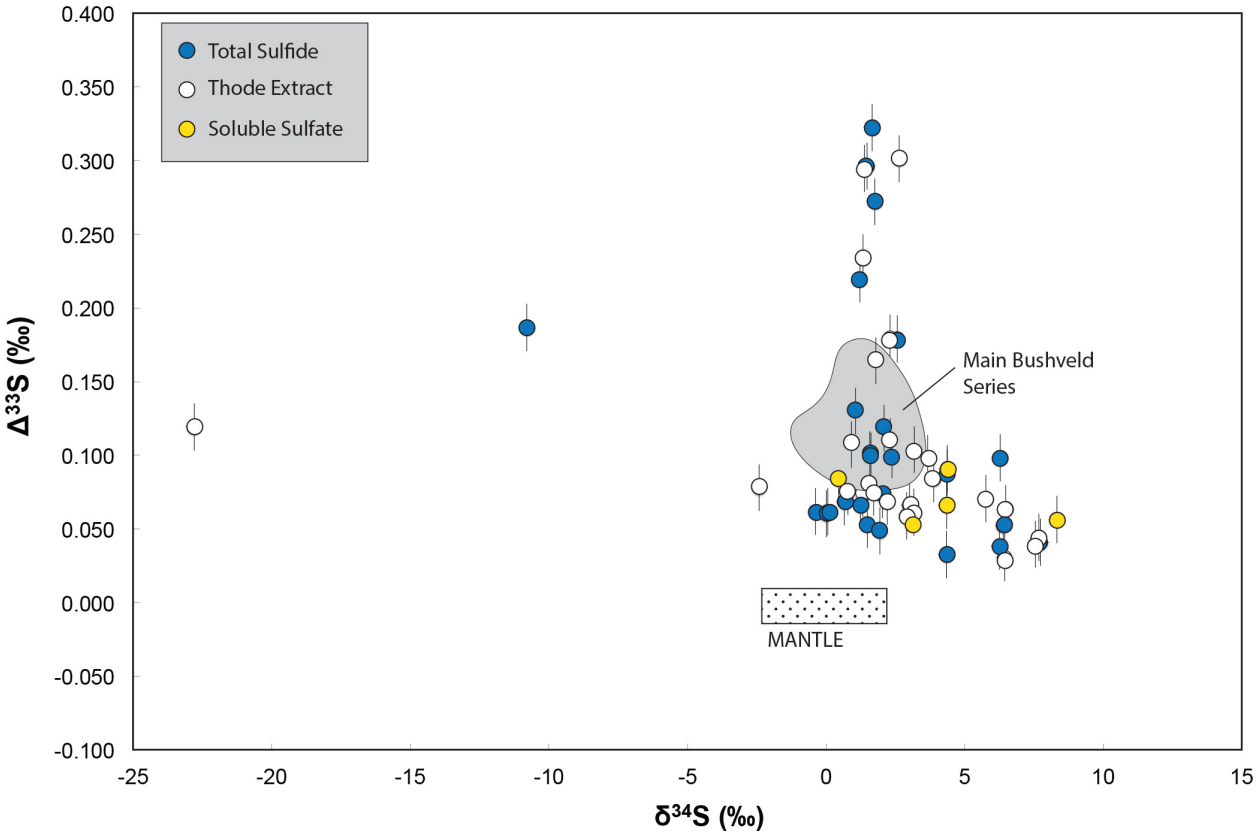

Figure 3.8. Sulfur isotope composition of total sulfide, Thode extract, and soluble sulfate obtained for samples of the Clapham Core. The mantle field was determined with data from Sakai et al. (1983), Peters et al. (2010) and Labidi et al. (2012). Main Bushveld Series data recalculated from Penniston-Dorland et al. (2012) and Magalhães et al. (2018) (Appendix A).

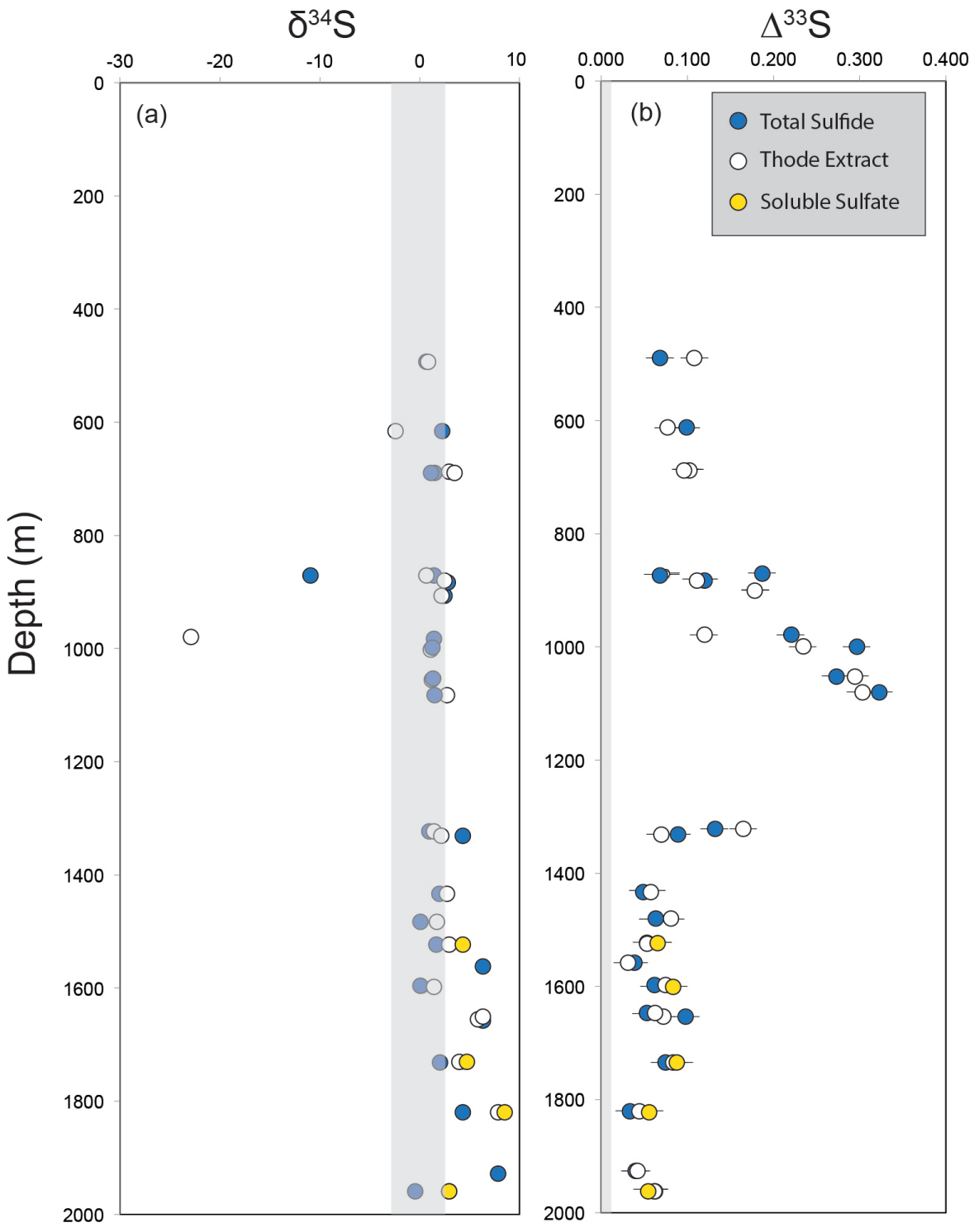

Figure 3.9. a) Variation of $\delta^{34}S$ with stratigraphic depth of the Clapham core. **b.** Variation of $\Delta^{33}S$ with stratigraphic depth. Grey rectangle corresponds to the mantle value (Sakai et al., 1983; Labidi et al., 2012). Values for $\delta^{34}S$ and $\Delta^{33}S$ are in the permil (‰) unit.

Table 3.5. Sulfur isotope composition of total sulfide extracts from the Clapham Core, organized by stratigraphic depth.

Core	Zone	Depth (m)	$\delta^{33}S$	$\delta^{34}S$	$\delta^{36}S$	$\Delta^{33}S$	$\Delta^{36}S$	Corrected Depth (m)
CH6	Lower	59.83	0.410	0.662	1.333	0.068	0.074	489.83
CH6	Lower	182.70	1.291	2.317	4.288	0.099	-0.119	612.70
CH6	Lower	256.23	0.910	1.568	2.976	0.102	-0.005	686.23
CH6	Lower	256.56	0.931	1.614	3.167	0.100	0.097	686.56
CH6	Lower	439.81	-5.390	-10.799	-21.326	0.187	-0.907	869.81
CH6	Lower	441.77	0.707	1.244	2.494	0.066	0.130	871.77
CH6	Lower	450.00	1.204	2.106	4.135	0.120	0.130	880.00
CH7	Marginal	49.59	1.500	2.566	4.720	0.179	-0.162	899.59
CH6	Marginal	549.15	0.848	1.220	2.255	0.220	-0.064	979.15
CH7	Marginal	149.77	1.057	1.478	2.131	0.296	-0.679	999.77
CH7	Marginal	201.15	1.176	1.756	2.992	0.272	-0.348	1051.15
CH6	Marginal	650.00	1.177	1.661	3.124	0.322	-0.034	1080.00
CH7	Marginal	471.84	0.688	1.081	1.828	0.131	-0.226	1321.84
CH7	Marginal	481.06	2.335	4.368	8.479	0.088	0.164	1331.06
CH7	BUS	580.51	1.050	1.944	3.575	0.049	-0.122	1430.51
CH7	BUS	631.01	0.070	0.019	-0.231	0.060	-0.268	1481.01
CH7	BUS	672.36	0.820	1.489	2.588	0.053	-0.243	1522.36
CH7	BUS	708.24	3.256	6.257	11.780	0.038	-0.142	1558.24
CH7	BUS	749.68	0.100	0.075	0.020	0.062	-0.123	1599.68
CH7	BUS	798.02	3.342	6.398	12.151	0.052	-0.039	1648.02
CH7	BUS	803.63	3.329	6.282	12.040	0.098	0.070	1653.63
CH7	BUS	884.85	1.122	2.036	4.037	0.073	0.165	1734.85
CH7	BUS	970.00	2.266	4.342	8.285	0.033	0.018	1820.00
CH7	BUS	1076.4	4.021	7.743	14.864	0.041	0.102	1926.40
CH7	BUS	1108.46	-0.125	-0.364	-0.714	0.062	-0.024	1958.46

Table 3.6. Sulfur isotope composition of the Thode extracts from the Clapham Core, organized by stratigraphic depth.

Core	Zone	Depth (m)	$\delta^{33}S$	$\delta^{34}S$	$\delta^{36}S$	$\Delta^{33}S$	$\Delta^{36}S$	Corrected Depth (m)
CH6	Lower	59.83	0.582	0.920	0.421	0.108	-1.329	489.83
CH6	Lower	182.7	-1.164	-2.411	-4.652	0.078	-0.076	612.70
CH6	Lower	256.23	1.986	3.670	7.165	0.098		686.23
CH6	Lower	256.56	1.729	3.159	6.079	0.103	0.069	686.56
CH6	Lower	439.81	0.480	0.786	1.445	0.075	-0.049	869.81
CH6	Lower	441.77	0.958	1.716	3.329	0.075	0.066	871.77
CH6	Lower	450.00	1.290	2.292	4.522	0.111	0.162	880.00
CH7	Marginal	49.59	1.367	2.307	4.344	0.179	-0.044	899.59
CH6	Marginal	549.15	-11.688	-22.799	-43.632	0.119	-0.759	979.15
CH7	Marginal	149.77	0.924	1.341	2.442	0.234	-0.107	999.77
CH7	Marginal	201.15	1.011	1.392	2.327	0.294	-0.320	1051.15
CH6	Marginal	650.00	1.658	2.636	5.097	0.301	0.082	1080.00
CH7	Marginal	471.84	1.086	1.789	3.181	0.165	-0.220	1321.84
CH7	Marginal	481.06	1.208	2.213	4.154	0.069	-0.055	1331.06
CH7	BUS	580.51	1.558	2.913	5.524	0.059	-0.019	1430.51
CH7	BUS	631.01	0.859	1.511	2.640	0.081	-0.232	1481.01
CH7	BUS	672.36	1.616	3.011	5.383	0.066	-0.346	1522.36
CH7	BUS	708.24	3.344	6.444	11.760	0.031	-0.520	1558.24
CH7	BUS	749.68	0.755	1.321	2.192	0.074	-0.320	1599.68
CH7	BUS	798.02	3.399	6.486	12.444	0.064	0.085	1648.02
CH7	BUS	803.63	3.037	5.768	11.040	0.071	0.051	1653.63
CH7	BUS	884.85	2.088	3.895	7.530	0.084	0.117	1734.85
CH7	BUS	970.00	3.992	7.680	14.696	0.044	0.053	1820.00
CH7	BUS	1076.4	3.930	7.567	14.581	0.040	0.153	1926.40
CH7	BUS	1108.46	1.692	3.169	5.987	0.061	-0.042	1958.46

Table 3.7. Sulfur composition of the water-soluble sulfate from BUS samples**.**

Core	Zone	Depth (m)	$\delta^{33}S$	$\delta^{34}S$	$\delta^{36}S$	$\Delta^{33}S$	$\Delta^{36}S$	Corrected Depth (m)
CH7	BUS	672.36	2.30	4.35	8.19	0.066	-0.089	1522.36
CH7	BUS	749.68	0.32	0.45	0.82	0.084	-0.046	1599.68
CH7	BUS	884.85	2.34	4.37	8.26	0.091	-0.061	1734.85
CH7	BUS	970.00	4.34	8.34	15.81	0.056	-0.090	1820.00
CH7	BUS	1108.46	1.65	3.10	6.06	0.054	0.161	1958.46

3.6. Discussion

This discussion section will be divided in two major themes in order to allow for a more detailed discussion of the geological meaning of the data obtained. It will start with a discussion of the sulfur isotope data, focusing on the rationale for collecting the Thode extracts data obtained in this study. The second part focuses on the sulfur composition of each of the Lower Bushveld Series units and what it tells us about the early stages of the Rustenburg Layered Suite.

3.6.1. Rationale for collection of Thode extracts

The experiment of Thode extract analysis was conducted because of a low yield of sulfur during total sulfide extraction, which suggested that those samples may have contained sulfur in a form other than sulfide such as sulfate. The ubiquitous presence of sulfate-bearing minerals in the Clapham core has been described by Wilson et al., 2017, which found anhydrite in all stratigraphic levels of the BUS, and in the lower portion of the Lower Zone. However, the extraction of sulfate using Thode solution on whole-rock powder did not give a clear sulfate signature and also did not improve the yields of sulfide in samples without sulfate, as the extraction of water-soluble sulfate in these samples showed that many samples do not actually have water-soluble sulfate in significant amounts (concentrations lower than 100 ppm), different than what is reported in the literature.

The lack of a sulfate phase reflects on the calculated $\Delta_{\text{Thode extract-sulfide}}$ from the Thode extracts and total sulfide analyses in samples from the Clapham core (Table 3.5, Table 3.6), which are incompatible with the expected value in case sulfide and sulfate co-exist ($\Delta_{\text{Thode extract-sulfide}} > 0$; Table 3.7). The Thode solution extracts other types of sulfur (e.g. sulfide) from a

sample, including minerals such as pyrrhotite, and can explain why the sulfide and Thode extract values are similar in some of the samples where anhydrite is not present. Other types of sulfur that are accessed by the Thode extracts include insoluble sulfate minerals (such as barite) and minerals that include sulfate. Apatite can accommodate sulfate ions in its structure (Economos and Boehnke, 2014) and has been described to reflect values at time of crystallization (Economos et al., 2017). A distinct possibility exists that these extracts include sulfate from apatite that is known to be present (Appendix A; Table A.4).

Another source of sulfur that we might have missed in the petrographic study due to the limited amount of samples is insoluble sulfate minerals such as barite. However, there is no previous description in the literature (Wilson, 2015; Wilson et al., 2017) of insoluble sulfates in the Bushveld samples, nor it was observed in this study. If insoluble sulfate minerals were indeed present, the $\Delta_{\text{Thode extract-sulfide}}$ might represent evidence for its origin as assimilated from the host rock, in which case it would not have reached chemical equilibrium with the sulfide after assimilation.

I want to clearly make the point that the analyses reported as "Thode extracts" do not represent the sulfate values of the rock and should not be considered as such (Figure 3.10), but that the Thode extract sulfur still provides valuable information that allows for the identification of samples with sulfate and other nonsulfide sources of sulfur. If the need arises to measure sulfur isotopes in samples that are poorly characterized in terms of mineralogy, the sulfur extraction protocols should contain a soluble sulfate extraction prior to the total sulfide extraction, and a sequential extraction for possible insoluble sulfate after the total sulfide extraction.

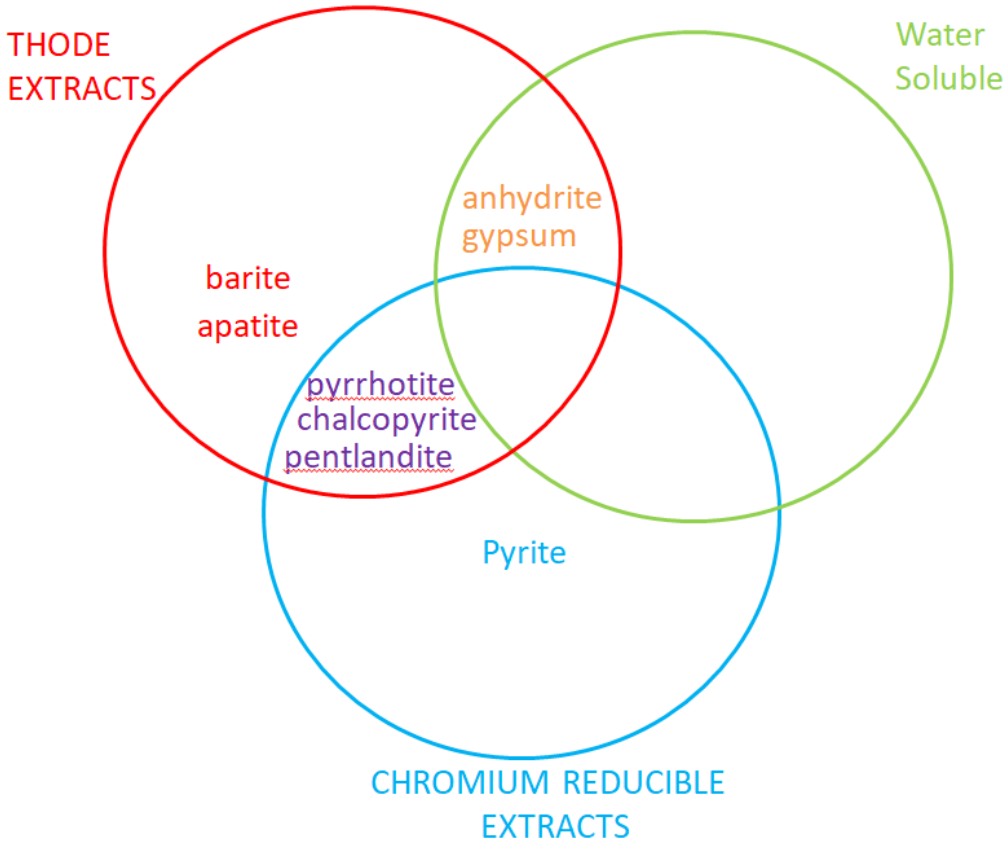

Figure 3.10. Venn diagram exemplifying the overlap between phases containing different sulfur species (sulfide, sulfate) and what is extracted by each method. Note that the Thode extracts intersect both fields for water-soluble sulfate and chromium reducible sulfur, with the potential to extract almost all the phases in a sample.

An additional complication for the whole-rock Thode extract measurements obtained in this study comes from the rocks from the Marginal Zone and one sample from the Lower Zone. As noted above, a few samples yield total sulfide and Thode extracts with $\Delta^{33}S$ values that are resolvable outside of uncertainty, and two have very dissimilar $\delta^{34}S$. The $\delta^{34}S$ of these two

Table 3.8. Values calculated for the $\Delta_{\text{Thode extract-sulfide}}$ in each sample.

Corrected Depth (m)	$\delta^{34}S_{sulfate}$	$\delta^{34}S_{sulfide}$	$\Delta_{\text{Thode extract-sulfide}}$
489.83	0.920	0.662	0.258
612.7	-2.411	2.317	-4.728
686.23	3.670	1.568	2.102
686.56	3.159	1.614	1.544
869.81	0.786	-10.799	11.585
871.77	1.716	1.244	0.472
880	2.292	2.106	0.186
899.59	2.307	2.566	-0.259
979.15	-22.799	1.220	-24.019
999.77	1.341	1.478	-0.137
1051.15	1.392	1.756	-0.364
1080	2.636	1.661	0.976
1321.84	1.789	1.081	0.708
1331.06	2.213	4.368	-2.155
1430.51	2.913	1.944	0.969
1481.01	1.511	0.019	1.491
1522.36	3.011	1.489	1.522
1558.24	6.444	6.257	0.188
1599.68	1.321	0.075	1.246
1648.02	6.486	6.398	0.088
1653.63	5.768	6.282	-0.514
1734.85	3.895	2.036	1.859
1820	7.680	4.342	3.338
1926.4	7.567	7.743	-0.175
1958.46	3.169	-0.364	3.532

samples are sufficiently different to preclude high temperature equilibrium and thus may reflect a sulfur contaminant (not necessarily in the sulfate form) in these samples with different isotopic characteristics. The same can be inferred from the difference in $\Delta^{33}S$. The origin of such a

contaminant is unclear, although, for samples from the Marginal Zone, addition of sulfur from sedimentary rocks can explain these differences.

From here forward, I will discuss only the results of the total sulfide data, except for the samples containing anhydrite.

3.6.2. Sulfur isotope composition of the Lower Bushveld Series and its geological significance

The values of sulfur isotope composition in sulfides of the Lower Bushveld Series are similar to the Main Bushveld Series, and show that the entire Rustenburg Layered Suite, from its basal unit, to its top, is contaminated with surface-derived sulfur. The average $\Delta^{33}S$ of the BUS (0.057‰) is the lowest among all units of the RLS, while the Marginal Zone encompasses rocks with the highest values found in this intrusion ($\Delta^{33}S$ up to 0.322‰). Comparison of the sulfide profile with the $^{87}Sr/^{86}Sr_{(i)}$ profile data obtained by Wilson et al. (2017) shows coincident changes in intervals with different $\Delta^{33}S$ characteristics and intervals with different $^{87}Sr/^{86}Sr_{(i)}$ in the Lower and Marginal Zones (Figure 3.12). This behavior is consistent with the pattern reported by Magalhães et al. (2018) (Chapter 2), which showed different contaminants in the RLS. The same pattern can be observed in the BUS, but the range of $\Delta^{33}S$ variations are very subtle compared to the large variations of $^{87}Sr/^{86}Sr_{(i)}$.

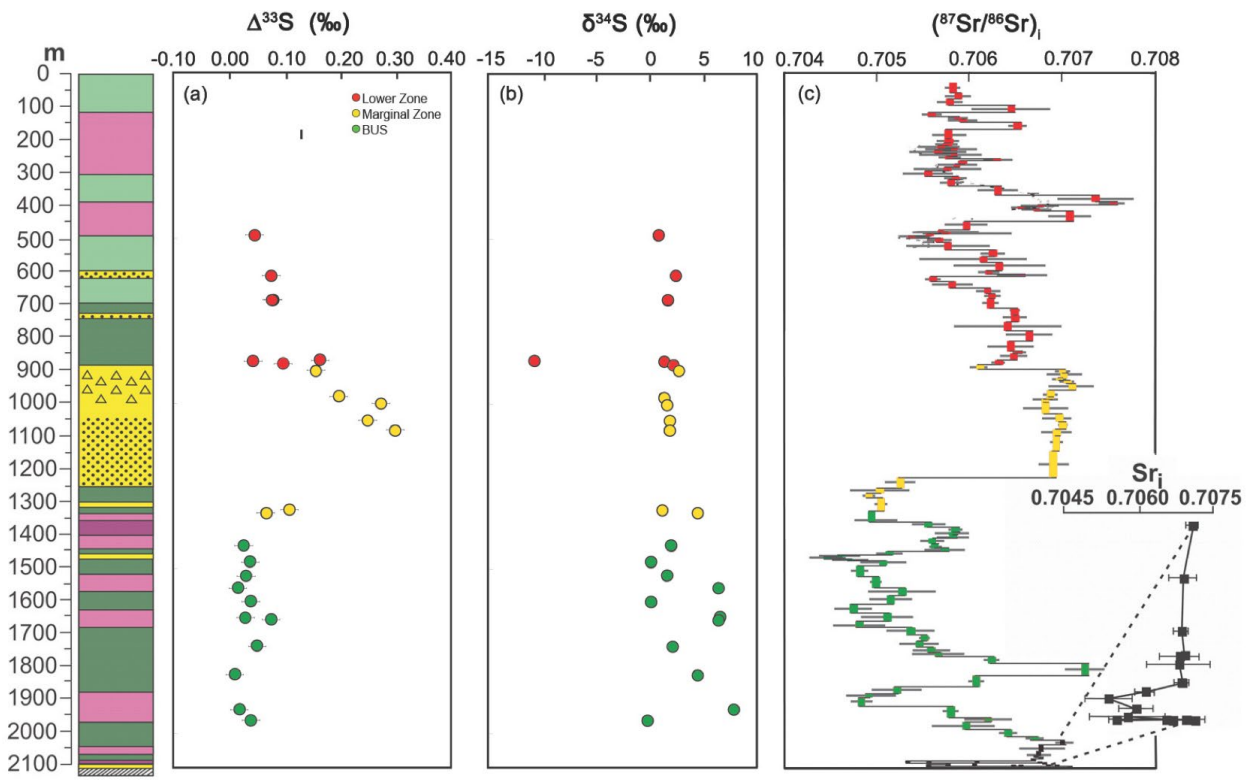

Figure 3.12. Variation of $\Delta^{33}S$, $\delta^{34}S$ and $^{87}Sr/^{86}Sr_{(i)}$ with depth in the Clapham Section. The $^{87}Sr/^{86}Sr_{(i)}$ data are in-situ measurements in plagioclase from Wilson et al. (2017).

Four sources have been postulated to explain the observed mineral compositions, trace element patterns, and Sr isotopic composition of the Clapham section (Wilson et al., 2017). These include primitive mantle source, subcontinental lithospheric mantle, lower crust of the Kaapvaal Craton, and the metapelites of the Pretoria Group of the Transvaal Supergroup, which are in contact with the BUS. Wilson et al. (2017) also inferred, based on incompatible trace elements and the Sr isotopic compositions, that the base of the Lower Zone and the base of the BUS are more influenced by crustal contamination than the rest of the RLS. This is reflected in the sulfur isotope composition (sample with very negative $\delta^{34}S$ in the Lower Zone, overall higher $\delta^{34}S$ in the bottom part of the BUS), but there is no significant change in the $\Delta^{33}S$ values.

The Lower Zone data match the sulfur isotope values previously reported by Magalhães et al. (2018) for the same unit (recalculated values of $\delta^{34}S$ of 2.24‰ and $\Delta^{33}S$ of 0.088‰). A single Marginal Zone analysis previously had yielded a slightly higher than average value (recalculated $\delta^{34}S$ and $\Delta^{33}S$ measured as 3.17‰ and 0.081‰, respectively), and could either be explained by where within the Marginal Zone it is being sampled, or that the composition of this unit is dependent on the local sedimentary rocks, such as what is seen at the Northern Limb (Penniston-Dorland et al., 2008; Sharman et al., 2013). No significant mineralogical change has been observed with these rocks, and their lowest Mg# can be attributed to the differentiation from the BUS, as proposed by Wilson (2015), instead of being Lower Zone magmas that interacted with the floor of the intrusion.

The increase of $\Delta^{33}S$ values in Marginal Zone in the Clapham section is interpreted to represent crustal contamination of the residual melt following settling of the cumulates that formed the BUS. This is also supported by the coincidence of the highest $\Delta^{33}S$ values corresponding to layers where pelitic xenoliths have been reported in hand sample and in the field (Wilson, 2015) and suggests that a shedding of material from the then roof of the intrusion occurred after significant crystal settling. Although none of the Marginal Zone samples analyzed here contained xenoliths, these pelites from the Pretoria Group are well described in the literature (Wilson, 2015).

The chilled margin of the RLS is in contact with the Magaliesberg Quartzite (Wilson, 2012), estimated to be ~2.1 Ga (Lenhardt et al., 2012). Considering that the Marginal Zone has xenoliths of rocks that are stratigraphically higher than the Magaliesberg Quartzite, it is not expected that these sediments would have any significant mass-independently fractionated sulfur. Additionally, measurements conducted for this study in rocks from the Pretoria Group

(Magaliesberg Quartzite, Lakenvalei Quartzite, and Vermont Pelite; both metamorphosed and pristine samples) have not yielded any sulfur (i.e. sediments are very sulfur-poor and therefore would not contribute with sulfur in case of assimilation). Other units (Houtebeck Fm., Silverton Fm.) measured by Guo et al. (2009) have yielded $\Delta^{33}S$ that are close to zero. Therefore, despite clear evidence for assimilation of crustal material and an apparent correlation between pelite xenolith appearance and higher $\Delta^{33}S$ values in the rocks, there is a discrepancy between the measured sulfur isotope composition in these sediments and what is observed in the Marginal Zone.

Despite being a more primitive magma, the BUS shows a sulfur isotope signature that is different than what is expected for an uncontaminated mantle melt ($\Delta^{33}S=0\pm0.008$; Labidi et al., 2014). This assessment is valid regardless of the high Mg# in olivine and orthopyroxene that reflects rocks crystallized from a primary ultramafic magma, or the overall mineralogy of the samples. The relatively constant $\Delta^{33}S$ of the BUS suggests that the magmas had a near-homogeneous sulfur isotopic composition during the main phase of crystal settling, without significant addition from sulfur from the country rocks. The absence of BUS sulfur with $\Delta^{33}S = 0$ also continues to support the hypothesis that the intruded melts carried a mass independent signature at the time of injection. Evidence from the $^{87}Sr/^{86}Sr_{(i)}$ values has led Wilson et al. (2017) to infer that the BUS magmas assimilated TTGs from the lower crust.

Most occurrences of primary anhydrite are linked to arc magmatism, and usually occur in rocks with an intermediate to felsic composition that contains hydrous minerals such as amphibole (Luhr et al., 1998). The fO_2 values for anhydrite stability in a magma were determined to be around ΔFMQ +1.5 to ΔFMQ +2 (Carroll and Rutherford, 1987; Jugo et al., 2005), which would place the magmas at a higher fO_2 than previously described for the RLS

(oxygen fugacity condition at FMQ or more reduced; Naldrett et al., 2012). No hydrous phases are present in the BUS rocks that contain anhydrite, as biotite is a very minor component in those. Samples where biotite composes the main mineralogy of the rock (CH7 708.24) do not contain anhydrite. Quartz and K-feldspar are typical in these anhydrite-bearing rocks, which is contrasting to its inferred initial ultramafic composition (Wilson, 2012). The presence of these phases (i.e. quartz, K-feldspar, and anhydrite) might reflect a change in whole-rock chemistry due to contamination by crustal rocks. The samples with abundant anhydrite, measured as water-soluble sulfate, show a positive $\Delta_{sulfate\text{-}sulfide}$, between 2.3‰-4.0‰ (Figure 3.13), corresponding to sulfate-hydrogen sulfide equilibration temperatures between 1000 and 1400°C (Eldrigde et al., 2016). A sample with similar sulfide and soluble sulfate values (CH7 749.68) is interpreted as not representing the value of actual anhydrite. The $\Delta_{sulfate\text{-}sulfide}$ are much smaller than observed for Norils'k (8.5‰-11.9‰; Ripley et al., 2010), or the Northern Limb (~6.5‰; Yudovskaya et al., 2018), locations with field relationships clearly evidencing assimilation of an anhydrite-bearing host rock. Note however, that the fractionations between sulfate and sulfide for fractionations of this magnitude of Eldridge et al. (2016) are between ~500 and 700°C and indicate either that equilibrium was not attained at magmatic temperatures, or that these other sulfates equilibrated with sulfide at much lower temperature. The BUS does not preserve either field or petrographic evidence for assimilation of sulfate. The floor rock does not have anhydrite or any sulfur and sulfate is seen included in pyroxene and with textures that imply an igneous origin. The similar $\Delta^{33}S$ (within uncertainty) of sulfate and sulfide also support this suggestion.

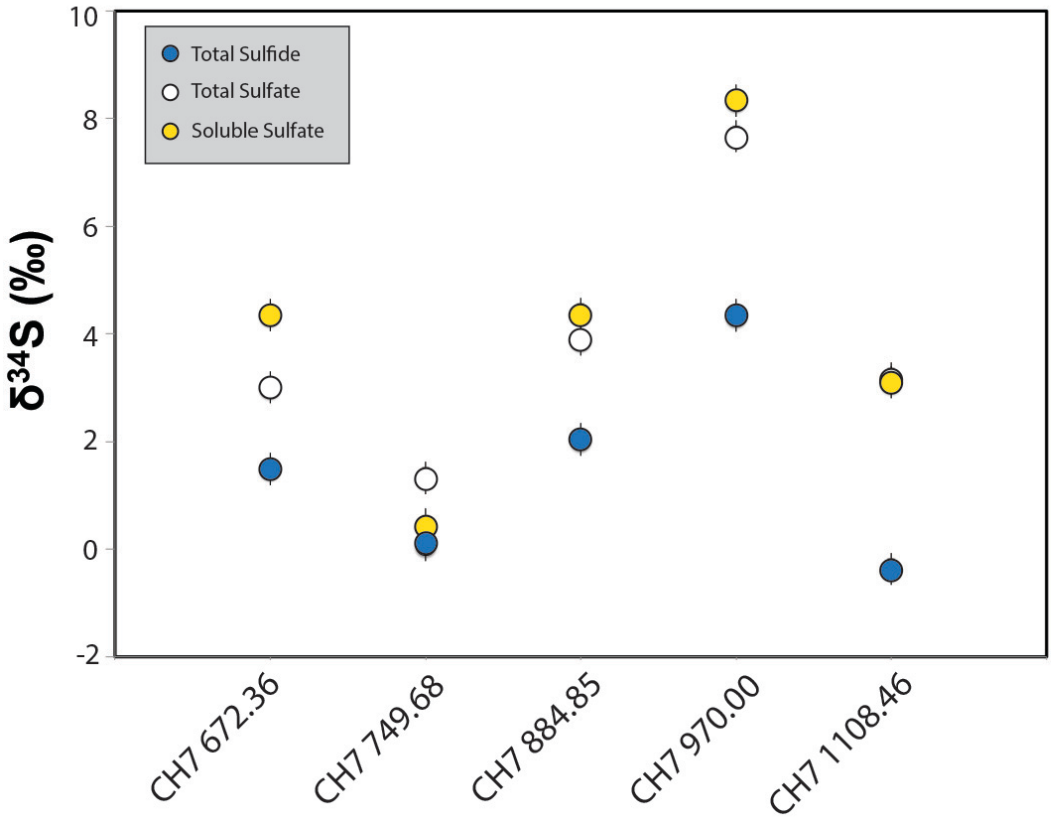

Figure 3.13. Comparison of the $\delta^{34}S$ values for total sulfide, Thode extracts, and water-soluble sulfate.

An other constraint on the temperatures is given by experiments conducted by Miyoshi et al. (1984) using chloride melts, which are the only available experimental sulfide-sulfate fractionation determined for high temperature systems. They have obtained $\Delta_{sulfate\text{-}sulfide}$ from 3.7‰ to 5.1‰ for fractionation at temperatures between 900-1100°C, similar to the values obtained for the BUS. These fractionation values, in conjunction with the petrography (Figures 3.7a through 3.7f), suggest crystallization of magmatic anhydrite and sulfate-sulfide fractionation at higher temperatures. Although previously described as a late-magmatic phase (Wilson et al., 2017), anhydrite was found here to be an early magmatic mineral in the BUS. Anhydrite was found included in pyroxenes, and the precipitation of pyrite and apatite grains surrounding the

anhydrite shows interaction with a liquid that was becoming more reduced during crystallization. If sulfate was a direct result of assimilation from a country rock, rather than crystallization from the magma, either both sources of sulfur (sulfide in magma, sulfate in contaminant) would need to have exactly the same $\Delta^{33}S$, or be well-mixed in the magma in order for both sulfide and sulfate to have similar $\Delta^{33}S$ composition. These findings do not preclude the assimilation of other sulfate-bearing material, but it does strongly suggest that such assimilation did not happen post emplacement. The appearance of quartz and K-feldspar suggests that either a crustal material was added into the magma, or the initial composition of some of the BUS magmas reflect an unusual composition, likely with contributions from more than one source.

3.7. Conclusions: Implications for sulfur source and processes occurring during emplacement of the RLS

The multiple sulfur isotope compositions of the Clapham core provides insight into the processes taking place in the early stages of emplacement of the Rustenburg Layered Suite. The Basal Ultramafic Sequence, the lowermost unit of the RLS, has olivine, pyroxene, and plagioclase with chemical composition that reflect crystallization from a primitive ultramafic magma. It also has the presence of anhydrite, a sulfate, which is puzzling given the inferred initial reduced nature of the RLS magma (Naldrett et al., 2012). Although considered the most primitive unit, the BUS has a sulfur isotope signature unlike what is expected of an uncontaminated mantle source, demonstrating that the earliest magmas were also contaminated. The composition of sulfide and sulfates suggest equilibrium at high temperatures, and, coupled with textural evidence, suggest a magmatic origin for the anhydrite.

The Marginal Zone, as it occurs in the Clapham Section, was interpreted by Wilson (2015) to represent the result of interaction between the roof of the intrusion and residual melts from fractional crystallization of the BUS. This unit has the highest $\Delta^{33}S$ observed in the Clapham core; this spike in $\Delta^{33}S$ can be associated with field evidence for contamination from rocks from the Pretoria Group. However, the pelites of the Pretoria Group do not have an adequate composition to contribute significant anomalous sulfur to this intrusion.

Following the crystallization of the BUS and Marginal Zone, a new magma batch then intruded the proto-RLS chamber and formed the Lower Zone. Wilson et al. (2017) inferred that this unit has a contribution from the sub-continental lithospheric mantle. The lack of any samples with $\Delta^{33}S$ having values of zero further suggests that the injected melts already carried an anomalous signature, which could potentially imply that the source of magmas was impacted by recycling of ancient material. Anhydrite has been reported in some of the Lower Zone rocks (Wilson et al., 2017), but was not observed in any of the analyzed samples.

The size of the BMP and the widespread appearance of a very homogeneous signature within a large area raises the possibility that the $\Delta^{33}S$ is an intrinsic property of the magma source. Possible sources of these signals are the upper crust (see discussion in Chapter 4), lower crust, and the mantle. The values of S isotopes in the lower crust of the Kaapvaal Craton are not well-constrained, although evidence that its composition cannot fully explain the values observed in the RLS exists (Vredefort Dome, Chapter 2). Chapter 5 will explore the possibility of whether the sub-continental lithospheric mantle (SCLM) has contributed with anomalous sulfur to the Bushveld Magmatic Event, given the evidence for participation of the SCLM in the Bushveld event (James et al., 2001; Richardson and Shirey, 2008; Wilson et al., 2017) and the findings of peridotite xenoliths with a positive $\Delta^{33}S$ signature (see Chapter 5). Modern mantle plumes can

contain a non-zero, negative $\Delta^{33}S$ signature (Cabral et al., 2013; Delavault et al., 2016), albeit the $\Delta^{33}S$ is smaller than what is observed in the RLS, and also not positive.

Chapter 4. Multiple sulfur isotope composition of the Waterberg Project shows that upper crustal assimilation did not play a major role in magma contamination

4.1. Abstract

The source of the crustal-derived sulfur ($\Delta^{33}S \neq 0$) is one of the major questions related to the origin of the platinum group element mineralization in the Rustenburg Layered Suite (RLS). The 2.06 Ga Waterberg Project (WP) is a mafic-ultramafic intrusion related to the Bushveld Magmatic Province that, like the RLS, has significant PGE-rich horizons. While the RLS is hosted in the Transvaal Supergroup in the Kaapvaal Craton, the Waterberg is hosted in the Waterberg Supergroup in the southern margin of the Limpopo Belt. Although they are linked to the same magmatic event, they are separate intrusions that intruded different upper crust material.

The Waterberg Project has a signature of anomalous sulfur ($\Delta^{33}S$ = 0.113‰±0.016‰, 1.s.d.), similar to the RLS ($\Delta^{33}S$ = 0.133‰±0.030‰). There is no evidence for influence of the host rock as a source of anomalous sulfur. The lack of significant variation in the $\Delta^{33}S$ values within the Waterberg stratigraphy shows that the addition of upper crust sulfur is not necessary for PGE formation. We suggest that the contamination of the Waterberg and RLS magmas with a surface-derived material of Archean age occurred at depth, either in the lower crust or in the sub-continental lithospheric mantle.

4.2. Introduction

The Waterberg Project (WP), also referred to as the "Far Northern Limb" (Huthmann et al., 2016; 2017; 2018; Kinnaird et al., 2017; Figure 1), is a newly discovered platinum group element (PGE) prospect. It is located in the southern margin of the 2.6 Ga Limpopo Belt in South Africa (Kreissig et al., 2001), north of the Northern Limb of the Rustenburg Layered Suite (RLS) (Figure 1), which contains the largest PGE deposit on Earth. The WP is coeval with the RLS, and therefore can be associated with the Bushveld Magmatic Province, but differences in geochemistry and mineralization style suggest the two intrusions are not connected (Kinnaird et al., 2017; Huthmann et al., 2018). These relationships make the WP the ideal location to investigate both the source of sulfur and the relationship between sulfur and the enrichment of PGEs in the intrusions.

The RLS preserves evidence for a surface-derived sulfur-bearing component of Archean age ($\Delta^{33}S \neq 0$; Penniston-Dorland et al., 2008; 2012; Magalhães et al., 2018), as magmas originating from mantle with only primitive sulfur will yield near zero $\Delta^{33}S$ (Labidi et al. 2012; Peters et al., 2010). Such signatures were first described in the Northern Limb of the RLS by Penniston-Dorland et al. (2008), and subsequently reported for both Eastern and Western Limbs (Penniston-Dorland et al., 2012). Magalhães et al. (2018) documented the presence of an anomalous sulfur signature throughout the entire stratigraphy of the intrusion. No significant variation of sulfur isotopic composition has been observed associated with the PGE-rich layers, despite several models of PGE enrichment requiring interaction of the silicate magma with sulfide immiscible liquids (Campbell et al., 1983; Kerr and Leitch, 2005). While the presence of anomalous sulfur in the RLS is well described (Penniston-Dorland et al., 2008; 2012; Sharman et al., 2013; Magalhães et al., 2018), its origin remains unresolved. Mass-independent fractionation

($\Delta^{33}S$) is a fingerprint of Archean surface material (Farquhar et al., 2000) due to its atmospheric origin (Farquhar et al., 2003), and such a signature is recorded in the supra-crustal sediments of the Transvaal Supergroup. However, rocks from the lower crust, or the sub-continental lithospheric mantle are also possible source regions for the surface-derived sulfur.

The study of an intrusion that resulted from the same magmatic event as the RLS but that occurs as an entirely separate body in a different geological and tectonic setting, like the WP, provides a unique opportunity to understand how surface-derived sulfur was introduced into the magmas of this igneous province. Here, we present multiple sulfur isotope compositions of the WP and assess the possible source regions of anomalous sulfur, the timing of contamination, its role in the PGE mineralization, and its implications for the evolution of the WP and the RLS.

4.3. The Waterberg Project

The WP is located north of the Hout River Shear Zone, which marks the boundary between the Kaapvaal Craton, where the RLS is located, and the southern margin of the Limpopo Belt (Smit et al., 1992, Kreissig et al., 2001). Evidence for the association of Waterberg to the Bushveld magmatic event comes from the U/Pb zircon ages, which yielded values of 2.059±3 Ga and 2.053±5Ga (Huthmann et al., 2016). The ages overlap with the 2.0589±0.0008 Ga (U-Pb in titanite, Buick et al., 2001) ages of the Bushveld Complex, and 2052±16 Ma age of the Molopo Farms Complex (U-Pb in baddeleyite, De Kock et al. 2016), another intrusion of the Bushveld Magmatic Province.

The WP reaches thicknesses of up to 1200 meters, dips 34°-38° to the west and is directly overlain by sediments of the Waterberg Supergroup (Kinnaird et al., 2017). The stratigraphy of

the intrusion consists of, from bottom to top: Ultramafic Sequence (UmS), overlain by a Troctolite-Gabbronorite-Anorthosite sequence (TGA), and an Upper Zone (UZ) of magnetite-bearing gabbroic rocks to ferrogabbros. The PGE mineralization occurs in two different levels: the F zone, which occurs within the UmS, and the T zone, which is located at the top of the TGA. The footwall consists of Archean gneisses that are interfingered with pyroxenite near the contact. The first pyroxenitic magmas caused the basement to melt, and mingling of pyroxenitic and granitic magma occurred, leading to formation of granofels (Huthmann et al., 2018). The layers were thought to form in two distinct magma pulses, and to have been homogenized in a staging chamber in the lower crust (Huthmann et al., 2017) given the homogeneity of $^{87}Sr/^{86}Sr_{(i)}$ (values between 0.7065-0.7075) throughout the stratigraphy. Further details and comparison with the Northern Limb geology can be found in Huthmann et al. (2016), Kinnaird et al. (2017), Huthmann et al., (2017), Huthman et al. (2018), and McCreesh et al. (2018a).

Differences in lithology, geochemistry, and mineralization style when compared to the RLS suggest that this body was emplaced separately from the Northern Limb, in a single magmatic basin (Huthmann et al., 2018).. In the RLS, the PGE-rich horizons occur in the Critical Zone, with the PGE concentrated in sulfides and in chromite (Cawthorn, 2010). In the WP, the PGE-mineralized T-layer is hosted in the TGA sequence, which is comparable to the Main Zone of the RLS, and the PGE enrichment is associated to arsenides and bismuthotellurides, instead of PGE-rich sulfides (McCreesh et al., 2018).

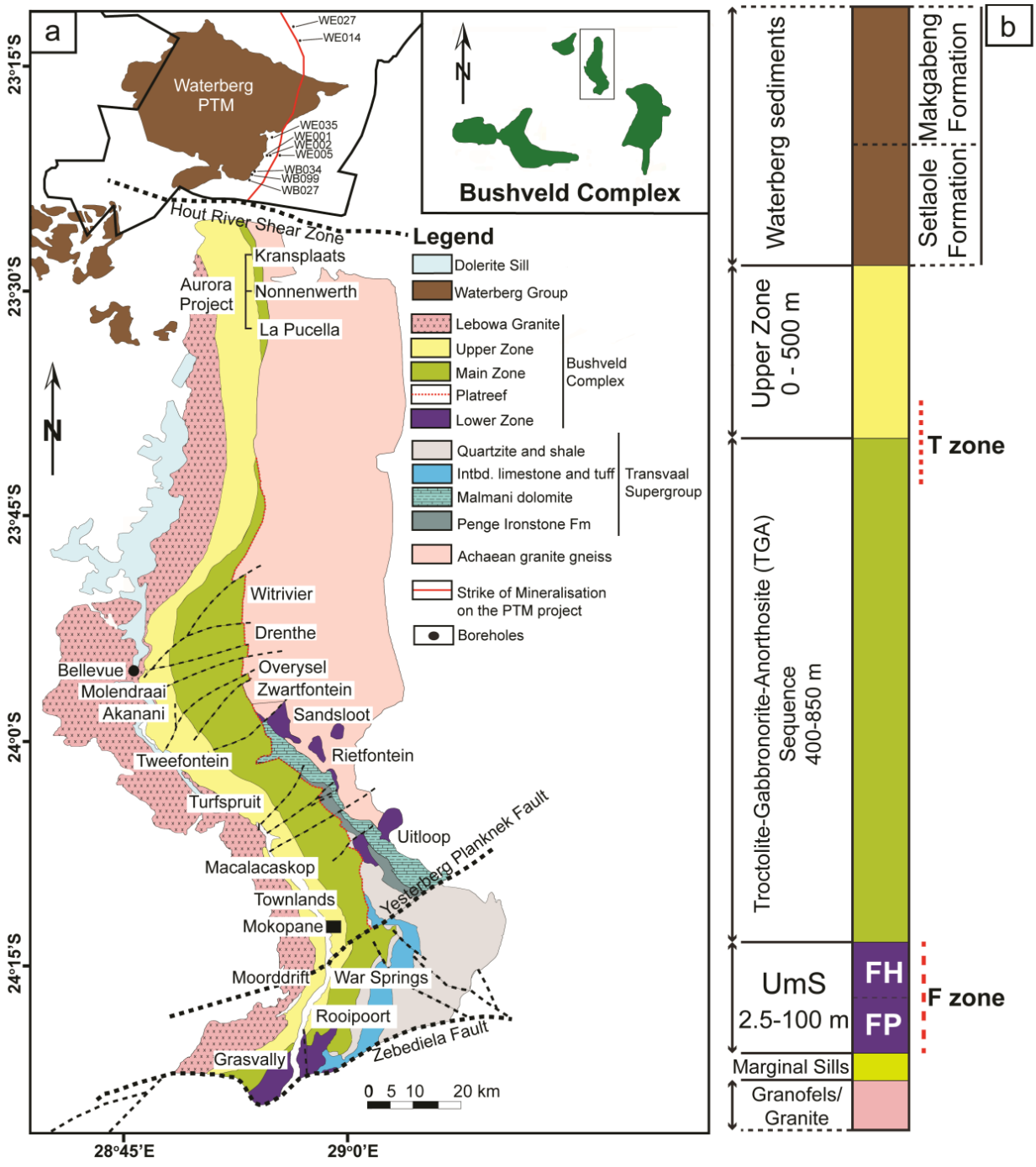

Figure 4.1. Geological map of the Northern Limb of the Rustenburg Layered Suite, evidencing the location of the Waterberg Project (does not crop out). The stratigraphic column of the WP is described on the right, with emphasis on the mineralized zones F and T. Figure from Matthew McCreesh.

4.4. Methods

The multiple sulfur isotope composition of sulfides from the WP was measured by using a combined acid-volatile sulfur method to extract all inorganic sulfides. This procedure is the same as described in Chapter 2, and therefore will not be repeated here.

The multiple sulfur isotope data are reported using the delta ($\delta^{3X}S = \left[\frac{\left(\frac{^{3X}S}{^{32}S}\right)_{sample}}{\left(\frac{^{3X}S}{^{32}S}\right)_{V-CDT}} - 1\right]$) and capital delta notation ($\Delta^{33}S = \delta^{33}S - [(1+\delta^{34}S)^{0.515} - 1]$). Uncertainties are estimated on long-term standard reproducibility of fluorinations of IAEA-S1 and yield 2σ variations of $\delta^{33}S$±0.15‰; $\delta^{34}S$±0.30‰; and $\Delta^{33}S$±0.016‰. Data for samples are normalized directly to recent high quality analyses of CDT (Antonelli et al., 2014) which yields an isotopic composition of IAEA S-1 of $\delta^{34}S$ = -0.394‰; and $\Delta^{33}S$ = 0.116‰ relative to Canyon Diablo Troilite (CDT). We recognize that this determination does not match the accepted $\delta^{34}S$ of IAEA S1 on the V-CDT scale, but use this normalization here because it allows a more direct comparision with measurements of $\Delta^{33}S$ made in our laboratory for both CDT and MORB, and also allows direct comparisons with the data of Labidi et al. (2012) for $\Delta^{33}S$ of MORB, both of which indicate no resolvable difference for the $\Delta^{33}S$ of MORB and CDT. We take the $\Delta^{33}S$ of MORB to be representative of mantle without significant added sulfur from recycling. Our data can be converted to V-CDT by renormalization so that IAEA S1 has a $\delta^{34}S$ value of -0.3‰, but the conclusions of this study will not change.

4.5. Results

The $\delta^{34}S$ values are within the range of -0.65‰ to +1.89‰, with the exception of one sample that yields a higher value of +5.26‰ (Figure 4.2, Table 4.1). The average is 0.84‰, with a median value of 0.47‰ and interquartile range of 0.44‰. The $\Delta^{33}S$ values are within the range of 0.079‰ to 0.135‰, with a mean of 0.113‰ and interquartile range of 0.023‰. These values compare to the corrected average values for the RLS of 1.82‰ and 0.133‰, respectively. The one measured host rock sample, a sulfur-rich granofels, has a composition of $\delta^{34}S$ of 1.89‰ and $\Delta^{33}S$ of 0.034‰.

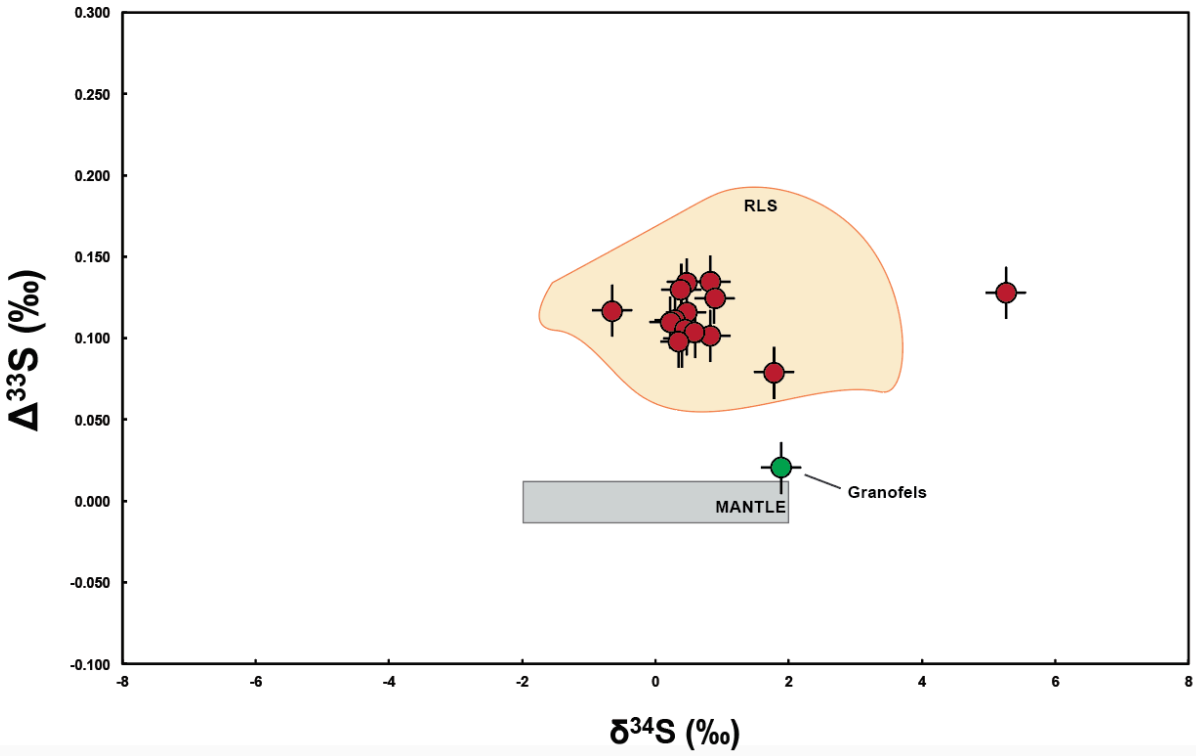

Figure 4.2. Multiple sulfur isotope composition of the Waterberg Project (red circles), and its host rock, a sulfur-rich granofels (green circle). The orange field denotes the range of compositions for the RLS (Penniston-Dorland et al., 2012; Magalhães et al., 2018), while the gray rectangle represents the composition of sulfur from mantle-derived MORB glass (Labidi et al., 2012; 2013; 2014; Labidi and Cartigny, 2015). Error bars are 2σ.

Table 4.1. Multiple sulfur isotope data of the Waterberg Project.

Sample	$\delta^{33}S$	$\delta^{34}S$	$\delta^{36}S$	$\Delta^{33}S$	$\Delta^{36}S$	Unit
WB017 206.29	0.377	0.472	0.811	0.134	-0.085	Upper Zone
WB017 294.00	0.580	0.883	1.621	0.125	-0.058	Upper Zone
WB027 537.64	0.329	0.387	0.792	0.130	0.057	Upper Zone
WB099 698.67	0.256	0.282	0.425	0.111	-0.110	Below Main-Upper Zone boundary
WB099 699.40	0.223	0.218	0.355	0.110	-0.059	Below Main-Upper Zone boundary
WB099 700.02	0.347	0.470	0.831	0.105	-0.062	Below Main-Upper Zone boundary
WB099 705.50	0.525	0.821	1.550	0.102	-0.010	Below Main-Upper Zone boundary
WB099 763.00	0.363	0.482	0.882	0.115	-0.034	Main Zone
WB099 825.73	-0.216	-0.647	-0.978	0.117	0.251	Main Zone
WB099 900.03	2.835	5.263	9.944	0.128	-0.079	Main Zone
WB099 1009.00	0.407	0.588	1.138	0.104	0.020	Main Zone
WE035 603.70	0.305	0.400	0.898	0.099	0.137	Ultramafic Platreef
WE035 616.68	0.998	1.784	3.434	0.079	0.041	Ultramafic Platreef
WB027 1116.10	0.288	0.370	0.627	0.098	-0.075	Ultramafic Platreef
WB029 1152.20	0.557	0.821	1.632	0.135	0.072	Ultramafic Platreef
WB027 1174.70	1.008	1.892	3.454	0.034	-0.144	Footwall

4.6. Discussion

The evidence collected so far (Kinnaird et al., 2017; Huthmann et al.; 2016; 2017; 2018) suggest that the WP is a completely different intrusion that did not interact with the magmas that formed the Northern Limb of the RLS, but is still associated to the Bushveld Magmatic Event. Huthmann et al. (2017) postulated that the magmas never coexisted in the same staging chamber given the different Sr isotope composition of the WP and the Northern Limb. Moreover, there is no clear evidence for lateral movement of magma in the upper crust at this location, as opposed to what is observed at the Uitkomst Complex, an ultramafic-mafic intrusion that is spatially associated to the RLS (Gauert et al, 1995; de Waal et al., 2001). There is no evidence so far for a physical connection between the WP and the Northern Limb, either on surface or subsurface. Similarities exist, however, in the sulfur isotopic compositions.

The mean $\delta^{34}S$ value of 0.84‰ for the WP, like that of the RLS (1.82‰), is slightly ^{34}S-enriched relative to the value inferred by Labidi et al. (2013) and Labidi and Cartigny (2015) for the depleted mantle (-1.40±0.50‰). This enrichment could reflect fractionations occurring during the extraction of sulfur from a mantle source during melting, as the average $\delta^{34}S$ that is within the range of mantle-derived magma composition (Sakai et al., 1983; Peters et al., 2010; Labidi et al., 2012). An alternative explanation, that includes the one sample that yields a higher value of +5.26‰, suggests a process that either added outside material (i.e. assimilation of host rock) or fractionated sulfur by a loss process. While the ^{34}S enrichment, alone, cannot be used to differentiate between these two, the $\Delta^{33}S$ of the WP samples in combination allows for an additional insight into the processes taking place in these intrusions.

The $\Delta^{33}S$ signature of 0.113‰ indicates that the Waterberg magma requires an assimilated surface-derived material of Archean age, and its relative homogeneity for samples

across the full range of $\delta^{34}S$ implies mass-dependent fractionation of sulfur without addition of sulfur with $\Delta^{33}S \neq 0.113‰$. This inference includes the sample at the contact with the lower $\Delta^{33}S$ signature and higher S content (<1wt% S) granofels. Addition of material to primitive mantle compositions is further supported by prior measurements of Sr isotopes (Huthmann et al., 2017), which also exhibit a high degree of homogeneity. This compares with the relationship observed for the RLS, which shows a subtle shift in the relationship between Sr, Nd, and $\Delta^{33}S$ for its different magma pulses (Magalhães et al., 2018).

The lack of any variation of $\Delta^{33}S$ values in the stratigraphy (Figure 4.3) also suggests a decoupling between a crustal assimilant and the precipitation of PGE rich layers, a behavior that is also seen at the Rustenburg Layered Suite (Magalhães et al., 2018). The simplest explanation for the near constant $\Delta^{33}S$ argues against addition of significant amounts of upper crustal sulfur with $\Delta^{33}S \neq 0.113‰$ and therefore implies that assimilation upon emplacement is not a direct pre-requisite for the PGE mineralization to occur. A similar relationship is seen for mineralization in the RLS (Magalhães et al., 2018). Huthmann et al. (2018) describe a lack of correlation between S content and Pt and Pd contents, which supports this hypothesis.

The similar $\Delta^{33}S$ of sulfur in the WP and the RLS (0.113‰ compared to 0.133‰, respectively), combined with the inference that this signature is a property of the mafic melts themselves, rather than attributable to late sulfur addition, raises the issue of understanding the process by which these mafic magmas acquired a homogenous $\Delta^{33}S$ signature. The RLS is hosted by the Transvaal Supergroup, which is known to possess highly anomalous $\Delta^{33}S$, but the WP is hosted in a much younger sedimentary sequence, the 2.0 Ga Waterberg Supergroup; thus the similarity of $\Delta^{33}S$ for the WP and the RLS suggests the surface-derived sulfur signature was acquired by a process occurring at depth, rather than at the site of emplacement.

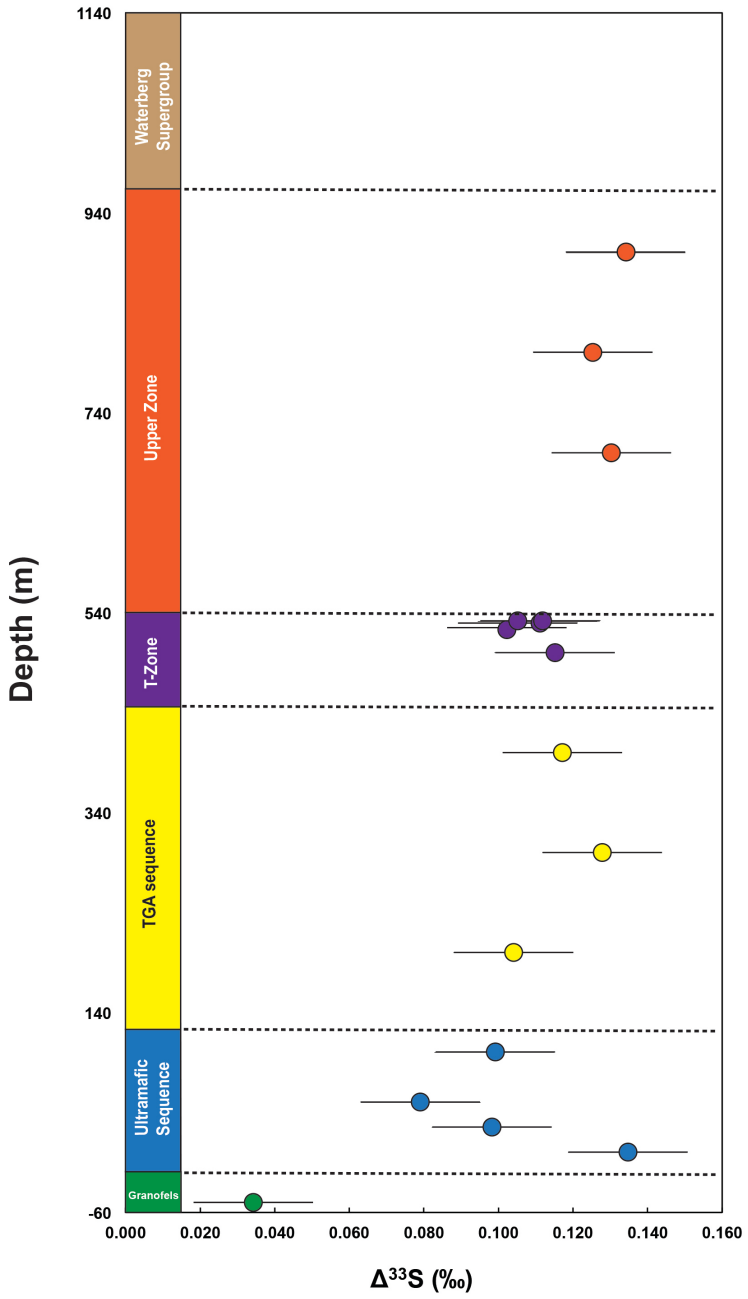

Figure 4.3. Variation of the sulfur isotope composition of the Waterberg Project in the context of stratigtaphic column (error bar is 0.016‰, 2σ).

One of the petrogenetic models for both the RLS and Waterberg Project include staging chambers in the lower crust, where the magmas would have resided prior to emplacement in the

crust and where they would have assimilated crustal material (McCandless et al., 1999; Huthmann et al., 2017). As the WP and RLS have similar compositions, it would be necessary that the country rocks have similar sulfur isotopic compositions, and that approximately the same amount of material was assimilated. Tests of this hypothesis were conducted previously (Maier et al., 2000; Harris et al., 2005; Magalhães et al., 2018) for different isotope systems, using analyses of exposed rocks from the Vredefort Dome as a proxy for the lower crust. The estimates of amount of contamination for different units of the RLS do not show a complete agreement; while the Sr, Nd, and oxygen composition of the Main Zone can be explained by 30%-40% assimilation of Vredefort granitoids, the composition of the Lower Zone cannot (Maier et al., 2000; Harris et al., 2005). Additionally, Magalhães et al. (2018) found that the Vredefort metagranitoids, metamafites, and metasediments have very low sulfur concentrations and a $\Delta^{33}S$ between 0.011‰-0.176‰, which cannot account for the RLS sulfur isotopic composition, but could account, qualitatively, for the WP. In order to evaluate if the Vredefort Dome rocks could have provided sulfur for the RLS, I performed simple mixing calculations using previously obtained sulfur and oxygen isotopic compositions for the Vredefort Dome and the RLS. The mantle value was set at $\delta^{18}O$ equal to 5.7‰ (Muehlenbachs and Clayton, 1976) and an oxygen concentration of 44%, and $\Delta^{33}S$ of 0‰ (Labidi et al., 2014) with a mantle abundance of 250 ppm (McDonough and Sun, 1995). I evaluated two rock types as potential end members, a granitoid and a metasediment. The highest $\Delta^{33}S$ of 0.176‰ was found in a metasediment with a sulfur concentration of 500 ppm. An approximation for the $\delta^{18}O$ of these rocks is 10‰ (among the highest values found in metasediments by Fagereng et al., 2008) and an oxygen percentage of 48%. A granitoid was also used as an end member, with $\Delta^{33}S$ of 0.101‰, 150 ppm concentration, $\delta^{18}O$ of 9.15‰ (Fagereng et al., 2008) and oxygen percentage of 48.62%. I find

that neither the metasediments nor the granitoids of the Vredefort Dome can generate the composition of RLS magmas through mixing with the mantle. There is no $\delta^{18}O$ data for the WP, therefore such calculations were performed only for the RLS.

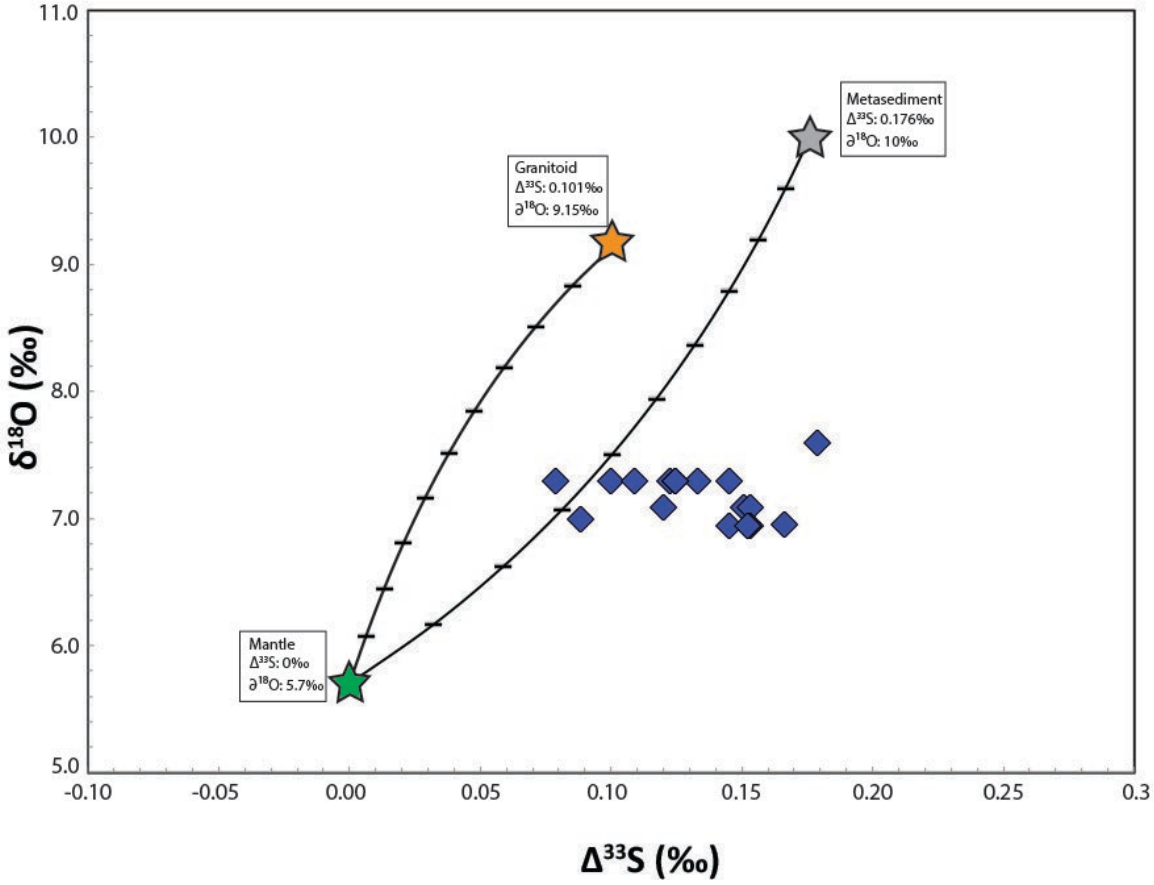

Figure 4.4. Mixing calculations of sulfur and oxygen isotope compositions between three distinct reservoirs: mantle, and granitoid and metasediments from the Vredefort Dome. Rustenburg Layered Suite data is plotted as blue diamonds. Mantle composition as obtained by Labidi et al. (2014) for sulfur, and Muehlenbachs and Clayton (1976) for oxygen. Oxygen data of the Vredefort Dome was estimated from Fagereng et al., 2008, and the RLS was extracted from Harris et al. (2005). The sulfur isotope data was obtained by Penniston-Dorland et al. (2012) and Magalhães et al. (2018).

Another possible source for the anomalous sulfur is the sub-continental lithospheric mantle (SCLM), as it was clearly modified in the Bushveld magmatic event. However, this would require a way to impart nonzero $\Delta^{33}S$ on the SCLM and a process that allowed for its homogenization before or during transport to the site of emplacement. Several studies have described evidence of recycling of Archean sulfur to various mantle reservoirs, such as in diamond-forming regions (Farquhar et al., 2002; Thomassot et al., 2009) and in regions associated with deeper mantle plumes (Cabral et al., 2013; Delavault et al., 2016). Studies of lavas from the Mangaia and Pitcairn plumes suggest that other asthenospheric mantle domains (HIMU and EMI) can carry anomalous $\Delta^{33}S$, albeit with a negative value (Cabral et al., 2013; Delavault et al., 2016), intrinsically different than what is found in the WP and RLS magmas. Eclogitic sulfide included in diamonds underlying the Kaapval Craton preserve evidence for a positive $\Delta^{33}S$ signature that has been interpreted as recycled Archean sedimentary material, suggesting the possibility for its addition to and preservation in the SCLM (Farquhar et al., 2002; Thomassot et al., 2009). Moreover, approaches using seismology (James et al., 2001; Shirey et al., 2002), Re-Os isotope systematics (Richardson and Shirey, 2008), peridotite chemistry (Viljoen et al., 2009), and diamond chemistry (Korolev et al., 2018) have also suggested contributions via interaction between the SCLM and the mantle plume that gave rise to the Bushveld Magmatic Province. If such SCLM carried anomalous sulfur such as seen in other parts of the craton, it could be a source for such a signature in Bushveld province magmas.

4.7. Conclusions

The WP is a newly described platinum-group element prospect in South Africa that has been geochronologically linked to the 2.06 Ga Bushveld Magmatic Province. It is thought to be a

separate intrusive body from the Northern Limb of the RLS due to different petrological, geochemical, and isotopic characteristics (Huthmann et al., 2016; Kinnaird et al., 2017). This layered intrusion has $\delta^{34}S$ values (0.84‰±1.32‰,) consistent with sourcing from a primitive mantle, but possesses an anomalous sulfur isotope signature ($\Delta^{33}S$ of 0.113‰±0.016‰) that requires an ancient (Archean) surface-derived sulfur component. The $\Delta^{33}S$ value is homogeneous in the different units and further suggests that assimilation of upper crust material did not instigate the PGE precipitation in the WP.

The homogeneity of Waterberg Prospect $\Delta^{33}S$ and its similarity to the $\Delta^{33}S$ of the Rustenburg Layered Suite, both emplaced in very different host rocks, implies a deep source for the nonzero $\Delta^{33}S$. These possible sources include the lower crust and a sub-continental lithospheric mantle source that contained a recycled, surface-derived component.

Chapter 5: Investigating the origin of anomalous sulfur in the Rustenburg Layered Suite, Bushveld Complex: the sub-continental lithospheric mantle as a potential source

5.1. Abstract

The sub-continental lithospheric mantle (SCLM) has been suggested as a source of an anomalous sulfur component for the Rustenburg Layered Suite and other primitive magmas of the Bushveld Magmatic Province. Previous studies have shown that sulfide inclusions in eclogitic diamonds from the Kaapvaal-Zimbabwe Craton contain mass-independent fractionated (MIF; $\Delta^{33}S$) sulfur ranging from -0.5‰ up to 1.3‰, which differs from the expected mantle value of $\Delta^{33}S=0$. However, peridotite-type sulfide inclusions do not contain anomalous sulfur, raising questions about whether the evidence from diamond forming regions are sufficient to support the suggestion of a primary nonzero $\Delta^{33}S$ signal.

This study reports whole rock multiple sulfur isotope analysis of sulfides in peridotite and eclogite xenoliths from the Premier Kimberlite, South Africa, that support an anomalous Archean sulfur isotope signature for SCLM, as well as the primitive BMP magmas. Most peridotite xenoliths in this study (n=16) yield variable $\delta^{34}S$ (-3.25‰ to +9.57‰), with near constant $\Delta^{33}S$ (avg. 0.062±0.034‰, 1 s.d.). One peridotite sample has a $\Delta^{33}S$ of 0.179‰, the highest among all samples analyzed in this study. The eclogite xenoliths (n=2) yield negative $\delta^{34}S$ ranging from -5.33‰ to -2.89‰, and average $\Delta^{33}S$ of 0.047±0.004‰ (1 s.d.), defining a compositional field that differs from the peridotites. The kimberlite matrix material has a similar $\Delta^{33}S$ signature to the peridotite xenoliths, with an average of 0.077±0.021‰ (1 s.d.), but different $\delta^{34}S$ values, with a much narrower range of -0.67‰ to +2.98‰.

These results demonstrate the presence of a surface-derived sulfur signature in the Premier Kimberlite and in the xenoliths it carries. The similarity of the signatures between peridotites and kimberlites, and their similarity to values seen in the Rustenburg Layered Suite, suggest that it is possible, from a qualitative perspective, that the SCLM is a potential source of the anomalous sulfur observed in the RLS. Since MIF is chemically conservative, the most efficient way to change it is by mixing of materials with different composition, which would allow for its conservation in the mantle for long periods of time. It also would allow its introduction in the system in the case of assimilation of crustal material with high $\Delta^{33}S$. There is no evidence, either petrographic or isotopic, for large-scale introduction of sulfur to the system during kimberlite emplacement.

5.2. Introduction

The occurrence of sulfides with a mass-independent sulfur isotope signature (S-MIF, $\Delta^{33}S \neq 0$) and without a significant $\delta^{34}S$ variability in the Rustenburg Layered Suite (RLS) and the Waterberg Project (WP) of the Bushveld Magmatic Province (BMP) raises the question on the source of sulfur in the intrusion. While evidence for local sulfur contribution from the wall rock exists (Penniston-Dorland et al., 2008), a more pervasive anomalous sulfur signature is observed in both intrusions, supporting the possibility that this signal was acquired prior to the transport of Bushveld magmas to their ultimate site(s) of emplacement (Magalhães et al., 2018). Such a signature has been shown (Chapter 4) to not originate by assimilation of the country rocks in the upper crust, as the RLS and WP share a similar sulfur isotopic signature despite being emplaced in different country rocks, and in the case of the WP, one without anomalous sulfur. Moreover, other lines of geochemical and geophysical evidence suggest that the sub-continental lithospheric

mantle (SCLM) participated in the Bushveld Magmatic Event (Carlson et al., 1999; James et al., 2001; Maier et al., 2005; Richardson and Shirey, 2008; Wilson et al., 2017), and could therefore have contributed sulfur to these magmas.

This chapter focuses on determining whether sulfur from the SCLM presents a nonzero $\Delta^{33}S$ signature, and if it could therefore be considered a potential source for the nonzero $\Delta^{33}S$ in the Bushveld magmas. Xenoliths from the Premier Kimberlite, a Proterozoic intrusion in Northeastern South Africa that is spatially associated with the Rustenburg Layered Suite, allow for insight into the composition of the SCLM underlying the RLS. The data presented here builds upon prior sulfur isotope evidence for recycling of Archean sulfur to the SCLM in the Kaapvaal-Zimbabwe Craton where diamonds form (Farquhar et al., 2002; Thomassot et al., 2009). This work extends the diamond work to the broader SCLM. This chapter presents the petrography and sulfur isotope composition of sulfides from the Premier Kimberlite matrix and entrained peridotite and eclogite xenoliths in order to evaluate whether there is evidence for recycling of ancient material in the sub-continental lithospheric mantle underneath this particular area of the Kaapvaal Craton, which could then have provided anomalous sulfur to the magmas that formed the BMP.

5.3. The Premier Kimberlite

The nomenclature of the Premier Kimberlite refers the name to a famous group of diamondiferous kimberlite pipes with a U-Pb perovskite age of ~1150 Ma (Wu et al., 2013) that crop out near Pretoria, South Africa. The $^{87}Sr/^{86}Sr_{(i)}$ values of 0.7025-0.7031 and $\varepsilon Nd_{(1150Ma)}$ between +0.8 and +1.9 are cited as evidence that the kimberlite derives from a moderately depleted mantle source (Wu et al., 2013). These kimberlite pipes intrude quartzites and

conglomerates from the Paleoproterozoic Waterberg Group, the Rustenburg Layered Suite, the felsic portion of the Rooiberg Group, and at depth also cut the dolomite, shale, and quartzite of the Transvaal Sequence (Maier et al., 2005). The kimberlite was cut by a gabbroic sill at 1100Ma (Allsopp et al., 1967), and the uppermost 300 m have been eroded and are no longer present.

The Premier Kimberlite is thought to be unrelated to the other kimberlites in South Africa which have younger ages (Smith et al., 1994; Griffin et al., 2014). These other kimberlites have brought peridotite xenoliths to the surface, and in some cases, diamonds. Studies conducted on sulfide inclusions in diamonds from some of these younger kimberlites, Orapa and Jwaneng, indicated the presence of Archean surface-derived sulfur within eclogites in the diamond forming regions of the SCLM underneath the Kaapvaal-Zimbabwe Craton (Farquhar et al., 2002; Thomassot et al., 2009). The Re-Os signature of eclogite-type sulfide inclusions from these and other kimberlite pipes such as the Venetia Kimberlite also provides evidence for recycling, given their very radiogenic initial isotope ratios (Shirey et al., 2002; Richardson and Shirey, 2008).

Intense carbonation of the Premier Kimberlite during ascent of the magma through the crust and metasomatism are a feature of this intrusion (Wu et al., 2013), which makes geochronological measurements challenging. Age constraints for this intrusion using radiogenic isotope systems have yielded variable ages, which are thought to reflect resetting due to either crustal contamination, alteration, or weathering (Wu et al., 2013). Tappe et al. (2018) recently obtained U/Pb perovskite ages for the volcanoclastic infill of the Premier pipe of 1153.3±5.3 Ma, and for a newly discovered kimberlite dike that yielded an 1139.8±4.8 Ma date which suggest that the volcanism at Premier may have extended over millions of years.

The Premier Kimberlite has sampled eclogites, and garnet and spinel peridotites from the SCLM underneath the Bushveld Complex. The peridotitic xenoliths can be divided in two

groups: coarse and deformed varieties, based on textural and mineral compositions (Danchin, 1979; Viljoen et al, 2009). The deformed peridotites are thought to have originated from greater depths than those with coarse textures, given their distinct pressure and temperature of equilibration (Gregoire et al., 2003; Viljoen et al. 2009). Deformed lherzolites were equilibrated at higher P-T conditions (1226-1371°C, 40 to 61 GPa; Gregoire et al., 2003), while the coarse variety were equilibrated at much lower P-T (927-1190°C, 29 to 44 GPa, Gregoire et al., 2003). This implies that the Premier Kimberlite has sampled material of different depths within the SCLM, with most of the xenoliths coming from the diamond stability field (Viljoen et al., 2009). Eclogite xenoliths from the Premier are interpreted to represent subducted material (Dludla et al., 2006; Richardson and Shirey, 2008). The average calculated equilibration temperatures of the eclogites is 1102 ± 37° C, assuming a pressure of 5 GPa (Dludla et al., 2006).

Previous Re-Os work carried out on the peridotite xenoliths from the Premier Kimberlite have shown that some peridotite xenoliths record a T_{RD} age consistent with the Bushveld magmatism (Carlson et al., 1999). Indirect evidence for refertilization also includes the Pt content in sulfides from these xenoliths (Maier et al., 2005), and proposed links to geochemistry of dunite pipes associated with the Bushveld Complex (Gunther et al., 2018). These discordant dunite pipes that occur in the Critical and Lower Zones are thought to be related to the RLS. Their high oxygen isotope values (5.7–7.0‰ in olivine and and 6.7–7.4‰ in pyroxene) are similar to those of the RLS zones they intrude in, but the olivine geochemistry provides no evidence for assimilation-fractional crystallization processes. The high Ni/Mn ratio of the olivine is interpreted to be inherited from the melting of a pyroxene-rich mantle source (Gunther et al., 2018).

5.4. The Sub-Continental Lithospheric Mantle underneath the Kaapvaal Craton

Several lines of evidence point towards connections linking the SCLM to the BMP. Low P-wave seismic velocity in the mantle underneath the Bushveld Complex at 150 km (James et al, 2001), trace element patterns indicative of contribution of an eclogitic component in the Lower Zone (Wilson et al., 2017), and Sr, Nd, and Os isotopic compositions suggesting a harzburgitic component in addition to the eclogitic component in the RLS magmas (Richardson and Shirey, 2008; Wilson, 2015; Wilson et al, 2017) have all been cited as evidence for involvement of the SCLM in the generation of the Bushveld magmas. A high-temperature, melt-related metasomatic event in the mantle is thought to be associated with the Bushveld magmatism as well (Viljoen et al., 2014), transporting elements such as Ca, Fe, Ti and Zr, and closely related to precipitation of diamonds at a later stage (1930±40 Ma; Richardson et al., 1993). The nature of these links is also connected to the growth and evolution of the SCLM underneath the Kaapvaal Craton (Figure 5.1) which is thought to have started as early as 3.6 Ga, as suggested by rhenium depletion model ages of Premier peridotite xenoliths that range from 3.6 to 2.0 Ga (Carlson et al., 1999). The 2.0 Ga age coincides with the Bushveld magmatic event at approximately 2.06 Ga (James et al., 2001; Shirey et al., 2002; Richardson and Shirey, 2008).

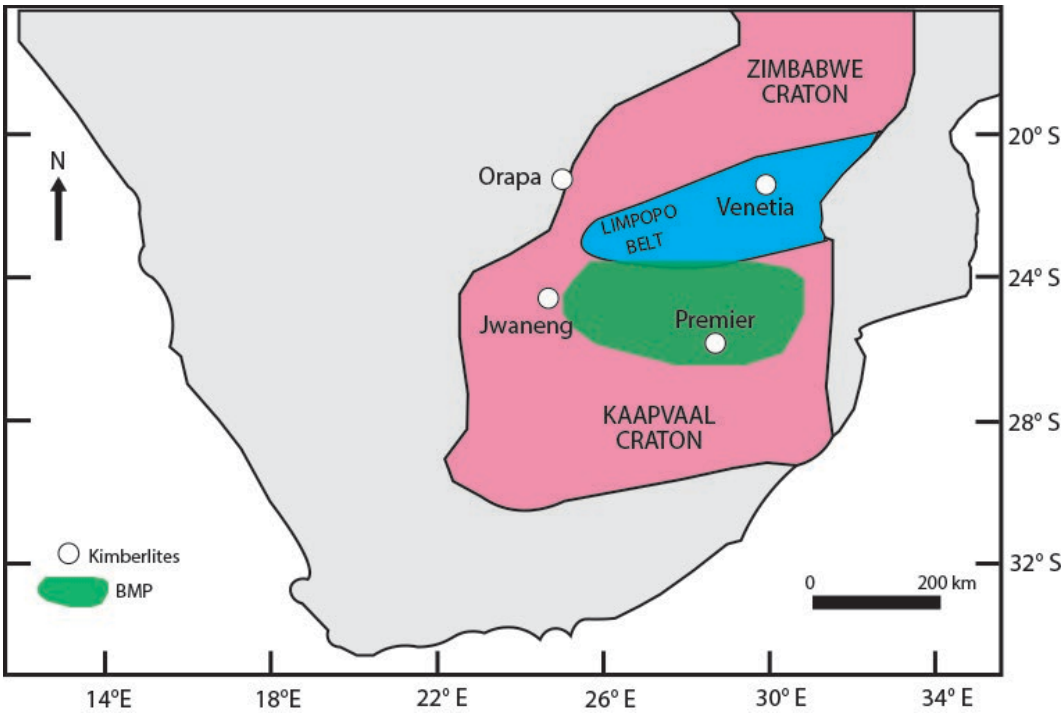

Figure 5.1. Map of Southern Africa showing the location of the Kaapvaal-Zimbabwe Craton and location of the Premier Kimberlite (white circle). Other kimberlite intrusions are Jwaneng,, Orapa, and Venetia. The green area reflects the extent of the Bushveld Magmatic Province. Figure sketched after Richardson and Shirey, 2008.

5.5. Samples and Methods

The samples reported in this paper were borrowed from the Boyd Collection at the Smithsonian Institution. The sample set includes both peridotite and eclogite xenoliths, as well as kimberlite matrix. A subset of the isotopic data was collected as part of a senior thesis by Greg Polley (2011: https://www.geol.umd.edu/undergraduate/paper/polley.pdf) and other data (petrographic and isotopic) were collected by me. The data evaluation presented herein is made on the basis of the combined dataset.

5.5.1. Petrography and Mineral Chemistry

Characterization of the mineral phases for selected samples was conducted using transmitted and reflected light petrography of polished thin sections. Additional characterization was done using a field emission Zeiss Auriga scanning electron microscope (SEM) at the Geophysical Laboratory of the Carnegie Institution for Science, with a working distance of 8.5 mm, 15 kV acceleration energy, and 60μm aperture.

The quantification of silicate mineral composition was made with WDS analysis (wavelength-dispersive X-ray spectroscopy) in a JEOL 8900R electron probe microanalyzer (EPMA) at University of Maryland. The calculation of Fe^{3+} was made through charge balance based on the cation and oxygen charge relationship. The quantification of sulfide phases was conducted at the Geophysical Laboratory of the Carnegie Institution for Science, using a JEOL 8530F electron microprobe analyzer, with accelerating voltage of 15kV, current of 20 nA, and beam size of 1 μm. Mineral abbreviations utilized in this chapter are: opx (orthopyroxene), ol (olivine), cpx (clinopyroxene), grt (garnet), mag (magnetite), sulf (sulfide).

5.5.2. Sulfur Isotopes

Isotopic methods used to obtain sulfur isotope analyses are the similar to those described in earlier chapters of this thesis. The samples are manually powdered in a ceramic mortar and pestle until the grains were finer than 0.350 mm, as measured through sieving. Approximately 2.5 grams of sample are reacted with a mixture of 20 mL of 5N HCl and 20 mL of CRS (Chromium (II) reduced) solution to produce silver sulfide. After the chemical extraction, the silver sulfide sample is kept in the dark for one week, and subsequently washed with MilliQ water and ammonium hydroxide in order to clean impurities. At this stage, pure silver sulfide is

dried and around 3 mg are wrapped in aluminum foil and put in a reaction vessel. Fluorine is added and the reaction produces sulfur hexafluoride (SF_6), which is then cryogenically separated from impurities and stored in glass manifold fingers.

The isotope composition of the SF_6 gas is measured with a Finnigan MAT 253 gas-source mass spectrometer. The isotope ratios are corrected to the V-CDT scale using the calibration presented in Dottin et al. (2018). Previous data of the Rustenburg Layered Suite (Penniston-Dorland et al., 2012; Magalhães et al., 2018) have also been recalculated to this calibration and are presented in this paper. Variations in mass dependent fractionation are given by equation 5.1. The mass independent composition is quantifiable in terms of a capital delta (Δ) notation (equation 5.2).

$$\delta^{3X}S = \left[\frac{\left(\frac{^{3X}S}{^{32}S}\right)_{\text{sample}}}{\left(\frac{^{3X}S}{^{32}S}\right)_{\text{V-CDT}}} - 1\right] \quad (5.1)$$

$$\Delta^{33}S = \delta^{33}S - [(1 + \delta^{34}S)^{0.515} - 1] \quad (5.2),$$

with these values being reported in units of permil (‰).

5.6. Results

5.6.1. Petrographic Observations of selected samples

5.6.1.1. Peridotites

The samples of peridotite xenoliths in this study consist of garnet-bearing lherzolites and harzburgites, spinel-bearing harzburgites and dunites and a polymict breccia (Table B.1). The xenoliths display variable mineral textures, from coarse-grained/undeformed to deformed/recrystallized (Figures 5.2a through 5.2d). The mineralogy of these xenoliths is dominated by Mg-rich olivine and orthopyroxene (Mg# 80-92; Table 5.1), and clinopyroxene, with variable contents of pyrope garnet, spinel, chromite, phlogopite, and sulfides. The degree of serpentinization in these samples varies from very little serpentine to almost fully overprinting the original minerals in the xenoliths, leaving only small remnants of olivine. Minerals associated with the serpentinized portion include magnetite, calcite, and in some cases, sulfides. Only one sample (FRB1318) shows an entirely different texture and set of mineralogy, a polymict breccia dominated by megacrysts of olivine, garnet, ilmenite, pyroxene, and phlogopite with a matrix rich in carbonate, phlogopite, and serpentine.

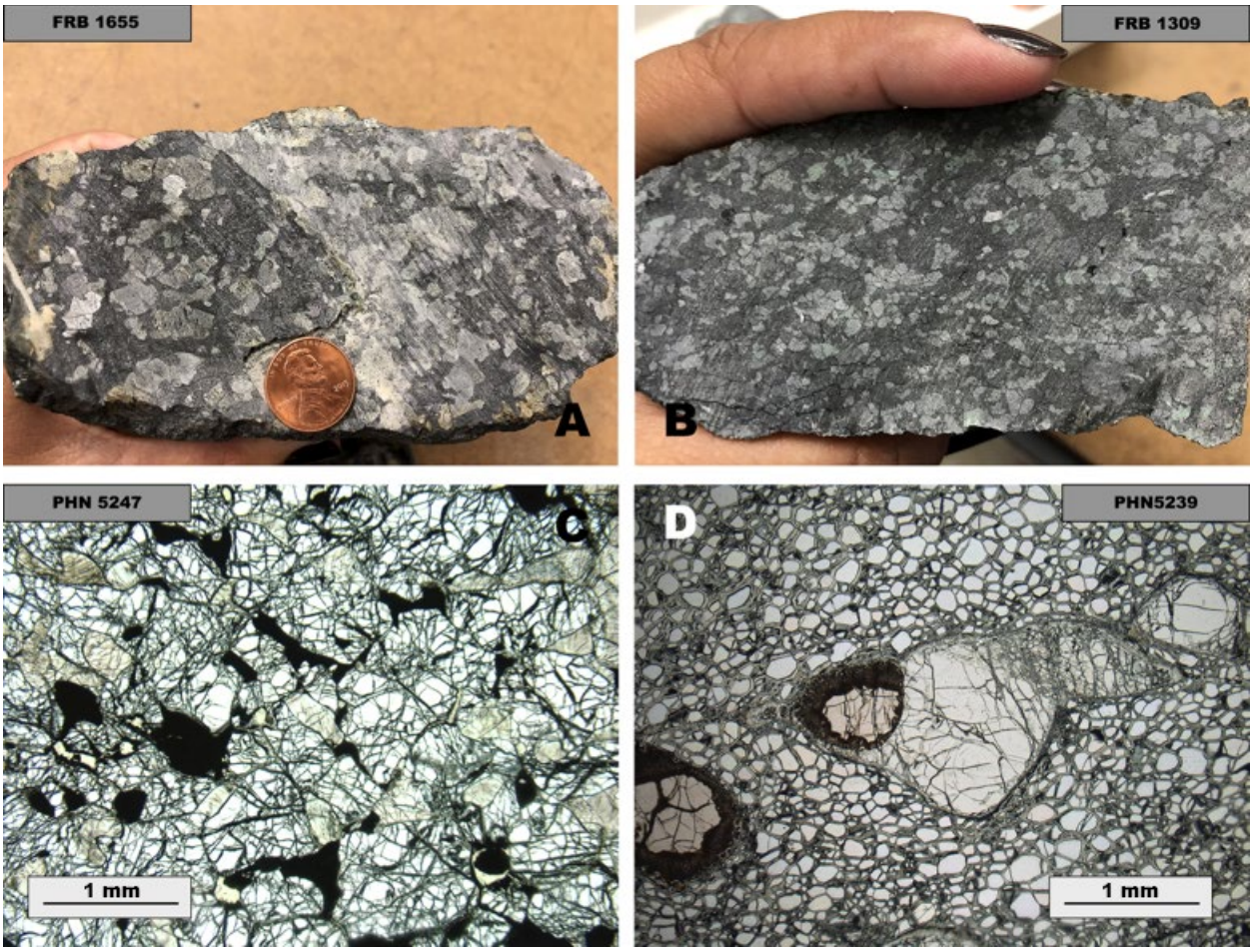

Figure 5.2. Different textures observed in peridotite xenolith samples. 5.2a. Hand sample of the sample FRB1655 (spinel harzburgite), with large crystals and little deformation; **5.2b.** Hand sample of sample FRB1309 (garnet lherzolite), displaying more fine grained minerals, with little deformation; **5.2c.** Sample PHN5247 (spinel harzburgite) with coarse grain size, without evidence for ductile deformation or significant serpentinization, plane polarized light. **5.2d.** Statically recrystallized grains of olivine form the matrix of this sample, which also have large orthopyroxene and garnet porphyroclasts, plane polarized light (sample PHN5239, garnet harzburgite).

Table 5.1. Mineral chemistry data of olivine, orthopyroxene, clinopyroxene, and garnet, from peridotite xenoliths from the Premier Kimberlite.

SAMPLE	FRB130	PHN523	PHN524	FRB130	PHN523	PHN524	FRB130	PHN523	PHN524	FRB130	FRB523	FRB524
	Olivine	Olivine	Olivine	Opx	Opx	Opx	Cpx	Cpx	Cpx	Garnet	Garnet	Garnet
n	13	6	8	15	7		5	5	3	7	5	4
Na_2O	0.04	0.03	0.01	0.17	0.29	0.02	2.20	1.72	1.70	0.10	0.10	0.07
FeO	7.84	8.03	19.05	5.10	5.16	12.98	2.51	3.37	4.34	7.18	6.32	6.93
TiO_2	0.02	0.02	0.01	0.10	0.23	0.04	0.26	0.38	0.81	0.21	1.28	0.20
K_2O	0.01	0.01	0.00	0.01	0.00	0.00	0.07	0.04	0.00	0.00	0.01	0.01
Al_2O_3	0.01	0.03	0.01	1.34	1.40	4.33	3.31	2.27	5.88	21.71	18.75	21.83
MgO	50.15	50.18	41.97	34.43	33.70	29.26	16.95	20.48	14.16	21.72	22.48	21.86
MnO	0.09	0.09	0.20	0.10	0.11	0.23	0.07	0.12	0.09	0.35	0.25	0.31
Cr_2O_3	-	-	-	0.25	0.40	0.20	1.72	1.27	0.60	2.73	4.48	2.84
CaO	0.04	0.06	0.01	0.60	1.65	0.37	18.23	15.04	21.01	4.46	5.01	4.49
SiO_2	41.08	41.23	39.42	56.53	56.32	53.33	54.72	55.41	52.16	41.52	41.14	41.41
NiO	0.39	0.35	0.22	-	-	-	-	-	-	-	-	-
Total	99.67	100.04	100.89	98.63	99.26	100.77	100.03	100.09	100.74	99.98	99.82	99.96
Mg#	91.9	91.8	79.7	92.3	92.1	80.1						

The sulfides in the peridotite xenoliths include pentlandite [$(Fe,Ni)_9S_8$], pyrrhotite ($Fe_{1-x}S$), and heazlewoodite (Ni_3S_2), with minor chalcopyrite ($FeCuS_2$) and pyrite (FeS_2) present in a few samples. Sulfides occur as tiny crystals (<20μm) associated with the magnetite in serpentinized portions of the sample, and rarely occur as larger crystals. The sulfate barite ($BaSO_4$) occurs sparsely in these rocks. Sulfides are not found as inclusions within any silicate mineral.

Two peridotite samples, PHN5247 and FRB1309, have sulfides that reach up to 0.5mm in diameter, and exhibit features indicative of oxidation and sulfide loss. Sample PHN5247 is a spinel lherzolite with lower olivine and orthopyroxene Mg# (~80) than other samples and contains magnetite, serpentine, calcite, and sulfides as accessory phases. The sulfides in this sample can measure up 500μm in size and include associations of pentlandite $(Fe_4Ni_{4.6}Co_{0.3})S_8$ and pyrrhotite ($Fe_{0.83}S$), with minor chalcopyrite ($FeCuS_2$) (Table 5.2) and often show oxidation to magnetite (Figure 5.3a through 5.3d). Pentlandite is also found as lamellae within the pyrrhotite (Figure 5.3b), and some pentlandite-pyrrhotite pairs also contain a minor amount of chalcopyrite associated (Figure 5.3d). Minor quantities of heazlewoodite were observed as well in this sample. Sample FRB1309 is a garnet harzburgite (Mg# ~92) containing accessory serpentine, magnetite, calcite, and sulfides. This sample also shows reaction textures of sulfide, including greater replacement of sulfide by magnetite (oxidation) and reaction to produce heazlewoodite (Figure 5.4a through 5.4d).

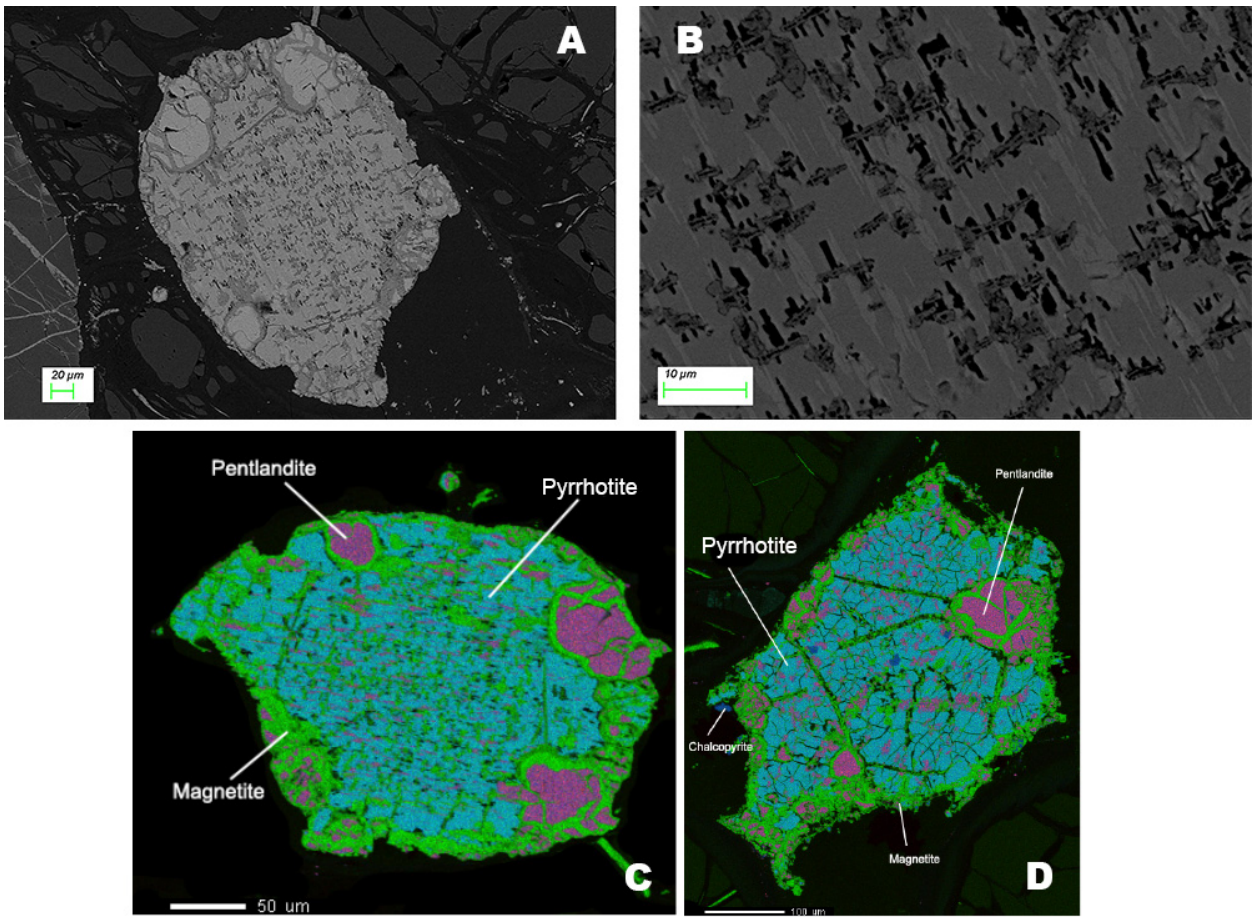

Figure 5.3.a. Sulfide grain in sample PHN5247 (spinel harzburgite) consists of an association of pentlandite and pyrrhotite, which are being altered into magnetite. **3b.** Close up look at the association between pyrrhotite (medium gray), pentlandite (lighter grey), and magnetite (darker gray). **3c and 3d:** Compositional map of sulfides from sample PHN5247, showing the textural relationships between pentlandite, pyrrhotite, magnetite, and chalcopyrite (when present). Pentlandite is also being exsolved from pyrrhotite.

Table 5.2. Sulfide mineral chemistry of sample PHN5247.

	Chalcopyrite	Pentlandite	Pyrrhotite
n	2	30	24
S	35.67	33.90	40.34
Pb	0.02	0.04	0.06
Fe	30.95	29.44	58.87
Ni	0.04	35.57	0.53
Cu	33.99	0.04	0.01
Zn	0.05	0.01	0.02
Co	0.05	2.02	0.11
Total	100.78	101.01	99.94

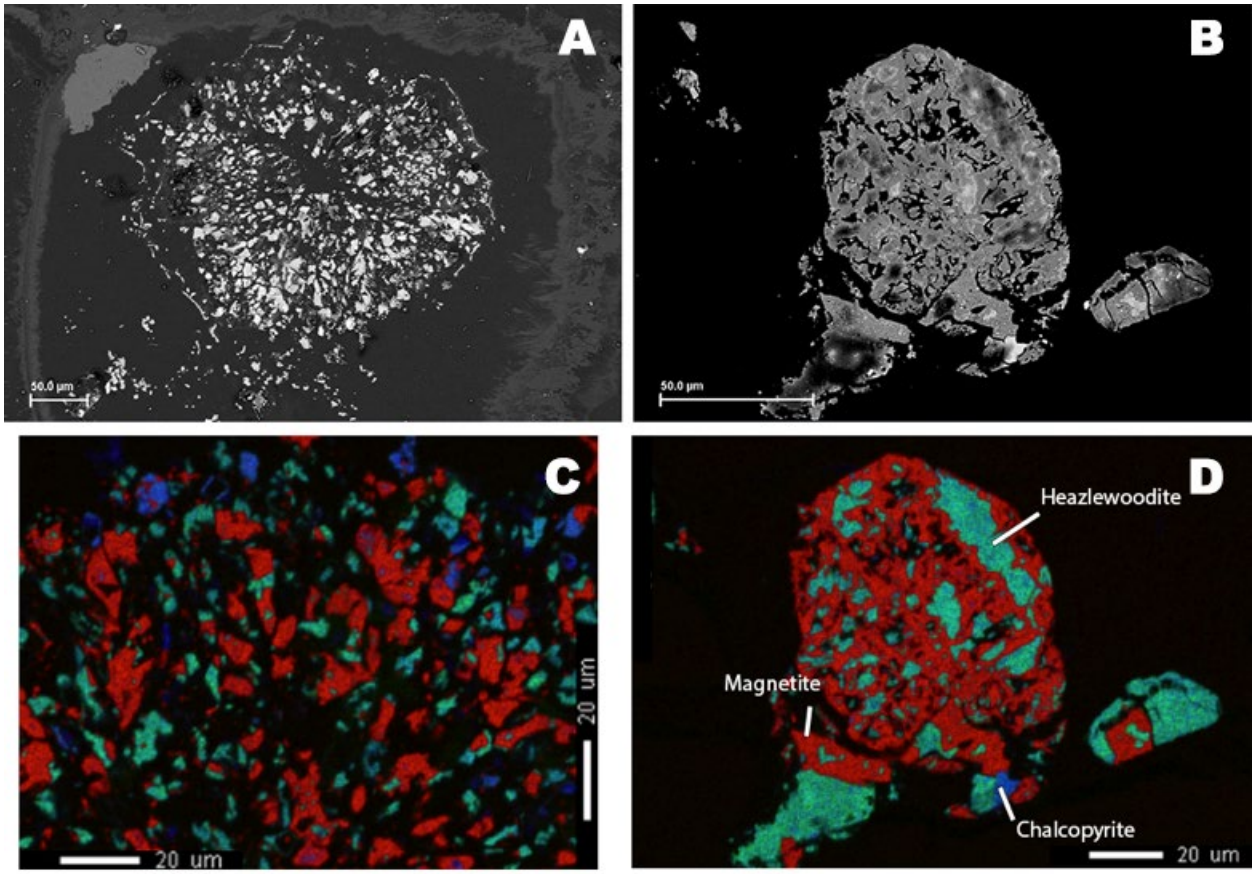

Figure 5.4 Images of sulfides from sample FRB 1309 (garnet lherzolite). **a.** BSE image of pseudo-sulfide shape, surrounded by serpentine, which is now an aggregate of sulfides surrounded by serpentine. **b.** BSE image of sulfide (brighter regions) surrounded by magnetite, which implies a high degree of oxidation and loss of sulfur; **c.** Compositional map of sulfides from figure 5.a. A closer look at this grain shows a multi-component assemblage, with magnetite (red), heazlewoodite (cyan), and chalcopyrite (blue).**d.** Compositional map of sulfide from sample 5b. Red colors showing the magnetite surrounding the heazlewoodite (cyan). The blue spot is chalcopyrite**.**

5.6.1.2. Eclogites

Two eclogite samples studies here contain pyroxene and Ca-Mg-rich garnet, with alteration along fractures (Figure 5.5c, 5.5d). Sample FRB908 D2 preserves pyrite, which occurs as large (up to 600µm, Figure 5.5c) grains that show inclusions of silicate phases

and as infill between silicate grains (Figure 5.5d). The silicate inclusions in pyrite are the same as the rock matrix, demonstrating that the pyrite grew after the rock already was under eclogite facies conditions. The pyrite grains contain inclusions of galena and chalcopyrite (Figure 5.5c). In addition to occurring as inclusions within the pyrite, chalcopyrite is also observed as grains associated with mica in alteration veins.

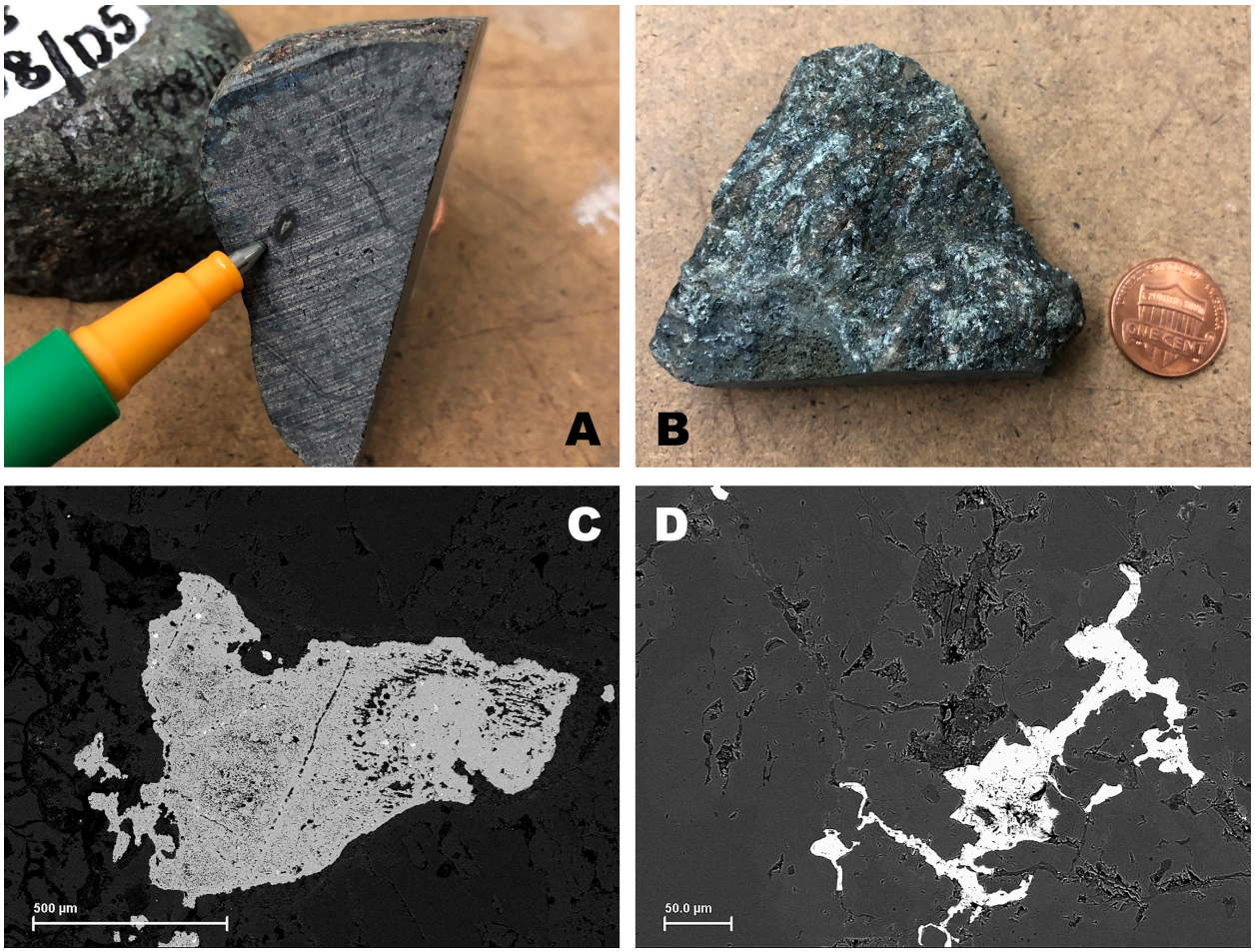

Figure 5.5. a. Eclogite hand sample FRB 908D2, sulfide within garnet crystal **b.** Eclogite hand sample FRB 908D2. **c**. BSE image of pyrite grain with inclusions of matrix minerals (dark spots) and other sulfides, such as galena (bright spots) **d.** BSE image of interstitial pyrite with no inclusions or association with other sulfides.

5.6.1.3. Kimberlite Matrix

The kimberlite matrix is a generic term for a group of heterogeneous samples that represent the distinct types of rocks associated with the Premier intrusion (Figure 5.6a and 5.6b), consisting of kimberlite and carbonatites, from the different units (i.e. black, green, gray). The mineralogy of all these samples consist mostly of serpentine and carbonate, which are alteration minerals in this case, pseudomorphing everything. Other phases that have been recognized include pyroxene, perovskite, magnetite, ilmenite, spinel, and phlogopite. Sulfide grains are rare and sparse in these rocks, and the only mineral phase I was able to identify was pentlandite. Tsai et al. (1979) also reported the presence of pyrite and chalcopyrite, in addition to pentlandite. There is a significant variation in rock composition and mineralogy between the samples, which reflects the complexities of these rock types.

Figure 5.6. a. Photograph of hand sample FRB1367-21. Note the lack of large crystals; **b.** Photograph of hand sample FRB 900C2, where it is possible to distinguish a large crystal that has been replaced by serpentine.

5.6.2. Sulfur Isotopes

The sulfur isotope composition of sulfides from peridotite and eclogite xenoliths, and the Premier kimberlite matrix is shown in Figure 7. Multiple isotope data from various parts of the Bushveld province (Rustenburg Layered Suite: Lower Zone, Marginal Zone, and Basal Ultramafic Sequence; Penniston-Dorland et al., 2012; Magalhães et al., 2018; Chapter 3 of this thesis; Waterberg Project, Chapter 4 of this thesis) and for the mantle (Peters et al., 2010; Labidi et al., 2012) are included in order to place the data in context of the BMP magmas and likely compositions of mantle-derrived melts. This figure illustrates the wide range of $\delta^{34}S$ values of peridotite xenoliths (compared to MORB and BMP magmas), from -3.25‰ to +9.57‰ (Figure 7, Table 1) and a smaller range of variation for $\Delta^{33}S$ values extend from 0.028‰ to 0.077‰ excepting sample PHN5247, which has a $\Delta^{33}S$ of 0.179‰. All $\Delta^{33}S$ values are clearly distinct from MORB compositions, but the most common values overlap with the compositions of some of the RLS and WP magmas, in particular the Lower Bushveld Series (LBS). The $\delta^{34}S$ values of the eclogite xenoliths are -5.34‰ and -2.89‰, and the $\Delta^{33}S$ values of these xenoliths yields 0.050‰ and 0.043‰. While the $\Delta^{33}S$ overlaps within uncertainty of the range of values for the MORB, the $\delta^{34}S$ does not overlap with either MORB or Bushveld magmas. The $\Delta^{33}S$ are nonzero and similar to those seen for sulfur from the peridotite xenoliths. The matrix of the Premier Kimberlite has sulfides yielding $\delta^{34}S$ values between -0.67‰ to +2.98‰ and $\Delta^{33}S$ values between 0.060‰ and 0.102‰, which fall within the range of $\delta^{34}S$ defined by the peridotite xenoliths, although the $\Delta^{33}S$ average is slightly higher in the kimberlite matrix. The range of sulfur isotope compositions for these three kimberlite matrix samples overlaps that of the Bushveld

samples and is distinct from MORB. No relationship is observed between sulfur isotopic composition and the deformation state of the samples. Although there are variable degrees of serpentinization in the xenoliths, they do not appear to be correlated to the variability of $\delta^{34}S$.

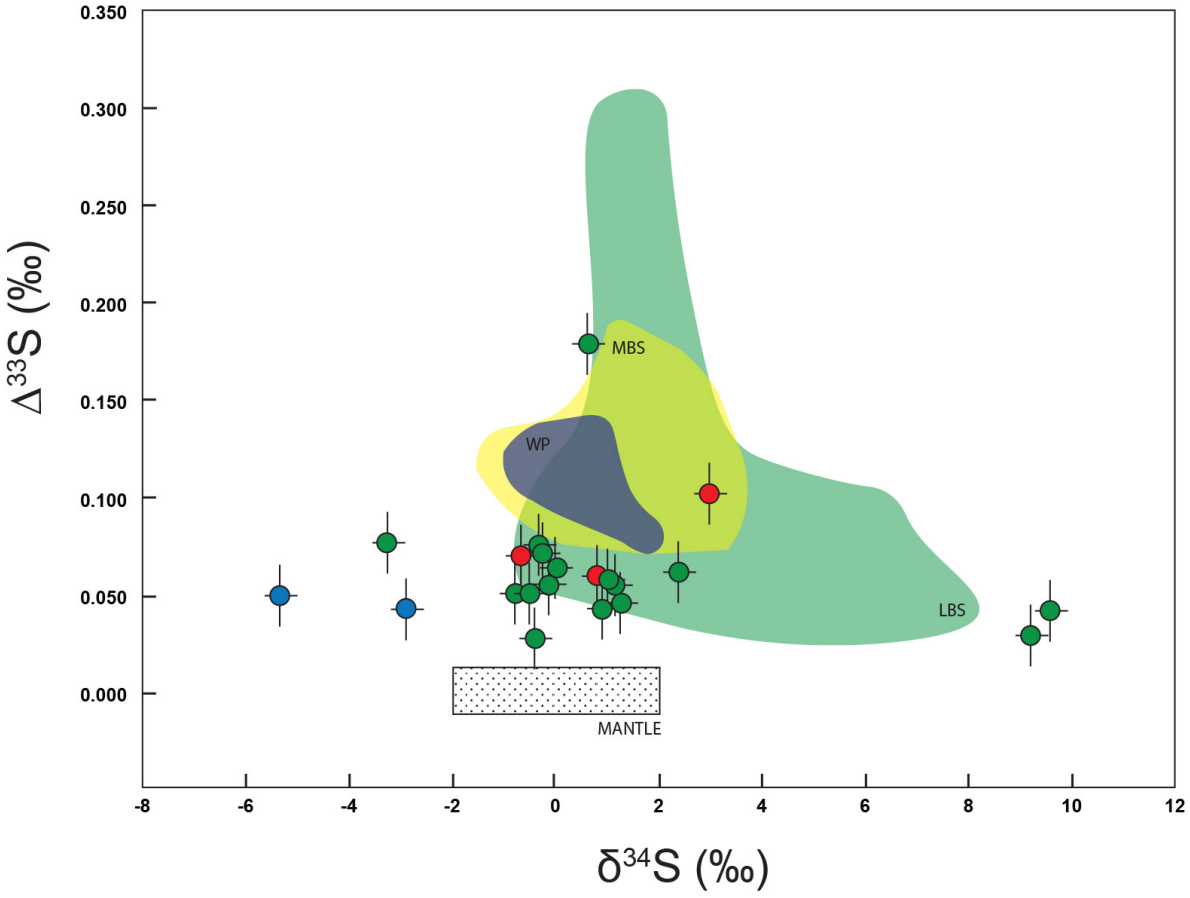

Figure 5.7. Diagram of $\delta^{34}S$ versus $\Delta^{33}S$ showing sulfur isotope composition data of sulfides from the matrix and peridotite (green circle), eclogite (blue circle), and matrix of the Premier Kimberlite (red circles). The green field denotes the known composition of the Lower Bushveld Series in the Clapham Section (Chapter 3), the yellow area denotes de composition of the Main Bushveld Series (Chapter 2), and the blue area corresponds to the composition of the Waterberg Project (Chapter 4). Sulfur isotope composition of the unaltered mantle (Peters et al., 2010; Labidi et al., 2012) is represented by a dotted box.

Table 5.3. Multiple sulfur isotope composition of the peridodite and eclogites xenoliths from the Premier Kimberlite, along with analyses of kimberlite matrix samples.

PERIDOTITES	$\delta^{33}S$	$\delta^{34}S$	$\delta^{36}S$	$\Delta^{33}S$	$\Delta^{36}S$
FRB1655	0.647	1.149	2.225	0.055	0.040
FRB1656	-0.090	-0.323	-0.979	0.076	-0.366
FRB1352	-0.350	-0.778	-1.403	0.051	0.074
FRB1370	-0.054	-0.243	-0.410	0.071	0.052
FRB1318	0.577	1.008	1.793	0.058	-0.122
FRB1309	0.513	0.913	2.040	0.043	0.306
FRB1375	-0.211	-0.509	-1.080	0.051	-0.113
FRB1657	0.069	0.008	0.229	0.064	0.214
FRB1331.3	4.753	9.194	17.224	0.029	-0.316
FRB1659	1.289	2.385	4.772	0.062	0.235
PHN5247	0.509	0.641	1.210	0.179	-0.009
PHN5239	-0.172	-0.388	-0.714	0.028	0.023
FRB1359	0.702	1.273	2.814	0.046	0.394
FRB1302	-1.600	-3.254	-6.282	0.077	-0.107
FRB1323	-0.005	-0.120	-0.212	0.056	0.015
FRB914	4.961	9.573	18.984	0.042	0.718
KIMBERLITES					
FRB900-C2	0.474	0.803	1.674	0.060	0.147
FRB1367-21	1.638	2.984	5.555	0.102	-0.122
FRB1367-14	-0.275	-0.670	-1.210	0.070	0.064
ECLOGITES					
FRB908-D2	-1.446	-2.890	-5.443	0.043	0.040
FRB908D5	-2.704	-5.339	-10.117	0.050	0.003

5.7. Discussion

Previous studies of the sulfur isotopic composition of the sub-continental lithospheric mantle in Africa have been centered on measurements of sulfide inclusions in diamonds due to the almost certain preservation of the sulfur isotopic composition at

the time of diamond formation. Measurements of P-type sulfide inclusions from Jwaneng diamonds (Thomassot et al., 2009), show that the sulfur isotopic composition follows the terrestrial fractionation line, with $\delta^{34}S$ values between -0.98‰ to 0.29‰. This is in contrast to the composition of E-type sulfide inclusions that record an ancient recycled component in the mantle ($\Delta^{33}S$ between. -0.5‰ to 0.9‰). Farquhar et al. (2002) found a $\Delta^{33}S$ signature between -0.11‰ to 0.61‰ in E-type sulfide inclusions from the Orapa Kimberlite. A more recent study of the Bultfontein Kimberlite, an intrusion associated with the Kimberley event, finds that bulk-rock $\delta^{34}S$ values of -3.4‰ to +0.8‰ in peridotites represent a contribution of a recycled component in the SCLM. However, this study concluded that the sulfur did not originate from an Archean material because no resolvable S-MIF signature was observed (Giuliani et al., 2016).

All samples reported in this chapter show a large variation in $\delta^{34}S$ values (-5.34‰ to +9.57‰), but these same samples also show a clear resolvable S-MIF signature in the form of positive $\Delta^{33}S$ values (0.028‰ to 0.179‰) that are not as variable. These sulfur isotope compositions are distinct from the $\delta^{34}S$ values of -2‰ to +2‰ and $\Delta^{33}S$ of 0±0.008‰ defined by MORB (Sakai et al., 1984; Labidi et al., 2014), which are used as a proxy for melts derived from depleted (upper) mantle. The $\Delta^{33}S$ suggests a contribution from an S-MIF source. The question is whether these non-zero $\Delta^{33}S$ values reflect late addition of sulfur to the xenoliths (such as from crustal rocks via hydrothermal exchange) or if they reflect the composition of sulfur that was present in the SCLM from which the xenoliths were derived. Although external fluids might have played a part in the story of Premier magmatism, there is no evidence at the moment, either petrographic or isotopic, for large-scale introduction of sulfur in the xenoliths. The Transvaal Supergroup,

intersected by the kimberlite at depth (Maier et al., 2008), is the only known unit that could contribute a significant amount of sulfur to this intrusion in case of sulfur mobilization in fluids. If the fluid in these processes of fluid-rock interaction was sourced from multiple units, it would likely contain anomalous sulfur of variable composition which would in a heterogeneous isotopic record in both $\delta^{34}S$ and $\Delta^{33}S$ in the xenoliths and the kimberlite matrix, unless well-homogenized at a posterior time. The question examined next is whether the observations support a SCLM origin for the nonzero $\Delta^{33}S$.

The petrographic observations presented in this chapter suggest that there are different generations of sulfide minerals and reactions that have consumed sulfide, as exhibited by textures seen in PHN5247 (Figure 5.4) and FRB 1309 (Figure 5.5)), or in some specific cases may have produced it. The presence of magnetite replacing sulfide minerals in both of these samples suggests sulfur loss and implies oxidation rather than reduction. Sulfur loss is further evidenced by the transformation of pentlandite to heazlewoodite (FRB1309) and by the magnetite alteration halo around the remaining sulfide grains. This, in turn, is most consistent with the most of the sulfur remaining, and its isotopic signature being related to the original sulfides, rather than extensive addition of sulfide sulfur during serpentinization. The loss of sulfur could have occurred during any part of the xenolith evolution, and it is not necessarily associated to the interaction with the kimberlite.

Another line of evidence supporting the hypothesis that the sulfide sulfur carries the $\Delta^{33}S$ from their SCLM source comes from the wide range of $\delta^{34}S$ (-3.25‰ to +9.57‰) but limited variability in $\Delta^{33}S$ (0.028‰-0.077‰) observed for peridotite xenoliths that suggests a process fractionated $^{34}S/^{32}S$, but that did not shift the $\Delta^{33}S$. Fluid

metasomatism in the mantle wedge has been reported to generate large $\delta^{34}S$ variations, through processes that can also enrich the xenoliths in PGE (Rielli et al., 2018). This observation is consistent with the interpretation that significant amounts of exogenous sulfur were not added as sulfide to the peridotites during kimberlite magmatism and provides an argument for the case that the SCLM underneath the RLS contains the nonzero $\Delta^{33}S$, implying a preservation of recycled sulfur to the mantle.

The eclogite sulfur may also be of mantle origin, and similar $\Delta^{33}S$ (0.043‰-0.050‰) allows this possibility if the SCLM has a positive $\Delta^{33}S$, as inferred from the peridotite data just presented and data presented for sulfide inclusions in diamond of Farquhar et al. (2002) and Thomassot et al., (2009). The eclogites here have negative $\delta^{34}S$ and it is unclear if this is a primary signature or the result of some sort of secondary process. The petrographic relationships for sulfide in eclogite (FRB908) show two generations of sulfide, with the most abundant exhibiting complex textures that include matrix silicate minerals that are interpreted to form during eclogite facies metamorphism. The second generation, inferred here to be younger, refers to pyrite precipitated in veins. Therefore, this suggests that heterogeneity of sulfur isotopic composition occurs within the same sample and further in-situ studies would need to be carried out.

Interaction between kimberlite and peridotite xenoliths can happen both during magmatism and post-magmatic processes. Gregoire et al. (2003) argued that light rare earth element patterns in clinopyroxenes suggest that geochemical interaction between the peridotite xenoliths and the Premier kimberlite magma occurred. While it is possible, maybe likely, that the kimberlite sulfur could also contain crustal sulfur imparted during the magmatic and post-magmatic stage, the more positive $\Delta^{33}S$ found in this study

referred to sulfides in peridotite sample PHN5247, which could not have been added from the known composition of the kimberlite. This also allows for a suggestion that the kimberlite sulfide sulfur could be derived from an SCLM source. In another study, Tsai et al. (1979) found a similar range of $\delta^{34}S$ in the Premier matrix sulfides, 0.2‰ (in pentlandite+chalcopyrite) to 1.3‰ (in pyrite). These authors concluded that these values represented a magmatic origin for the sulfides. Studies reveal that few measurements of $\delta^{34}S$ in other kimberlites overlap with mantle values, indicating that processes that fractionate isotopes can play an important role (Giuliani et al., 2014), and in particular those related to volatile nature of these magmas. Kimberlites have very wide ranges of sulfur isotopic composition. Sulfides can reach $\delta^{34}S$ values of up to +52‰ at the Mir Kimberlite, in Russia (Vinogradov and Ilupin, 1972), while southern African kimberlites usually range between (-3 to +12‰; Giuliani et al., 2014).

A final question is how this data and the possibility of an SCLM with positive $\Delta^{33}S$ relate to the larger question of sulfur ($\Delta^{33}S$) in the initial Bushveld magmas. The similarity of the $\Delta^{33}S$ for the peridotite xenoliths and magmas from the BUS provides support for assertions made previously in this dissertation that the melts already possessed anomalous $\Delta^{33}S$ at the time of their emplacement, and only in some locations such as in the Marginal Zone or near magma chamber boundaries it was subsequently shifted by further addition of exogenous sulfur. The more extreme $\Delta^{33}S$ of some RLS magmas may also be primary, as at least some samples (PHN5247) have more positive $\Delta^{33}S$ signatures that fall within the field defined by the Main Bushveld Series of the Rustenburg Layered Suite ($\Delta^{33}S$=0.179‰).

No reliable data exists for Sr, Nd, and O isotopes for the Premier xenoliths, therefore making mixing calculations difficult to be performed. A brief look at the one whole-rock $^{87}Sr/^{86}Sr_{(T)}$ data point ($^{87}Sr/^{86}Sr_{(i)}$ = 0.70150) produced by Walker et al. (1989) suggests that the SCLM peridotites do not have an ideal composition to be a source of the RLS magma, also supported by their one whole-rock $^{143}Nd/^{144}Nd$ data ($^{143}Nd/^{144}Nd$ = 0.512137±62). Carlson et al. (1999) found whole-rock $^{187}Os/^{188}Os_{(i)}$ values ranging from 0.10953 to 0.11612, which records one of the lowest $^{187}Os/^{188}Os$ measured for terrestrial rocks and reflects their early depletion. Sulfide inclusions deriving from an eclogite-type source show a much different range of Os concentration and isotopic compositions. The concentration of Os in these sulfides is much higher than in the peridotite xenoliths (up to 10,560 ppb, versus a maximum of 8.23 ppb for the peridotites; Richardson and Shirey, 2008; Carlson et al., 1999). The $^{187}Os/^{188}Os_{(i)}$ isotopic composition ranges from 0.1986 to 0.3154.

The possibility of a SCLM with recycled components can be further assessed with mixing calculations. For this, I chose to compare the known Os and S compositions and concentrations for the peridotite xenoliths (Carlson et al., 1999; this study) to the values of a mantle-derived melt with 10% melt (similar to Schoenberg et al., 1999). I also plotted the Os compositions of E-type sulfide inclusions (Richardson and Shirey, 2008), and used the highest positive value found by Farquhar et al. (2001) as an estimate of sulfur isotopic composition, with an arbitrary concentration of 500 ppm in eclogites. The mantle values used were from Labidi et al., 2014 for sulfur, and Meisel et al., 1996 for Os, with the SCLM as a contaminant. I used the highest values found for both Os and S in all cases, therefore representing a best-case scenario for the peridotite and eclogite

compositions. These show that the peridotite xenoliths are not a viable contaminant for the Bushveld magmas despite their non-zero $\Delta^{33}S$. ,However, the E-type sulfides could potentially be the These calculations also imply in mixing of the mantle with a reservoir with much higher Os concentration than the Premier xenoliths, and a $^{187}Os/^{188}Os_{(i)}$ ratio much higher than the mantle, possibly similar to what is seen in these E-type inclusions.

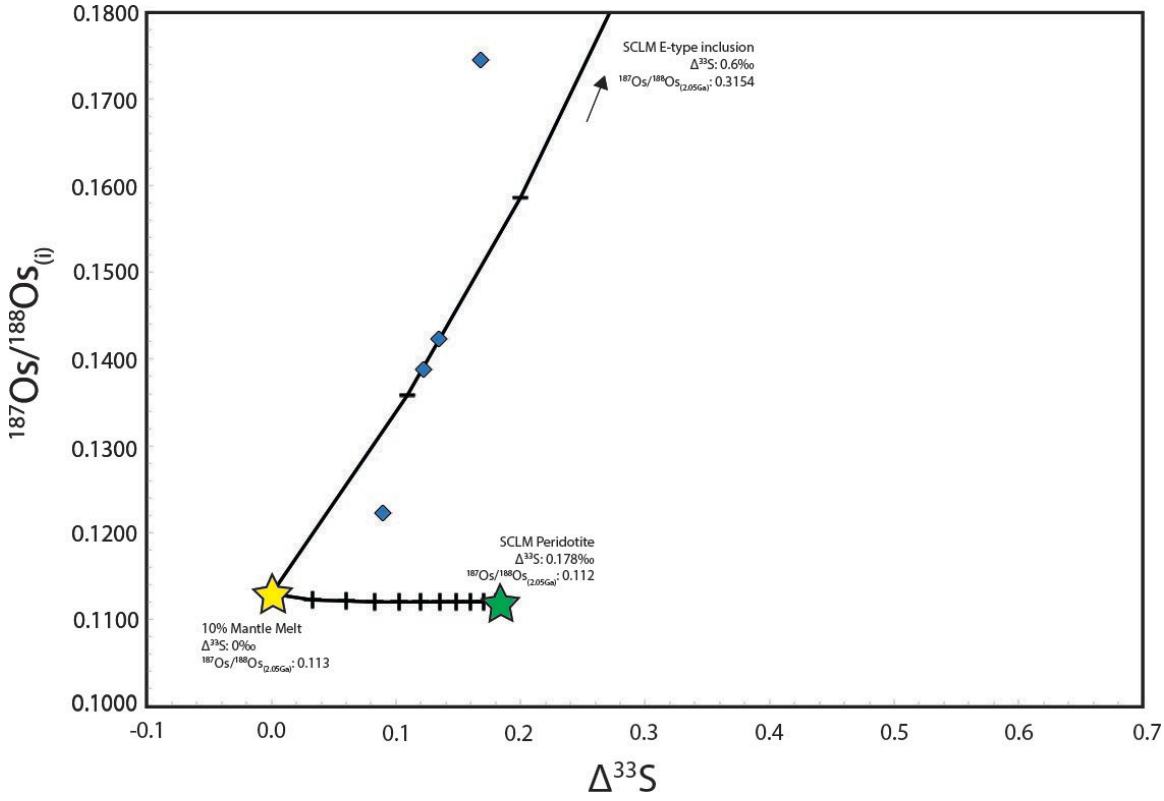

Figure 5.8. Mixing calculation between S and Os for different reservoirs. E-type sulfide inclusions (out of picture, Farquhar et al., 2001; Richardson and Shirey, 2008) and peridotite xenoliths (green star, Carlson et al., 1999; this study) were evaluated as possible compositional end members for a starting composition similar to a mantle melt (yellow star, Labidi et al., 2014; Meisel et al., 1996). The blue diamonds correspond to samples from the Critical Zone of the RLS (Schoenberg et al, 1999; Magalhães et al., 2018).

5.8. Conclusions

The Premier Kimberlite samples the sub-continental lithospheric mantle (SCLM) underneath the Rustenburg Layered Suite (RLS). Here, I find that the xenoliths and the kimberlite matrix have a composition that significantly differs from the expected mantle values in both $\delta^{34}S$ and $\Delta^{33}S$. Although peridotites and kimberlite typically would have a very distinct genesis, their values are indistinguishable, with a wide range of $\delta^{34}S$ values, but a narrow range for $\Delta^{33}S$. Eclogite xenoliths tend to have lighter sulfur, but are still within the peridotite range of values. Of the possible explanations for the presence of the $\Delta^{33}S$ signatures: (a) S-MIF is brought by an external fluid that completely overprinted the S isotope composition of the Premier Kimberlite and the xenoliths it contains; (b) S-MIF was present only in the xenoliths prior to kimberlite eruption and was redistributed throughout the Premier Kimberlite; or (c) S-MIF was present in both Premier Kimberlite and xenoliths prior to kimberlite eruption.

Melt depletion during formation of the Kaapvaal Craton cannot be invoked as a cause of non-zero $\Delta^{33}S$ in these mantle-derived samples because this process does not fractionate sulfur mass-independently. This, combined with inferences that primordial terrestrial (mantle) sulfur has $\Delta^{33}S$ of zero, lead to the suggestion that any inferred positive $\Delta^{33}S$ of the SCLM reservoirs from which these peridotite and eclogite xenoliths derived acquired this signature from recycling of Archean material, either in the mantle or during kimberlite emplacement in the crust. The nonzero $\Delta^{33}S$ is suggested, in this study, to be a feature of a contaminated SCLM. This does not rule out secondary shifts to $\Delta^{33}S$, but it implies that the primary control is the source. The cause of variability for $\delta^{34}S$ is less clear. A significant role is envisioned for fractionation processes occurring during

and after emplacement, but some variability may also be primary. Thus the peridotite and eclogite xenoliths, and Premier kimberlite matrix all have a sulfur composition that reflects a surface-derived component (S-MIF) component, although its origin remains not fully understood. Data from E-type sulfide inclusions provide evidence for the involvement of the SCLM in the Bushveld magmatism as a source of sulfur, however the whole-rock sulfur data presented in this study should not be interpreted as a strong evidence for a SCLM origin of the anomalous sulfur in the RLS.

6. Conclusions

6.1. Overview

This dissertation has focused on the sulfur isotope composition of two igneous bodies from the Bushveld Magmatic Province, the Rustenburg Layered Suite and the Waterberg Project, and evaluates possible sources of sulfur for the magma of these two intrusions. Solving the question of source of sulfur is important because it correlates directly to the platinum group element (PGE) chemistry and the formation of the PGE deposits hosted by these intrusions. It also provides important information about the behavior of sulfur during magma-rock interactions and how this reflects in the sulfur isotope composition of the RLS.

Chapters 2 and 3 reported the first systematic study of multiple sulfur isotopes in all the units of the Rustenburg Layered Suite, from its most basal unit, the Basal Ultramafic Sequence, to the granophyres at the roof of the Upper Zone, and showed that the sulfur composition has an Archean crustal component. Chapter 3 also reported mineral chemistry data for the Marginal Zone and Basal Ultramafic Sequence, which aided the evaluation of the origin of anhydrite, a calcium sulfate which presence is uncommon in mafic magmas. Chapter 2 also reported sulfur isotope data of the Vredefort Dome, a possible proxy for the lower crust underneath the Rustenburg Layered Suite. It showed that while a model of assimilation in the lower crust exists, the sulfur composition does not match what is needed to contaminate the BUS.

The multiple sulfur isotope composition of the Waterberg Project was reported in Chapter 4. Also associated with the Bushveld Magmatic Province, the Waterberg Project is a separate intrusion, but the sulfur isotope composition was shown to be similar to the Main Bushveld Series.

Chapter 5 examined xenoliths of the Premier Kimberlite to evaluate the composition of sub-continental lithospheric mantle underneath the Kaapvaal Craton in order to assess whether it contains recycled sulfur and if it could have been a source for the Bushveld Magmatic Province sulfur.

The main results and conclusions of each chapter of this dissertation are summarized below.

6.2. Summary

6.2.1. Chapter 2

Previous studies suggested the isotope composition of magmatic sulfur in the Rustenburg Layered Suite was not compatible with the expected value of a mantle-derived melt. Although models called for assimilation of crustal sulfur as a trigger of sulfur saturation in the magma, this finding brought to light very basic questions, as multiple sulfur isotope data were not available for the majority of the RLS. The study in Chapter 2 added to understanding of the RLS knowledge by systematically looking at all units, and shows that the entire intrusion has magmatic sulfur that carries a signature of crustal contamination. Variation of sulfur isotopes is shown with stratigraphic depth,

which correlates to changes in the compositions of other radiogenic systems and allows for the distinction of at least two different contaminants in the intrusion.

The concept of a staging chamber model in the lower crust that would contain RLS magma is a widespread idea, and previous studies have inferred contamination from the lower crust to explain trace element patterns in the rocks (Wilson et al., 2017). The Vredefort Dome, an impact crater that contains exposed middle- to lower crust rocks, was used as a proxy for the composition of the lower crust. Their multiple sulfur isotope composition and low sulfur concentrations show that assimilation of these rocks cannot account for the sulfur composition of the RLS.

6.2.2. Chapter 3

The drilling of the Clapham Core, and the recent discovery of the Basal Ultramafic Sequence, now considered the most basal unit of the Rustenburg Layered Suite, provides an opportunity to study the most primitive magmas of the intrusion and understand how deeply the exogenic sulfur signal extends into the BMP magmas and ultimately their source(s), extending to whether their composition reflects a pristine or altered mantle source. The multiple sulfur isotope profile of this core extends through the Lower Zone, Marginal Zone, and Basal Ultramafic Sequence, showing that even the most primitive magmas of the Rustenburg Layered Suite have a crustal component. In the Marginal Zone, the shifts to more positive $\Delta^{33}S$ (larger anomalies) are shown to be related to assimilation of host rock – highlighting one known way that the BMP magmas acquired anomalous sulfur – but the presence of a constant, low level $\Delta^{33}S$ signature in

the BUS (and LZ) provides further support that these magmas were intruded already with such a signature present. A feature of the BUS that is also described is the presence of anhydrite. The sulfur isotope composition of sulfides and of anhydrite, present in the Basal Ultramafic Sequence, provides further evidence that the sulfate is not late, or a result of assimilation of sulfate host rocks, but is considered here to be magmatic in origin and a feature of these magmas.

6.2.3. Chapter 4

The Waterberg Project (WP) is a mafic-ultramafic intrusion in the southern margin of the Limpopo Belt that has been linked to the Bushveld Magmatic Event due to its age and geochemistry. Despite a close spatial association with the Northern Limb of the Rustenburg Layered Suite, these intrusions are considered to have evolved separately.

The geographical location of the WP, which is off-craton, and its genetic relationship to the RLS allows for evaluation of the importance of upper crustal contamination in the intrusion. The WP and the RLS have very similar sulfur isotope compositions; yet the WP is hosted by the sediments of the Paleoproterozoic Waterberg Group, which is inferred to have no to minor MIF-S, and the RLS is hosted by the sediments of the Transvaal Supergroup, which has strong MIF-S signatures. This similarity of igneous $\Delta^{33}S$, but difference in host rock $\Delta^{33}S$ argues against assimilation of host rock as the primary explanation of the crustal S signature in the primitive magmas Bushveld Magmatic Province bodies.

6.2.4. Chapter 5

The sub-continental lithospheric mantle (SCLM) is also a potential source for the crustal sulfur, as previous works reported sulfide inclusions in diamonds with a crustal signature. For this study I looked at the peridotite and eclogite xenoliths of the Premier Kimberlite, a younger intrusion that cuts the southern part of the Rustenburg Layered Suite and therefore samples the sulfur underneath the craton.

All of the peridotite and eclogite xenoliths, and the kimberlite matrix itself, yielded sulfur with a $\Delta^{33}S \neq 0$ signature. Given the intense metasomatism experienced by the Premier Kimberlite, the hypothesis that these signatures are related to an open-system behavior between kimberlite and xenolith, or addition of external sulfur has also been considered but eventually discarded, as textural analysis in sulfides from the diverse rock types coupled with the variable $\delta^{34}S$ but near-constant $\Delta^{33}S$, suggest that the composition observed is, in fact, reflecting their composition in the mantle, with a recycled component. However, such assumption cannot be used as a strong evidence for a SCLM-origin for the anomalous sulfur in the RLS.

6.3. Future directions

This thesis has focused on assessing the potential sources of anomalous sulfur in the magmas that formed the Rustenburg Layered Suite. These included the upper crust (Transvaal Supergroup), lower crust, and the sub-continental lithospheric mantle (SCLM). However, particularly for this last reservoir, all the studies published so far have

a qualitative nature, and do not consider other complexities that could potentially support or deny this hypothesis.

Recycling of sulfur is known to occur both in ancient and modern settings (Alt et al., 1993; Metrich et al., 1999; De Hoog et al., 2001; Thomassot et al., 2009; Rielli et al., 2018). Evidence for recycling of ancient sulfur in the early Earth (i.e. a material with anomalous, exogenic sulfur), particularly within the Kaapvaal Craton, has been described (Farquhar et al., 2002; Thomassot et al., 2009; this study). However, despite the evidence that the SCLM below the Bushveld contains recycled sulfur, there are no quantitative models that would account for different isotope systems (e.g. Sr-Nd-Os-O, in addition to S) and how they could have contributed for the Bushveld magma. One important aspect would be to better constrain how the kimberlitic magma interacted with the xenoliths, to assess the usability of the data. One other alternative is to measure these isotope systems in mineral inclusions in diamonds, including silicate minerals, using new techniques that allow for the measurement of small volume. Due to large analytical errors in in-situ measurements of the sulfides, it would not be possible to resolve the small $\Delta^{33}S$ signatures observed in the samples presented in Chapter 5. Processes of addition of S from the devolatilizing slab also have a potential for mobilizing certain PGE (Rielli et al., 2018), and therefore a more in-depth study of the behavior of these elements in xenoliths is warranted.

A reservoir that has not been tested as a possible source of sulfur to the RLS is the asthenospheric mantle, which would imply that the plume itself had a non-zero $\Delta^{33}S$ composition, and could represent recycled material in the deep mantle. One possible way to start tackling this question is by looking at the Bushveld Magmatic Province as a

whole, as all the bodies of this large igneous province should have a genetic connection. However, modern plume-derived magmas that do carry anomalous sulfur have a negative $\Delta^{33}S$ value (Cabral et al., 2013; Delavault et al., 2016), as opposed to the positive values obtained for this study. The $\Delta^{33}S$ of the sulfide inclusions in the SCLM beneath the Kaapvaal Craton also show a heavy bias towards positive values; therefore a connection between positive values and the shallower mantle, affected by devolatilization during subduction processes, needs to be addressed.

The Bushveld Magmatic Province is composed of many igneous bodies besides the Rustenburg Layered Suite, but other than this study, there are no published data for their multiple sulfur isotope composition. These bodies include the Molopo Farms Complex, the Koster Complex, Uitkomst Complex, the Lebowa Granite Suite, and the Phalaborwa Carbonatite Complex.

Initial studies of these other intrusions, in which I have participated, show that all of the intrusions associated with the Bushveld Magmatic Province have a sulfur signature unlike that expected for mantle derived rocks. The Molopo Farms Complex (Feineman et al., in prep), the Uitkomst Complex, and the Lebowa Granite Suite yield a $\Delta^{33}S$ value similar to the RLS and WP. The Phalaborwa Carbonatite Complex has a similar $\delta^{34}S$, but much higher $\Delta^{33}S$ in respect to the RLS (Bolhar et al., in prep), and the Koster Complex has a highly variable $\delta^{34}S$ and $\Delta^{33}S$. In the case of the Koster Complex, there is evidence for intense hydrothermal activity, which potentially mobilized sulfur-bearing fluids from the host rock and completely obliterated the initial sulfur composition. Given that there are significant differences between the evolution of each intrusion, it is important that a

careful study is conducted, aimed at understanding their particularities and evolutionary history.

Appendix A

A.1. Recalculated values of previously published sulfur data

The sulfur isotopic composition of the Rustenburg Layered Suite published in Penniston-Dorland et al. (2012) and Magalhães et al. (2018) was obtained by processing the raw ratio values normalized to the CDT measurements of Wing and Farquhar (2015), a different value of CDT/IAEA-S1 than Chapters 3, 4, and 5 of this thesis. Here, I present the reprocessed, data of both these papers, corrected for the CDT values from Dottin et al., 2018 (Tables A.1 and A.2).

Table A.1. Recalculated sulfur isotope composition of samples described in Penniston-Dorland et al. (2012).

EASTERN LIMB					
	$\delta^{33}S$	$\delta^{34}S$	$\delta^{36}S$	$\Delta^{33}S$	$\Delta^{36}S$
T4011	1.28	2.23	4.14	0.133	-0.096
T4014	1.45	2.56	4.68	0.137	-0.178
T4037	1.70	3.03	5.90	0.138	0.132
T4036	1.47	2.56	4.99	0.147	0.120
T4012	1.46	2.60	4.95	0.124	0.001
T4032	1.80	3.25	6.33	0.123	0.134
T4033	1.48	2.61	4.90	0.138	-0.064
T4039	1.45	2.58	5.06	0.124	0.147
B90-7	1.13	1.89	3.53	0.157	-0.069
WESTERN LIMB					
	$\delta^{33}S$	$\delta^{34}S$	$\delta^{36}S$	$\Delta^{33}S$	$\Delta^{36}S$
B5-c	0.73	1.10	1.99	0.161	-0.094
TL85-1a	0.76	1.22	2.48	0.130	0.163
B7	1.44	2.57	4.64	0.120	-0.246
B85-9	1.09	1.79	3.36	0.173	-0.043
N6.2	0.95	1.55	3.65	0.152	0.707
BHTv1.1	0.86	1.36	2.94	0.157	0.363

Table A.2. Recalculated sulfur isotope composition of samples described in Magalhães et al. (2018)

Sample	$\delta^{33}S$	$\delta^{34}S$	$\delta^{36}S$	$\Delta^{33}S$	$\Delta^{36}S$
DT28 909.1	1.694	3.009	4.828	0.145	0.029
B90-01	1.632	2.877	4.572	0.151	0.024
TW477 660	0.861	1.479	2.157	0.100	0.268
B-4	0.941	1.586	2.120	0.124	0.027
MP24D2	0.993	1.581	1.937	0.179	-0.146
B06-026	0.749	1.159	0.956	0.153	-0.325
DT28 847.2	0.910	1.487	1.687	0.144	3.007
DT28 904.7	0.819	1.329	1.758	0.135	3.448
DT28 910.3	0.876	1.490	1.932	0.109	0.021
LZ10-02	1.243	2.243	3.217	0.088	-0.126
B07-039	0.846	1.358	1.606	0.147	-0.181
B10-042	0.807	1.214	1.109	0.182	-0.278
TW477 440.57	0.330	0.489	-0.139	0.079	-0.148
B06-060	0.653	0.946	0.330	0.166	-0.547
B07-018	1.062	1.767	2.358	0.153	-0.078
B10-054	1.136	1.883	2.479	0.167	-0.179
B06-061	-0.541	-1.284	-3.360	0.120	-0.004
B06-024	0.890	1.446	1.717	0.145	-0.110
B06-011	0.886	1.424	1.671	0.153	-0.114
TW477 202.15	1.066	1.832	2.426	0.123	-0.135
BC16-05D	1.717	3.179	5.075	0.081	-0.049

A.2. Tables with mineral composition of biotite, apatite, sulfide, and sulfate

The mineral chemistry of silicate, sulfide, and sulfate phases was determined using the JEOL 8530F electron probe microanalyzer (EPMA) at the Geophysical Laboratory, Carnegie Institution for Science. The WDS (wave-dispersive X-ray spectroscopy) operating conditions were: accelerating voltage of 15 kV, bean current of 20 nA, and variable beam diameter from 1-5μm, depending on size of the mineral. Analyses reported in this study have compositional totals between 99.5 wt% and 101.5 wt%. The same equipment was used to take backscatter electron (BSE) images. The lower limit accepted for the biotite composition was 94 wt% total, given it is a hydrous mineral. The only sample that yielded viable results was CH7 708.24 (Table A.3). Apatite data is presented in Table A.4. I accepted compositional totals for sulfides (Table A.5) between 98wt% and 102wt%, same totals also were accepted for sulfate (Table A.6).

Table A.3. Mineral composition of biotite from sample CH7 708.24.

Biotite	
n	7
(wt%)	
Na_2O	0.68
MgO	22.18
CaO	0.00
TiO_2	2.24
Al_2O_3	15.81
SiO_2	39.19
FeO	5.11
K_2O	9.14
Total	94.35

Table A.4. Measured apatite composition in samples from the Marginal Zone and Basal Ultramafic Sequence.

Apatite			
(wt%)	CH7 1108	CH7 201	CH7 580
n	10	12	4
F	0.21	0.74	0.15
Na_2O	0.17	0.01	0.26
CaO	54.33	55.83	54.00
SO_3	0.43	0.09	0.13
Cl	4.15	2.28	5.46
SiO_2	0.44	0.32	0.30
Ce_2O_3	0.65	0.25	0.42
P_2O_5	39.69	40.72	39.96
Total	100.07	100.23	100.68

Table A.5. Element composition of sulfides and sulfate. The weight % totals accepted ranged between 98 wt%-102 wt%.

CH7 201.15 - sulfide									
Comment	**001**	**002**	**003**	**004**	**005**	**006**	**007**	**008**	**009**
S	37.97	33.38	34.58	33.19	33.24	39.44	39.54	33.46	34.84
Pb	0.07	0.02	0.04	0.00	0.07	0.00	0.06	0.06	0.04
Fe	60.30	32.71	30.64	32.60	30.01	59.91	59.72	31.03	30.70
Ni	0.19	33.64	0.16	33.24	32.53	0.24	0.13	33.99	0.07
Co	0.06	1.31	0.06	1.36	4.51	0.07	0.07	1.89	0.02
Cu	0.00	0.01	32.57	0.03	0.00	0.00	0.01	0.09	32.49
Zn	0.00	0.05	0.03	0.06	0.00	0.00	0.00	0.02	0.01
Total	98.59	101.11	98.08	100.45	100.36	99.66	99.52	100.55	98.18

Table A.5. (cont.)

CH7 201.15 - sulfide									
Comment	**010**	**011**	**012**	**013**	**014**	**015**	**016**	**017**	**018**
S	33.25	39.45	33.30	33.26	39.17	33.54	39.71	35.26	33.31
Pb	0.03	0.05	0.08	0.02	0.03	0.02	0.10	0.07	0.03
Fe	30.95	59.84	31.86	31.34	60.32	31.75	59.30	30.58	6.20
Ni	33.21	0.10	33.03	33.56	0.27	32.98	0.29	0.04	0.05
Co	2.32	0.08	2.24	2.39	0.09	2.00	0.07	0.03	0.02
Cu	0.44	0.01	0.01	0.00	0.00	0.01	0.03	33.11	0.18
Zn	0.00	0.00	0.00	0.06	0.04	0.01	0.00	0.07	59.67
Total	100.19	99.54	100.52	100.63	99.92	100.31	99.49	99.15	99.46

Table A.5. (cont.)

CH7 201.15 – sulfide					
Comment	**019**	**020**	**021**	**022**	**023**
S	39.72	34.70	33.18	39.13	39.02
Pb	0.07	0.01	0.02	0.05	0.08
Fe	59.23	30.56	30.82	59.85	59.75
Ni	0.10	0.12	33.49	0.22	0.33
Co	0.09	0.03	2.07	0.08	0.12
Cu	0.00	32.70	0.12	0.00	0.00
Zn	0.00	0.05	0.00	0.00	0.00
Total	99.22	98.17	99.68	99.33	99.29

Table A.5. (cont.)

CH7 672.36 - sulfide						
(mass%)	001	002	003	004	005	006
S	52.77	32.96	34.77	32.95	32.86	53.56
Pb	0.10	0.05	0.14	0.01	0.06	0.10
Fe	46.07	30.59	30.10	31.29	27.90	45.39
Ni	0.09	36.30	0.04	33.93	37.25	0.28
Co	0.96	0.19	0.05	0.18	0.17	1.32
Cu	0.02	0.03	32.97	0.37	0.05	0.00
Zn	0.01	0.00	0.00	0.00	0.07	0.00
Total	100.03	100.11	98.06	98.73	98.36	100.66

Table A.5. (cont.)

CH7 970.00 - sulfide									
(mass%)	**001**	**002**	**003**	**004**	**005**	**006**	**007**	**008**	**009**
S	53.36	32.73	53.24	33.34	43.49	33.46	54.26	53.90	33.62
Pb	0.00	0.09	0.11	0.00	0.03	0.01	0.02	0.07	0.09
Fe	45.03	26.96	45.13	31.39	37.88	27.18	45.41	45.95	30.43
Ni	0.22	38.02	0.12	34.67	17.17	38.29	0.35	0.16	33.60
Co	1.21	0.39	0.98	0.26	0.75	0.45	1.14	1.02	0.23
Cu	0.00	0.00	0.90	0.00	0.00	0.21	0.00	0.00	2.30
Zn	0.00	0.03	0.02	0.02	0.04	0.02	0.00	0.02	0.02
Total	99.82	98.23	100.50	99.69	99.36	99.62	101.19	101.12	100.29

Table A.5. (cont.)

CH7 970.00 - sulfide									
(mass%)	**010**	**011**	**012**	**013**	**014**	**015**	**016**	**017**	**018**
S	33.89	54.01	53.70	34.97	35.12	33.05	53.72	35.08	53.84
Pb	0.00	0.04	0.03	0.04	0.00	0.00	0.00	0.01	0.03
Fe	30.13	45.69	46.16	30.08	29.80	28.99	45.33	29.80	45.71
Ni	35.89	0.09	0.39	0.14	0.00	36.71	0.17	0.06	0.02
Co	0.22	1.22	0.72	0.09	0.04	0.66	0.80	0.07	1.20
Cu	0.00	0.00	0.00	33.82	33.70	0.14	0.19	33.58	0.00
Zn	0.02	0.00	0.05	0.01	0.01	0.00	0.01	0.03	0.01
Total	100.16	101.05	101.06	99.13	98.68	99.55	100.23	98.62	100.81

Table A.5. (cont.)

CH7 970.00 - sulfide						
(mass%)	**020**	**021**	**022**	**023**	**024**	**025**
S	33.59	33.89	53.83	53.92	33.33	54.22
Pb	0.00	0.00	0.08	0.10	0.00	0.08
Fe	32.36	30.30	45.82	46.16	29.78	45.40
Ni	34.80	36.00	0.20	0.21	36.51	0.33
Co	0.28	0.40	0.59	0.79	0.22	1.50
Cu	0.09	0.00	0.00	0.00	0.32	0.00
Zn	0.00	0.07	0.01	0.00	0.00	0.01
Total	101.12	100.67	100.53	101.18	100.15	101.55

Table A.5. (cont.)

CH7 1108.46									
(mass%)	**001**	**002**	**003**	**004**	**005**	**006**	**007**	**008**	**009**
S	33.63	53.30	34.82	53.58	35.06	33.36	53.48	33.75	53.84
Pb	0.00	0.06	0.10	0.08	0.02	0.14	0.11	0.06	0.03
Fe	26.25	45.06	29.92	44.88	29.95	25.08	46.23	27.72	44.63
Ni	40.47	0.20	0.04	0.67	0.00	41.23	0.11	17.68	0.26
Co	0.55	1.37	0.05	1.17	0.07	0.29	0.05	0.27	2.11
Cu	0.00	0.34	33.05	0.00	33.14	0.10	0.00	19.75	0.00
Zn	0.00	0.00	0.11	0.01	0.00	0.03	0.00	0.04	0.01
Total	100.90	100.34	98.08	100.39	98.24	100.23	99.98	99.26	100.87

Table A.5. (cont.)

CH7 1108.46									
(mass%)	**010**	**011**	**012**	**013**	**014**	**015**	**016**	**017**	**018**
S	53.68	33.56	33.33	35.48	35.15	53.92	53.70	35.27	33.68
Pb	0.10	0.18	0.02	0.08	0.01	-0.01	0.11	0.09	0.02
Fe	45.84	25.66	25.24	30.21	30.27	45.60	45.68	29.85	25.21
Ni	0.24	41.21	41.78	0.00	0.11	0.44	0.03	0.00	41.26
Co	1.04	0.32	0.22	0.03	0.06	1.04	1.10	0.05	0.29
Cu	0.00	0.16	0.13	32.84	33.20	0.00	0.00	33.13	0.05
Zn	0.00	0.03	0.00	0.05	0.03	0.04	0.01	0.01	0.04
Total	100.90	101.12	100.73	98.68	98.83	101.03	100.63	98.42	100.54

Table A.5. (cont.)

CH7 1108.46 - sulfide					
(mass%)	**019**	**020**	**021**	**022**	**023**
S	33.19	34.91	54.18	34.05	53.70
Pb	0.09	0.02	0.05	0.00	0.08
Fe	24.71	30.33	45.70	26.61	45.63
Ni	41.37	0.20	1.32	34.46	0.30
Co	0.28	0.05	0.14	0.40	0.52
Cu	0.43	33.63	0.00	4.94	0.00
Zn	0.01	0.09	0.08	0.01	0.03
Total	100.09	99.23	101.46	100.47	100.26

Table A.6. Mineral composition for anhydrites from the Basal Ultramafic Sequence.

CH7 970.00 - Anhydrite			CH7 1108.46 - Anhydrite			
wt%	**001**	**002**	**wt%**	**001**	**002**	**003**
Na_2O	0.00	0.00	**Na_2O**	0.02	0.00	0.02
F	0.08	0.00	**F**	0.00	0.01	0.04
MgO	0.01	0.02	**MgO**	0.02	0.03	0.02
SO_3	52.81	55.62	**SO_3**	55.06	54.60	53.77
Cl	0.00	0.00	**Cl**	0.00	0.01	0.00
CaO	48.00	44.71	**CaO**	44.28	45.47	43.87
TiO_2	0.02	0.01	**TiO_2**	0.00	0.00	0.02
SiO_2	0.02	0.06	**SiO_2**	0.10	0.14	0.10
Al_2O_3	0.01	0.00	**Al_2O_3**	0.03	0.02	0.02
FeO	0.07	0.18	**FeO**	0.20	0.42	0.16
MnO	0.00	0.05	**MnO**	0.02	0.02	0.00
Cr_2O_3	0.00	0.00	**Cr_2O_3**	0.02	0.01	0.01
K_2O	0.00	0.00	**K_2O**	0.01	0.00	0.00
P_2O_5	0.12	0.10	**P_2O_5**	0.09	0.12	0.24
SrO	0.04	0.04	**SrO**	0.10	0.06	0.05
Total	101.18	100.73	**Total**	99.92	100.90	98.29

A.3. Compositional Maps

Elemental maps were obtained for xenolith samples using the JEOL 8530F electron microprobe analyzer at Geophysical Laboratory, Carnegie Institution for Science. The elements were measured through a mix of WDS (wave-dispersive X-ray spectroscopy) and EDS (energy-dispersive spectroscopy), depending on the element being analyzed and crystal availability. The run conditions were 15 kV of accelerating energy, 20 nA of voltage, and a beam size of 1 µm. Maps include an anhydrite-apatite pair in sample CH7 1108.46 (Figure A.1), K-feldspar and plagioclase texture (Figure A.2), and intergrown sulfides (Figure A.3). Further descriptions are found in the captions of each figure.

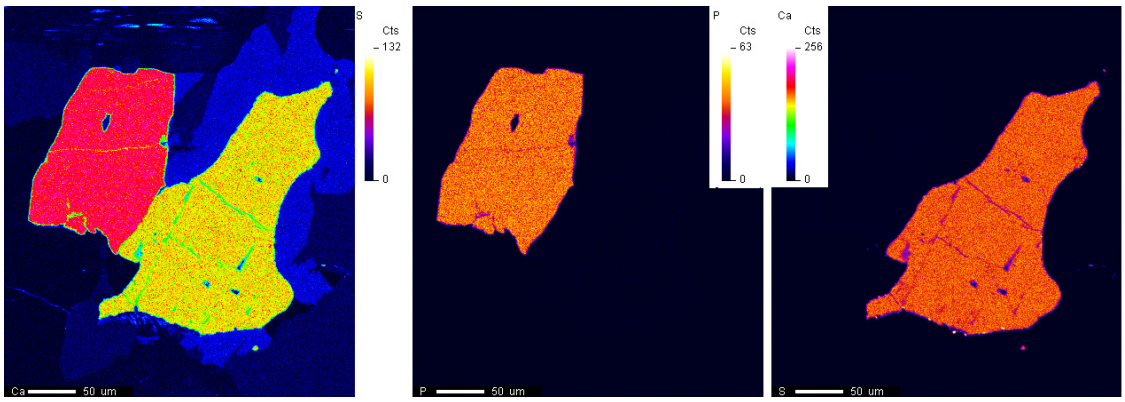

Figure A.1. Sulfur, phosphorus, and calcium compositional maps for apatite-anhydrite pair, confirming their mineral chemistry.

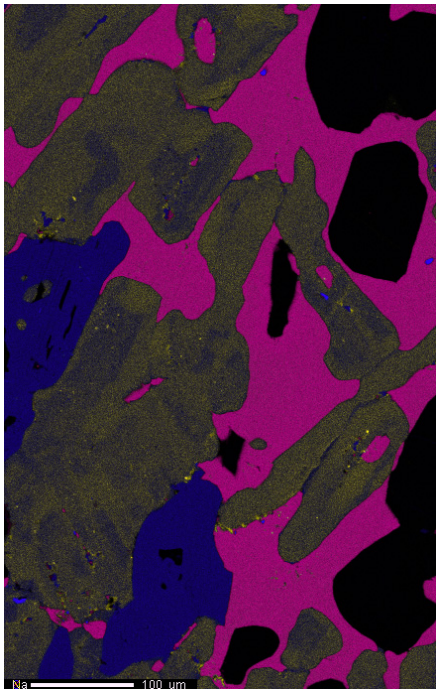

Figure A.2. Mineral composition composite for feldspars in sample CH7 471.78. In pink, K feldspar, blue is clinopyroxene, and in yellow is plagioclase (blue center is Ca-rich and yellow rim is Na-rich).

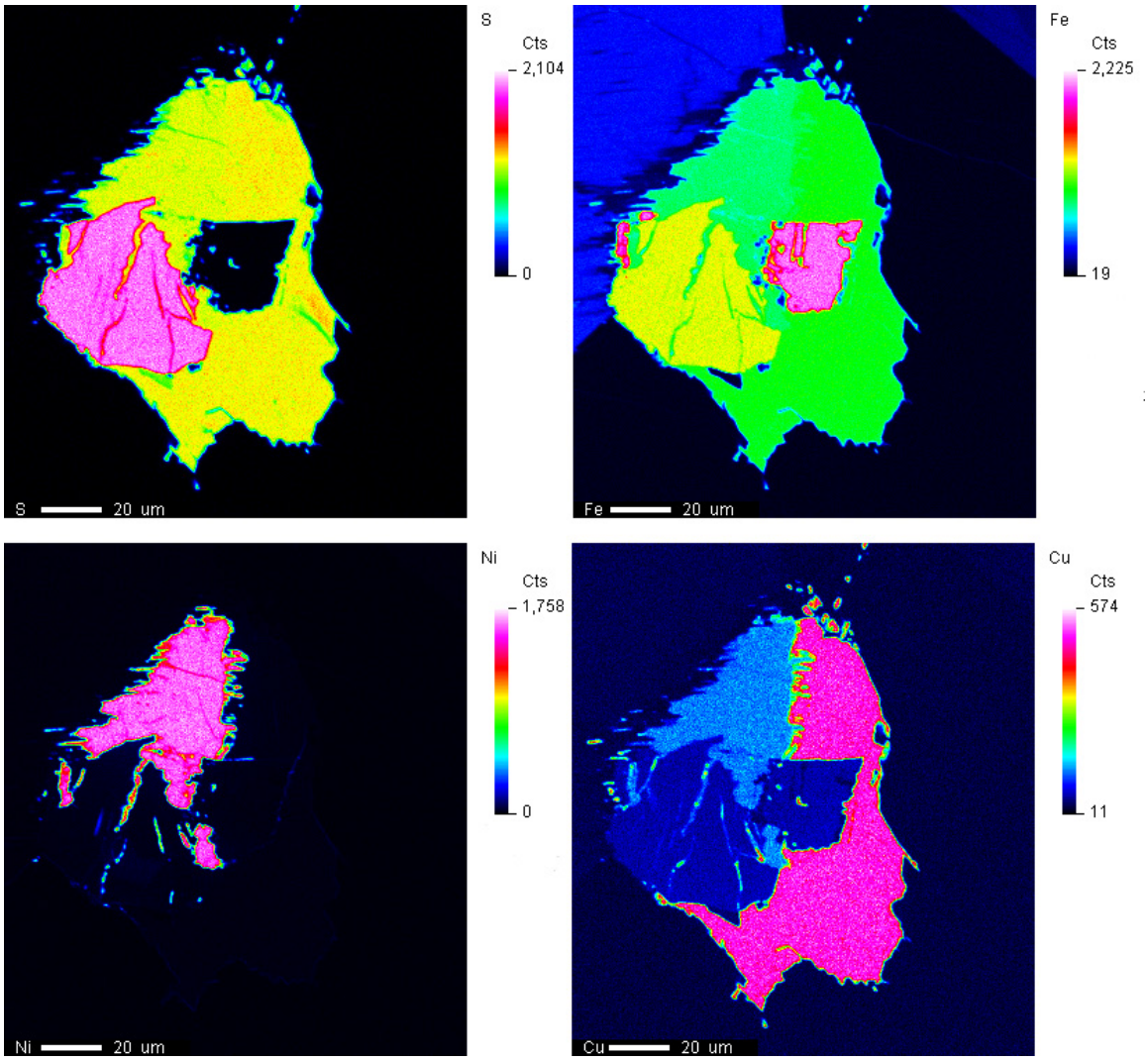

Figure A.3. S-Fe-Ni-Cu maps for sulfide from sample CH7 1108.46. Sulfide texture of sample CH7 1108.46. Pyrrhotite-pentlandite-chalcopyrite assemblage surrounding a grain of magnetite (in the center).

A.4. Backscatter Electron (BSE) Images

This section aims to present textural images that were not possible to include directly in the chapter, but that further illustrate some concepts discussed. All of those

pictures were captured during electron probe microanalysis and were taken using backscattered electrons.

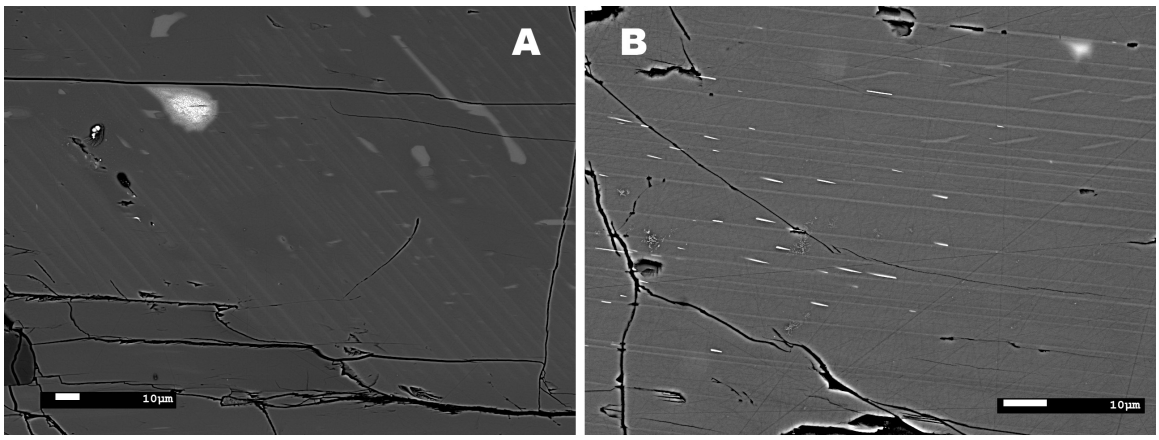

Figure A.4. Both images aim to show the size of exsolution lamellae in many orthopyroxenes of the Clapham Section. While larger lamellae can be seen, many samples have these extremely fine grained, hard to avoid, exsolution lamellae; a) Basal Ultramafic Sequence, sample CH7 970.00; b) Marginal Zone, sample CH7 49.59.

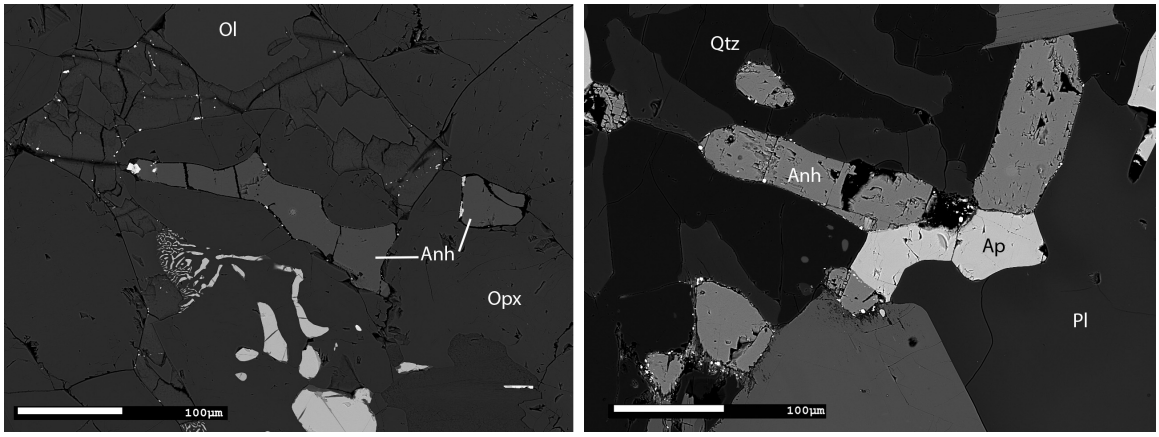

Figure A.5. (left) anhydrite grain in sample CH7 672.36, where it appears in less quantity. One other feature of this sample (not seen in others) is a symplectitic texture between orthopyroxene and iron oxide; **(right)** anhydrite and associated apatite, in sample CH7 1108.

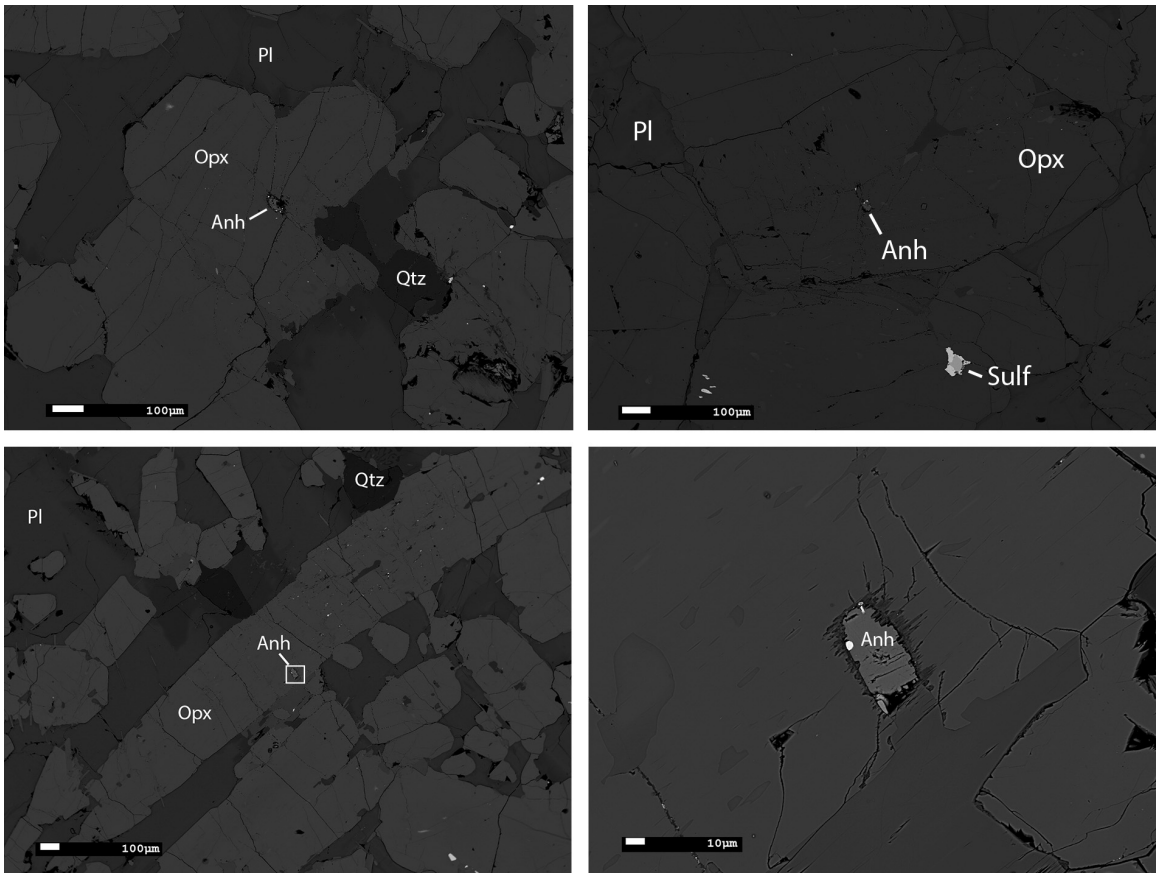

Figure A.6. All images aim to provide further examples of anhydrite grains included in orthopyroxenes, in samples CH7 1108.46 and CH7 970.00, suggesting that anhydrite is an early crystallized phase.

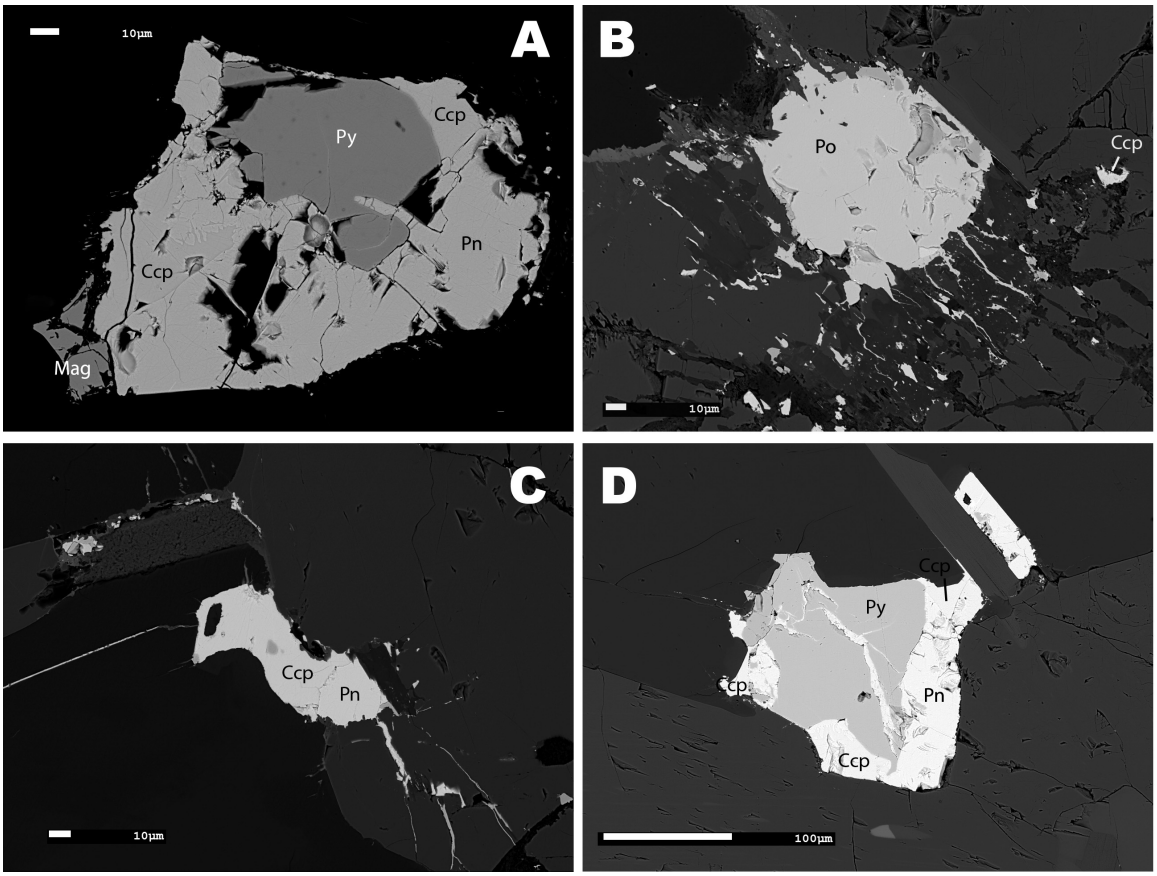

Figure A.7. Two images on the left (A and C) show sulfide textures in the Basal Ultramafic Sequence: association of pyrite+chalcopyrite+pentlandite; image A shows also magnetite associated with this assemblage. On the right (B and D), images of sulfides from Marginal Zone sample CH7 201.15, with evidence for late addition of sulfur ("sulfide veinlets").

Appendix B

B.1. Sample description

The classification of all xenoliths and their sample number is detailed in Table B.1. Samples FRB914, FRB1302, FRB1323, and FRB1359 are listed as classified by Carlson et al. (1999).

Table B.1. List of Premier xenolith samples, with their petrological classification.

Sample	Rock name
FRB1352	Garnet lherzolite
FRB1309	Garnet lherzolite
FRB1375	Spinel harzburgite
FRB1655	Spinel harzburgite
FRB1657	Garnet harzburgite
FRB1331.3	Spinel dunite
FRB1370	Phlogopite dunite
FRB1656	Garnet harzburgite
PHN5247	Spinel harzburgite
PHN5239	Garnet harzburgite
FRB1318	Polymict breccia
FRB1659	Spinel Harzburgite
FRB914	Spinel peridotite
FRB1302	Garnet peridotite
FRB1359	Garnet lherzolite
FRB1323	---
FRB908D2	Eclogite
FRB908D5	Eclogite

B.2. Backscatter Electron (BSE) Images

This section aims to present textural images that were not possible to include directly in the chapter, but that further illustrate some concepts discussed.

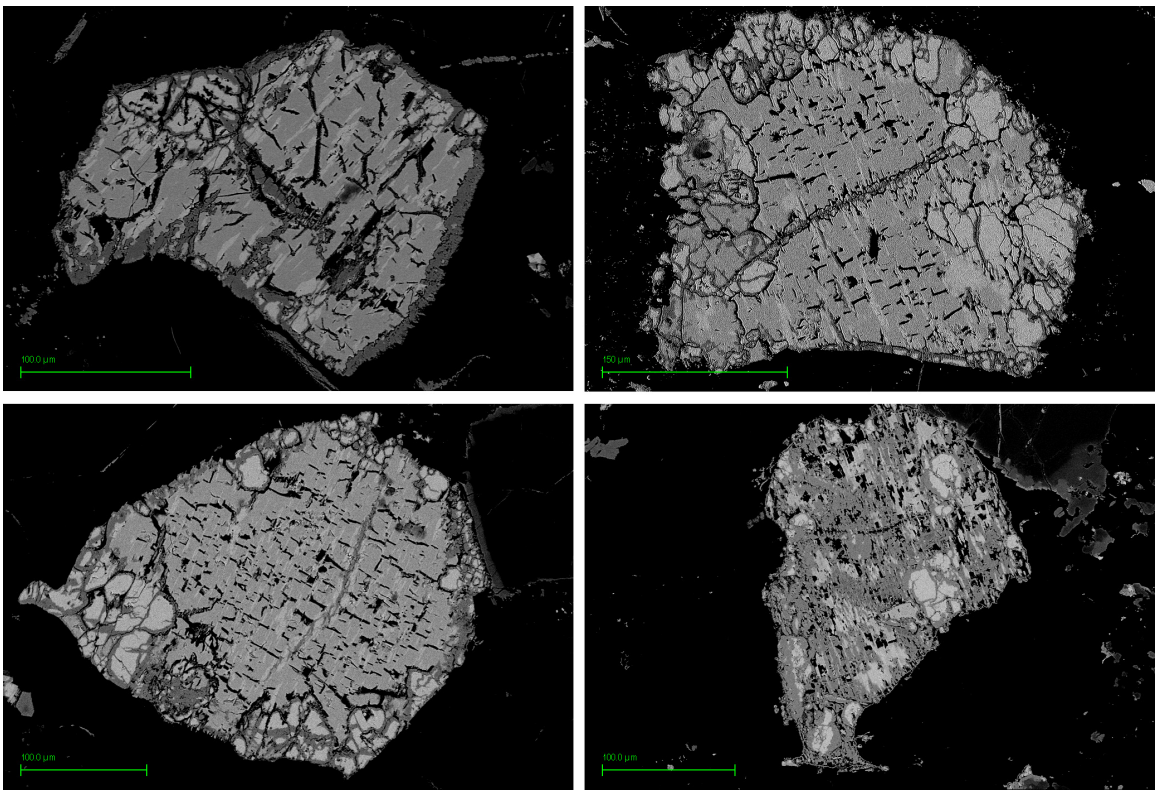

Figure B.1. Four different pyrrhotite-pentlandite pairs from sample PHN5247. Note the different degrees of alteration of sulfides: oxidation reactions and sulfur loss can be inferred from the replacement of sulfide with magnetite.

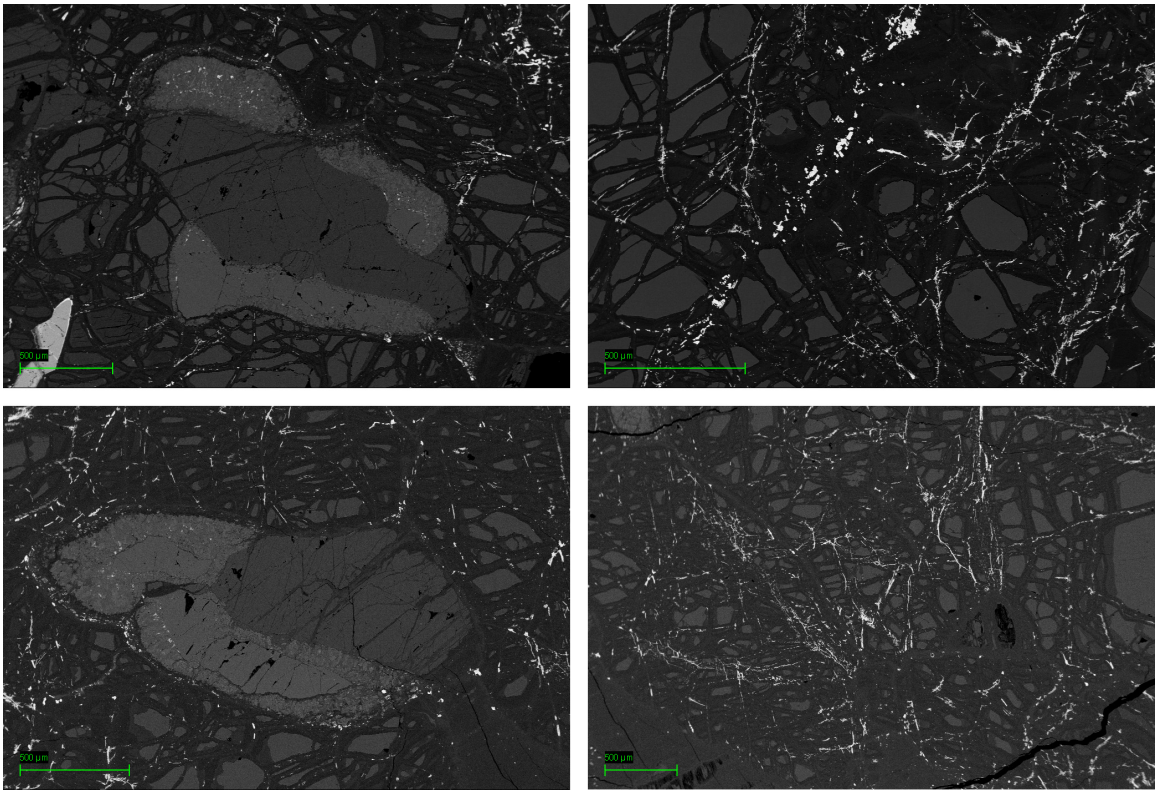

Figure B.2. Textures of sample FRB 1352. Two pictures on the left reflect keliphitic garnet (lighter gray) in contact with orthopyroxene (darker gray). On the right, remnants of olivine grains “wrapped” by serpentine. White material associated to the serpentine zones is magnetite.

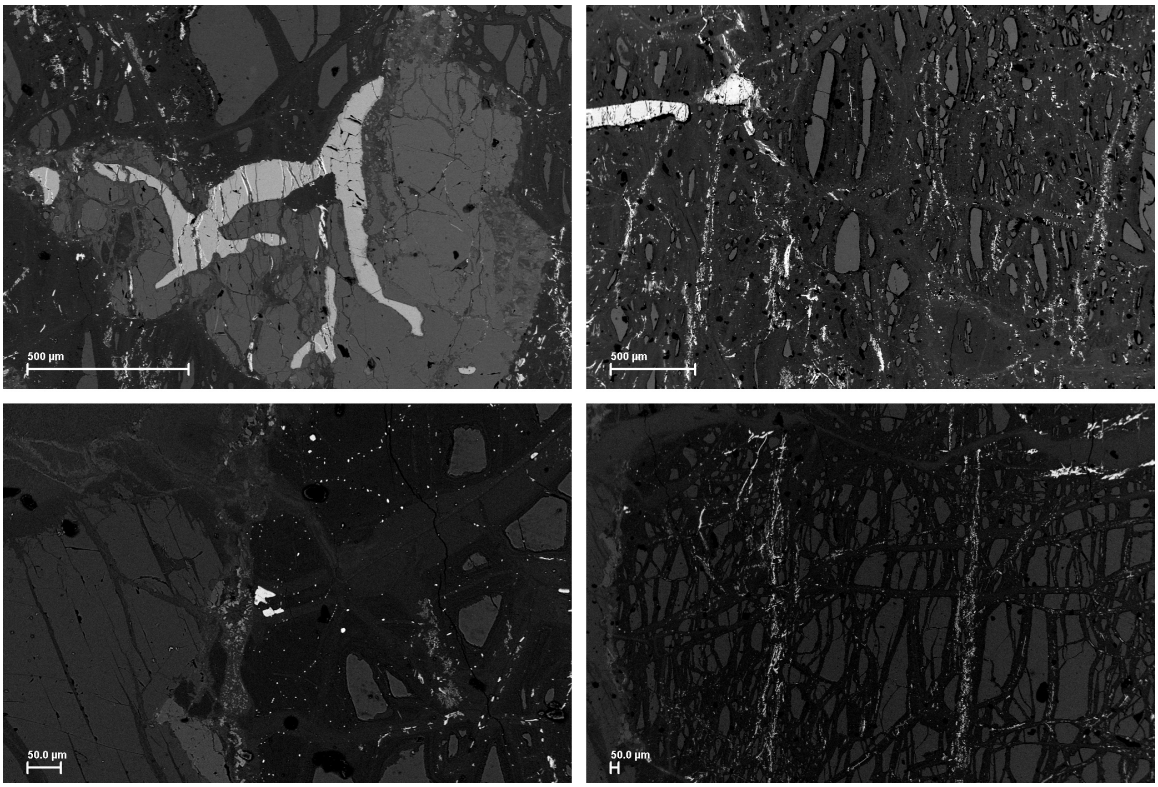

Figure B.3. BSE images from sample FRB1655. The two images on the top show spinel textures (light gray) and how it is found within this rock. The image on the bottom left shows a small sulfide (white) associated with the serpentinized portion. On the bottom right, abundant magnetite (white) can be seen in the serpentinzed portions of the olivine (dark gray).

B.3. Compositional Maps

Elemental maps were obtained for the xenolith samples using the JEOL 8530F electron microprobe analyzer at Geophysical Laboratory at Carnegie Institution for Science. The elements were measured through a mix of WDS (wave-dispersive X-ray spectroscopy) and EDS (energy-dispersive spectroscopy). The run conditions were 15 kV of accelerating energy, 20 nA of voltage, and a beam size of 1 µm. Further descriptions are found in the captions of each figure.

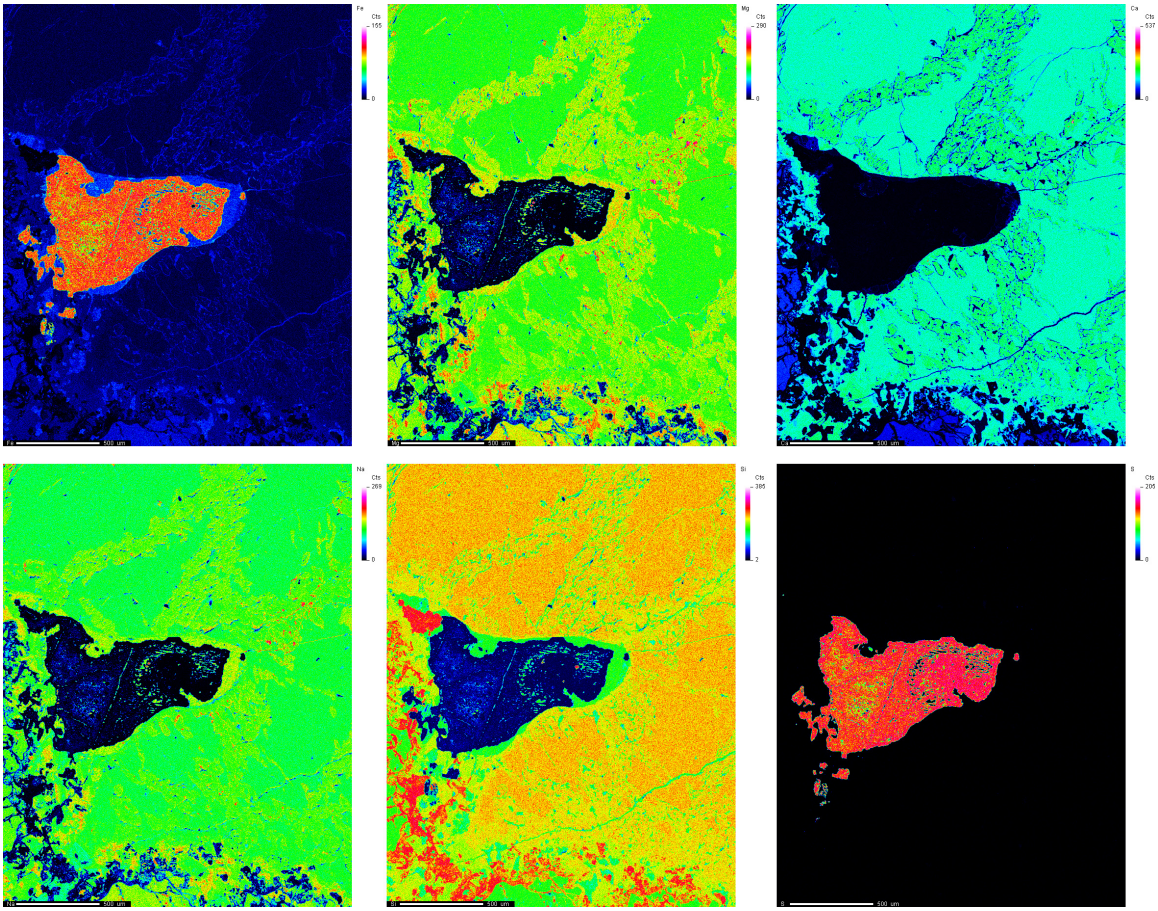

Figure B.4. Fe-Mg-Ca-Na-Si-S maps of the pyrite and associated onphacite in sample FRB 908D2. Inclusions within the pyrite grain have a Na-Al-Si composition. Increase in Fe around the borders of the grain is a possible pseudomorph of original sulfide grain boundaries.

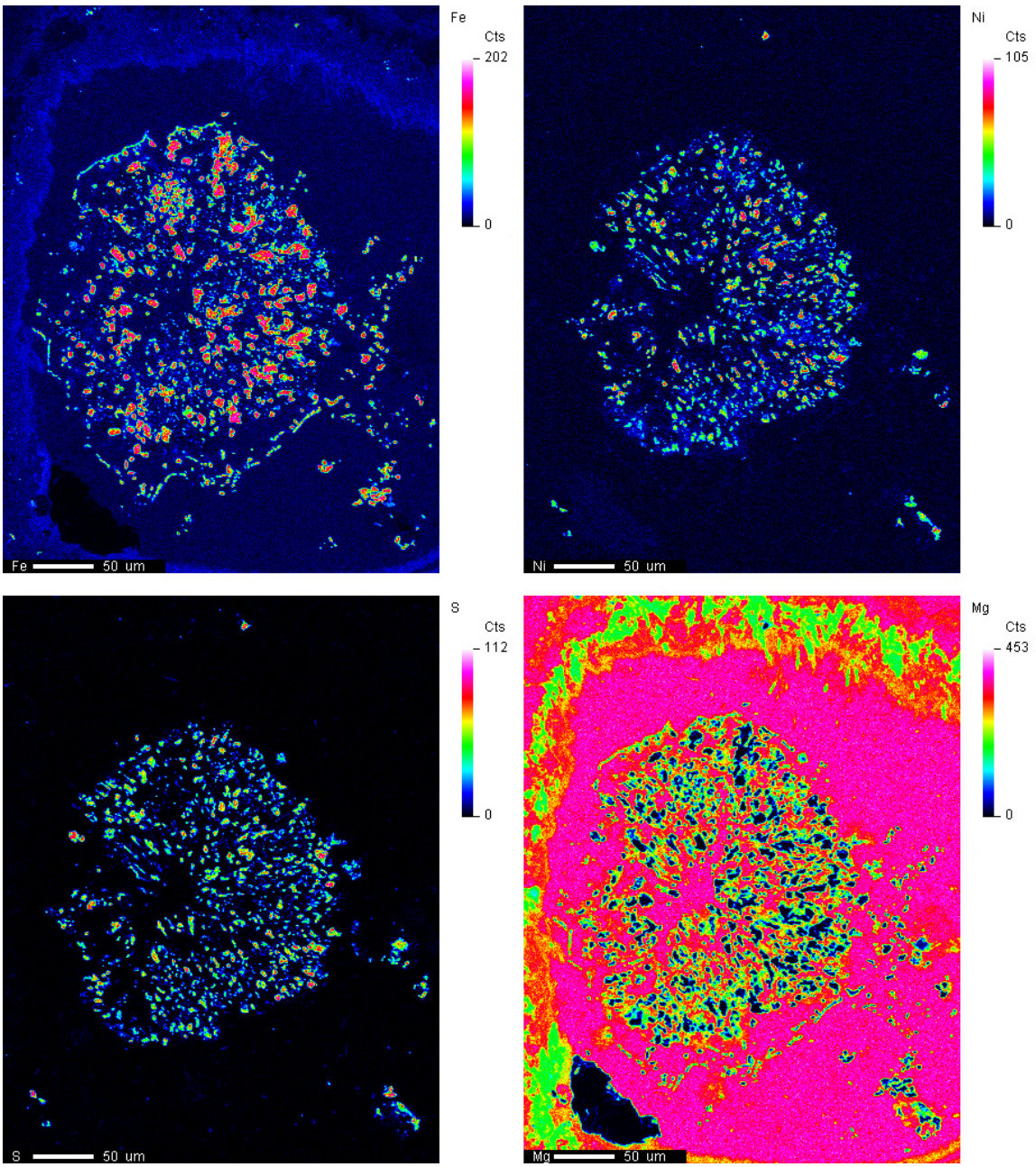

Figure B.5. Fe-Ni-S-Mg compositional map of sulfide grains from sample FRB 1309. It is possible to distinguish a sulfide pseudomorph still composed partly by Fe-Ni sulfides, but mostly overprinted by serpentine.

References

Allsopp, H.L.; Burger, A.J.; Van Zyl, C. 1967. A minimum age for the Premier kimberlite pipe yielded by biotite Rb—Sr measurements, with related galena isotopic data. Earth and Planetary Science Letters, 3: 161-166

Alt, J.C.; Shanks III, W.C.; Jackson, M.C. 1993. Cycling of sulfur in subduction zones: The geochemistry of sulfur in the Mariana Island Arc and back-arc trough. Earth and Planetary Science Letters, 119: 477-494.

Antonelli, M.A.; Kim, S-T.; Peters, M.; Labidi, J.; Cartigny, P.; Walker, R.J.; Lyons, J.R.; Hoek, J.; Farquhar, J. 2014. Early inner solar system origin for anomalous sulfur isotopes in differentiated protoplanets. PNAS, 111: 17749-17754.

Arnold, G.L.; Brunner, B.; Muller, I.A.; Roy, H. 2014. Modern applications for a total sulfur reduction distillation method – what's old is new again. Geochemical Transactions, 15: 1-12.

Bigeleisen, J. and Mayer, M.G. 1947. Calculation of equilibrium constants for isotopic exchange reactions. J. Chem. Phys., 15: 261–267

Boudreau, A.E.; McCallum, I.S. 1992. Concentration of Platinum-Group Elements by Magmatic Fluids in Layered Intrusions. Economic Geology, 87: 1830-1848.

Bryan, S.E. and Ernst, R.E. 2008. Revised definition of Large Igneous Provinces (LIPs). Earth-Science Reviews, 86: 175-202.

Buchanan, D.L.; Suddary, N.P.; Rouse, J.E.; Viljoen, M.J.; Davenport, J.W.J. 1981. The genesis of sulfide mineralization in a portion of the Potgietersrus Limb of the Bushveld Complex. Economic Geology, 76: 568-579.

Buick, I.S.; Maas, R.; Gibson, R. 2001. Precise U-Pb titanite age constraints on the emplacement of the Bushveld Complex, South Africa. Journal of the Geological Society, London, 158: 3-6.

Cabral, R.A.; Jackson, M.G.; Rose-Koga, E.F.; Koga, K.T.; Whitehouse, M.J.; Antonelli, M.A.; Farquhar, J.; Day, J.M.D.; Hauri, E.H. 2013. Anomalous sulphur isotopes in plume lavas reveal deep mantle storage of Archaean crust. Nature, 496: 490-493.

Cameron, E.N. 1978. The Lower Zone of the Eastern Bushveld Complex in the Olifants River Trough. Journal of Petrology, 19: 437-462.

Campbell, H. 2007. Testing the plume theory. Chemical Geology, 241 (2007): 153-176.

Campbell, I.H.; Naldrett, A.J.; Barnes, S.J. 1983, A model for the origin of platinumrich sulphide horizons in the Bushveld and Stillwater Complexes, Journal of Petrology, 24: 133-165.

Canfield, D.E.; Raiswell, R.; Westrich, J.T.; Reaves, C.M.; Berner, R.A. 1986. The use of chromium reduction in the analysis of reduced inorganic sulfur in sediments and shales. Chemical Geology, 54: 149-155.

Carlson, R.W.; Pearson, D.G.; Boyd, F.R.; Shirey, S.B.; Irvine, G.; Menzies, A.H.; Gurney, J.J. 1999. Re-Os systematics of lithospheric peridotites: implications for lithosphere formation and preservation. In Proceedings of the Seventh International Kimberlite Conference. Red Roof Design, Cape Town, South Africa, 99-108.

Carlson, R.W.; Pearson, D.G.; James, D.E. 2005. Physical, chemical, and chronological characteristics of continental mantle. Reviews of Geophysics, 43: 1-24.

Carroll, M.R., Rutherford, M.J., 1987. The stability of igneous anhydrite: experimental results and implications for sulfur behavior in the 1982 El Chichón trachyandesite and other evolved magmas. Journal of Petrology 28, 781–801.

Cawthorn, R.G. and Walraven, F. 1998. Emplacement and crystallization time for the Bushveld Complex. Journal of Petrology, 39: 1669-1687.

Cawthorn, R.G. and Webb, S.J. 2001. Connectivity between the western and eastern limbs of the Bushveld Complex. Tectonophysics, 330: 195-209.

Chaussidon, M.; Sheppard, S.M.F.; Michard, A. 1991. Hydrogen, sulphur and neodymium isotope variations in the mantle beneath the EPR at 12 50'N. Stable isotope geochemistry: A tribute to Samuel Epstein 3, 325.

Coplen, T.B.; Bohlke, J.K.; De Bievre, P.; Ding, T.; Holden, N.E.; Hopple, J.A.; Krouse, H.R.; Lamberty, A.; Peiser, H.S.; Revesz, K.; Rieder, S.E.; Rosman, K.J.R.; Roth, E.; Taylor, P.D.P.; Vocke Jr, R.D.; Xiao, Y.K. 2002. Isotope-abundance variations of selected elements. Pure Appl. Chem. 74(10), 1987-2017.

De Hoog, J.C.M.; Mason, P.R.D.; Van Bergen, M.J. 2001. Sulfur and chalcophile elements in subduction zones: Constraints from laser ablation ICP-MS study of melt inclusions from Galunggung Volcano, Indonesia. Geochimica et Cosmochimica Acta, 65: 3147-3164.

de Kock, M.O.; Ravhura, L.; Vorster, Clarisa; Beukes, N.J.; Gumsley, A.P. 2016. Constraining the timing of the Molopo Farms Complex emplacement and provenance of its country rock. Acta Geologica Sinica (English Edition), 90 (supp.1): 78.

de Waal, S. A.; Maier, W. D.; Armstrong, R. A.; Gauert, C. D. K. 2001. Parental magma and emplacement of the stratiform Uitkomst Complex, South Africa. Canadian Mineralogist, 39: 557-571.

Delavault, H.; Chauvel, C.; Thomassot, E.; Devey, C.W.; Dazas, B. 2016. Sulfur and lead isotopic evidence of relic Archean sediments in the Pitcairn mantle plume. Proceedings of the National Academy of Sciences, 113: 12952-12956.

Dludla, S.; Le Roex, A.P.; Gurney, J.J. 2006. Eclogite xenoliths from the Premier kimberlite, South Africa: geochemical evidence for a subduction origin. South African Journal of Geology, 109: 353-368.

Dottin, J.W.; Farquhar, J.; Labidi, J. 2018. Multiple sulfur isotopic composition of main group pallasites support genetic links to IIIAB iron meteorites.

Drexler, J.W., Munoz, J.L., 1985. Highly oxidized, pyrrhotite–anhydrite-bearing silicic magmas from the Julcani Ag–Cu–Bi–Pb–Au–W District, Peru: physiochemical conditions of a

productive magma. Can. Inst. Mining Conf. on Granite-Related Mineral Deposits: Halifax. September 15–17, 1985. Extended Abstr., 87–100.

Droop, G.T.R. 1987. A general equation for estimating Fe3+ concentrations in ferromagnesian silicates and oxidesfrom microprobe analyses, using stoichiometric criteria. Mineral Magazine, 51: 431-435.

Eglington, B.M. and Armstrong, R.A. 2004. The Kaapvaal Craton and adjacent orogens, southern Africa: a geochronological database and overview of the geological development of the craton. South African Journal of Geology, 107: 13-32.

Eiler, J.M.; Farley, K.A.; Valley, J.W.; Hauri, E.; Craig, H.; Hart, S.R.; Stolper, E.M. 1997. Oxygen isotope variations in oceanic basalt phenocrysts, Geochimica et Cosmochimica Acta, 61: 2281-2293.

Eldrige, D.L.; Guo, W.; Farquhar, J. 2016. Theoretical estimates of equilibrium sulfur isotope effects in aqueous sulfur systems: highlighting the role of isomers in the sulfite and sulfoxylate systems. Geochimica et Cosmochimica Acta, 195: 171-200.

Elkins-Tanton, L.T.; Foulger, G.R.; Natland, J.H.; Presnall, D.C.; Anderson, D.L. (Eds). Plates, Plumes and Paradigms. Geological Society of America Special Paper, 388: 449-462.

Ernst, R.E.; Youbi, N. How Large Igneous Princes affect global climate, sometimes cause mass extinctions, and represent natural markers in the geological record. Palaeogeography, Palaeoclimatology, Palaecology, 478: 30-52.

Evans, B.W., Scaillet, B., 1997. The redox state of Pinatubo dacite and the ilmenite–hematite solvus. American Mineralogist, 82: 625–629.

Evans, K.A., Tomkins, A.G., Cliff, J., Fiorentini, M.L., 2014. Insights into subduction zone sulfur recycling from isotopic analysis of eclogite-hosted sulfides. Chemical Geology, 365:1-19.

Fagereng, A.; Harris, C.; La Grange, M.; Stevens, G. 2008. Stable isotope study of the Archean rocks of the Vredefort impact structure, central Kaapvaal

Farquhar, J.; Bao, H.; Thiemens, M. 2000. Atmospheric influence of Earth's earliest sulfur cycle. Science, 289: 756-758.

Farquhar. J.; Savarino, J.; Airieau, S.; Thiemens, M.H. 2001. Observation of wavelength-sensitive mass-independent sulfur isotope effects during SO2 photolysis: implications for the early atmosphere. Journal of Geophysical Research: Planets 106: 32829-32839.

Farquhar, J.; Wing, B.A.; McKeegan, K.D.; Harris, J.W.; Cartigny P.; Thiemens, M.H. 2002. Mass-independent sulfur of inclusions in diamond and sulfur recycling on early Earth. Science, 298: 2369-2372.

Farquhar, J.; Cliff, J.; Zerkle, A.L.; Kamyshny, A.; Poultron, S.W.; Claire, M.; Adams, D.; Harms, B. 2013. Pathways for Neoarchean pyrite formation constrained by mass-independent sulfur isotopes. PNAS, 110: 17638-17643.

Gauert, C. D. K.; de Waal, S. A.; Wallmach, T. 1995. Geology of the ultrabasic to basic Uitkomst Complex, eastern Transvaal, South Africa: an overview. Journal of African Earth Science, 21: 553–570.

Garuti, G.; Gorgoni, C.; Sighinolfi, G.P. 1984. Sulfide mineralogy and chalcophile and siderophile element abundances in the Ivrea-Verbano mantle peridotites (Western Italian Alps). Earth Planet. Sci. Letters, 70: 69-87.

Giuliani, A.; Phillips, D.; Kamenetsky, V.S.; Fiorentini, M.L.; Farquhar, J.; Kendrick, M.A. 2014. Stable isotope (C, O, S) compositions of volatile-rich minerals in kimberlites: a review. Chemical Geology, 374: 61-83.

Giuliani, A., Fiorentini, M.L., Martin, L.A.J., Farquhar, J., Phillips, D., Griffin, W.L., LaFlamme, C., 2016. Sulfur isotope composition of metasomatised mantle xenoliths from the Bultfontein kimberlite (Kimberley, South Africa): Contribution from subducted sediments and the effect of sulfide alteration on S isotope systematics. Earth and Planetary Science Letters, 445:114-124.

Gregoire, M.; Bell, D.R.; Le Roex, A.P. 2003. Garnet lherzolites from the Kaapvaal Craton (South Africa): Trace element evidence for a metasomatic history. Journal of Petrology, 44: 629-637.

Griffin, W.L.; Batumike, J.; Gréau, Y.; Pearson, N.J.; Shee, S.; O'Reilly, S.Y. 2014. Emplacement ages and sources of kimberlites and related rocks in southern Africa: U-Pb ages and Sr-Nd isotopes of groundmass perovskite. Contributions to Mineralogy and Petrology, 168: 1032.

Gunther, T.; Haase, K.M.; Junge, M.; Oberthur, T.; Woelki, D.; Krumm, S. 2018. Oxygen isotope and trace element compositions of platiniferous dunite pipes of the Bushveld Complex, South Africa – Signals from a recycled mantle component? Lithos, 310-311: 332-341.

Guo, Q.; Strauss, H.; Kaufman, A.J.; Schröder, S.; Gutzmer, J.; Wing, B.; Baker, M.A.; Bekker, A.; Jin, Q.; Kim, S-T.; Farquhar, J. 2009. Reconstructing Earth's surface oxidation across the Archean-Proterozoic transition. Geology, 37: 399-402.

Halevy, I. 2013. Production, preservation, and biological processing of mass-independing sulfur isotope fractionation in the Archean surface environment. PNAS, 110: 17644-17649.

Hammerli, J.; Kemp, A.I.S.; Barrett, N.; Wing, B.A.; Roberts, M.; Arculus, R.J.; Boivin, P.; Nude, P.M.; Rankenburg, K. 2016. Sulfur isotope signatures in the lower crust: A SIMS study on S-rich scapolite of granulites. Chemical Geology 454, 54-66.

Harris, C. and Chaumba, J.B. 2001. Crustal Contamination and Fluid-Rock Interaction during the Formation of the Platreef, Northern Limb of the Bushveld Complex, South Africa. Journal of Petrology, 12: 1321 – 1347.

Harris, C., Pronost, J.J.M., Ashwal, L.D., Cawthorn, R.G., 2005. Oxygen and hydrogen isotope stratigraphy of the Rustenberg Layered Suite, Bushveld Complex: constraints on crustal contamination. Journal of Petrology, 46: 579–601.

Hatton, C.J. 1995. Mantle plume origin for the Bushveld and Ventersdrop magmatic provinces. Journal of African Earth Sciences, 21: 571-577.

Huthmann, F.M., Yudovskaya, M.A., Frei, D., Kinnaird, J.A., 2016. Geochronological evidence for an extension of the Northern Lobe of the Bushveld Complex, Limpopo Province, South Africa. Precambrian Research, 280: 61–75.

Huthmann, F.M.; Kinnaird, J.A.; Yudovskaya, M.A.; Elburg, M.A. 2017. The Sr isotopic stratigraphy of the far Bushveld Complex. Geological Society of South Africa, 120: 499-510.

Huthmann, F.M.; Yudovskaya, M.; Kinnaird, J.A.; McCreesh, M.; McDonald, I. 2018. Geochemistry and PGE of the lower mineralized Zone of the Waterberg Project, South Africa. Ore Geology Reviews, 92: 161-185.

Ickert, R.B.; Stachel, T.; Stern, R.A.; Harris, J.W. 2015. Extreme 18-O enrichment in majorite constrains a crustal origin of transition zone diamonds. Geochemical Perspective Letters, 1: 65-74.

James, D.E.; Fouch, M.J.; VanDecar, J.C.; van der Lee, S.; Kaapval Seismic Group. 2001. Tectospheric structure beneath southern Africa. Geophysical Research Letters, 28: 2485-2488.

Johnston, D. T. 2011. Multiple sulfur isotopes and the evolution of Earth's surface sulfur cycle. Earth-Science Reviews, 106(1-2): 161-183.

Jugo, P.J. 2009. Sulfur content at sulfide saturation in oxidized magmas. Geology, 37: 415-418.

Jugo, P.J.; Luth, R.W.; Richards, J.P. 2005. An experimental study of the sulfur content in basaltic melts saturated with immiscible sulfide or sulfate liquids at 1300ºC and 1.0 Gpa. Journal of Petrology, 46(4): 783-798.

Kamber, B.S.; Blenkinsop, T.G.; Villa, I.M.; Dahl, P.S. 1995. Proterozoic transpressive deformation in the Northern Marginal Zone, Limpopo Belt, Zimbabwe. Geology, 103: 493-508.

Kaufman, A.J.; Johnston, D.T.; Farquhar, J.; Masterson, A.; Lyons, T.W.; Bates, S.; Anbar, A.D.; Arnold, G.L.; Garvin, J.; Buick, R. 2007. Late Archean biospheric oxygenation and atmospheric evolution. Science, 317: 1900-1903.

Kerr, A., Leitch, A.M., 2005. Self-destructive sulfide segregation systems and the formation of high-grade magmatic ore deposits. Economic Geology, 100: 311-32.

Kinnaird, J.A.; Yudovskaya, M.; McCreesh, M.; Huthmann, F.; Botha, T.J. 2017. The Waterberg PGE Deposit – atypical magmatism and mineralisation. Economic Geology, 112, 1367–1394.

Kruger, F.J. 2005. Filling the Bushveld Complex magma chamber: lateral expansion, roof and floor interaction, magmatic unconformities, and the formation of giant chromitite, PGE and Ti-V-magnetitite deposits. Mineralium Deposita, 40: 451-472.

Labidi, J.; Cartigny, P.; Birck, J.L.; Assayag, N.; Bourrand, J.J. 2012. Determination of multiple sulfur isotopes in glasses: A reappraisal of the MORB δ34S. Chemical Geology, 334: 189-198.

Labidi, J.; Cartigny, P.; Moreira, M. 2013. Non-chondritic sulphur isotope composition of the terrestrial mantle. Science, 501: 208-202.

Labidi, J.; Cartigny, P.; Hamelin, C.; Moreira, M.; Dosso, L. 2014. Sulfur isotope budget (32S, 33S, 34S and 36S) in Pacific-Antarctic ridge basalts: a record of mantle source heterogeneity and hydrothermal sulfide assimilation. Geochimica et Cosmochimica Acta, 133: 47-67.

Labidi, J.; Cartigny, P.; Jackson, M.G. 2015. Multiple sulfur isotope composition of oxidized Samoan melts and the implications of a sulfur isotope 'mantle array' in chemical geodynamics. EPSL, 417: 28-39.

Lana, C.; Gibson, R.L.; Kisters, A.; Reimold, W.U. 2003. Archean crustal structure of the Kaapvaal craton, South Africa – evidence from the Vredefort dome. Earth and Planetary Science Letters, 206: 133-144.

Lenhardt, N.; Eriksson, P.; Octavian, C.; Bumby, A. 2012. Nature of and controls on volcanism in the c. 2.35-2.05Ga Pretoria Group, Kaapvaal Craton, South Africa. Precambrian Research, 214: 102-123.

Li C., Ripley E. M., Naldrett A. J., Schnitt A. K. and Moore C. H. 2009. Magmatic anhydrite sulfide assemblages in the plumbing system of the Siberian Traps. Geology, 37: 259–262.

Liu, Y.; Samaha, N-T.; Baker, D.R. 2007. Sulfur concentration at sulfide saturation (SCSS) in magmatic silicate melts. Geochimica et Cosmochimica, 71: 1783-1799.

Lorand, J.P. 1990. Are spinel lherzolite xenoliths representative of the abundance of sulfur in the upper mantle? Geochimica et Cosmochimica Acta, 54: 1487-1492.

Luhr, J.F. 2008. Primary igneous anhydrite: Progress since its recognition in the 1982 El Chichón trachyandesite. Journal of Volcanology and Geothermal Research, 175: 394-407.

Luhr, J.F., Carmichael, I.S.E., Varekamp, J.C., 1984. The 1982 eruptions of El Chichón Volcano, Chiapas, México: mineralogy and petrology of the anhydrite-bearing pumices. J. Volcanol. Geotherm. Res. 23, 69–108.

Magalhães, N.,Penniston-Dorland, S., Farquhar, J., Mathez, E.A. 2018. Variable sulfur isotope composition of sulfides provide evidence for multiple sources of contamination in the Rustenburg Layered Suite, Bushveld Complex. Earth and Planetary Science Letters. 492 163-173.

Maier, W.D.; Arndt, N.T.; Curl, E.A. 2000. Progressive crustal contamination of the Bushveld Complex: evidence from Nd isotopic analyses of the cumulate rocks. Contributions to Mineralogy and Petrology, 140: 316-327.

Maier, W.D.; Peltonen, P.; Juvonenm R.; Pienaar, C. 2005. Platinum group elements in peridotite xenoliths and kimberlite from the Premier Kimberlite pipe, South Africa. South African Journal of Geology, 108: 413-428.

Mathez, E.A. and Waight. 2003. Lead isotopic disequilibrium between sulfide and plagioclase in the Bushveld Complex and the chemical evolution of large layered intrusions. Geochimica et Cosmochimica Acta, 67: 1875-1888.

Matthews, S.J., Sparks, R.S.J., Gardeweg, M.C., 1999b. The Piedras Grandes–Soncor eruptions, Lascar Volcano, Chile: evolution of a zoned magma chamber in the central Andean upper crust. Journal of Petrology, 40: 1891–1919.

Mavrogenes, J.A. and O'Neill, H.StC. 1999. The relative effects of pressure, temperature and oxygen fugacity on the solubility of sulfide in mafic magmas. Geochimica et Cosmochimica Acta, 63: 1173–1180.

McCandless, T.E.; Ruiz, J.; Adair, B.I.; Freydier, C. 1999. Re-Os isotope and Pd/Ru variations in chromitites from the Critical Zone, Bushveld Complex, South Africa. Geochimica et Cosmochimica Acta, 63: 911-923.

McCreesh, M.J.G.; Yudovskaya, M.A.; Kinnaird, J.A.; Reinke, C. 2018. Mineralogical Magazine, 82: 539-575.

McDonough, W.F. & Sun, S.-S. 1995. The Composition of the Earth. Chemical Geology 120, 223-253.

Meisel, T.; Walker, R.J.; Morgan, J.W. 1996. The osmium isotopic composition of Earth's primitive upper mantle. Nature, 383: 517-520.

Métrich, N.; Schiano, P.; Clocchiatti, R.; Maury, R.C. 1999. Transfer of sulfur in subduction settings: an example from Batan Island (Luzon volcanic arc, Philippines). Earth and Planetary Science Letters, 167: 1–14.

Mekhonoshin, A.S.; Ernst, R.; Soderlund, M.A.; Hamilton, M.A.; Kolotilina, T.B.; Izokh, A.E.; Polyakov, G.V.; Tolstykh, N.D. 2016. Relationship between platinum-beating ultramafic-mafic intrusions and large igneous provinces (exemplified by the Siberian Craton). Russian Geology and Geophysics, 57: 822-833.

Mitchell, R.H., and Keays, R.R., 1981. Abundance and distribution of gold, palladium and iridium in some spinel and garnet lherzolites: Implications for the nature and origin of precious metal-rich intergranular components in the upper mantle. Geochimica Cosmochimica Acta, v. 45, p. 2425-2442.

Miyoshi T.; Sakai H.; Chiba H. 1984. Experimental study of sulfur isotope fractionation factors between sulfate and sulfide in high temperature melts. Geochem. J. 18, 75–84.

Muehlenbachs, K. and Clayton, R.N. 1976. Oxygen isotope composition of the oceanic crust and its bearing on seawater. Journal of Geophysical Research, 81: 4365-4369.

Mungall, J.E., Kamo, S.L., McQuade, S., 2016. U-Pb geochronology documents out-of-sequence emplacement of ultramafic layers in the Bushveld Igneous Complex of South Africa. Nature Communications, 7: 13385. DOI: 10.1038/ncomms13385.

Naldrett, A.J.; Wilson, A.H.; Kinnaird, J.A.; Yudovskaya, M.A.; Chunnett, G. 2012. The origin of chromitites and related PGE mineralization in the Bushveld Complex: new mineralogical and petrological constraints.Mineralium Deposita, 47: 209-232.

Nye, C.J., Swanson, S.E., Avery, V.F., Miller, T.P., 1994. Geochemistry of the 1989–1990 eruption of Redoubt Volcano: Part I, whole-rock, major- and trace-element chemistry. Journal of Volcanology and Geothermal Research 62, 429–452

Ono, S.; Eigenbrode, J.L.; Pavlov, A.A.; Kharecha, P.; Rumble II, D.; Kasting, J.F.; Freeman, K.H. 2003. New insights into Archean sulfur cycle from mass-independent sulfur isotope records from the Hamersley Basin, Australia. EPSL, 213: 15-30.

Parat, F., Dungan, M.A., Streck, M.J., 2002. Anhydrite, pyrrhotite, and sulfur-rich apatite: tracing the sulfur evolution of an Oligocene andesite (Eagle Mountain, CO, USA). Lithos 64, 63–75.

Pavlov, A.A. and Kasting, J.F. 2002. Mass-independent fractionation of sulfur isotopes in Archean sediments: strong evidence for an anoxic Archean atmosphere. Astrobiology, 21: 27-41.

Penniston-Dorland, S.C., Wing, B.A., Nex, P.A.M., Kinnaird, J.A., Farquhar, J., Brown, M., Sharman, E., 2008. Multiple sulfur isotopes reveal a primary magmatic origin for the Platreef PGE deposit, Bushveld Complex, South Africa. Geology, 36: 979–982.

Penniston-Dorland, S.C.; Mathez, E.A.; Wing, B.A.; Farquhar, J.; Kinnaird, J.A. 2012. Multiple sulfur isotope evidence for surface-derived sulfur in the Bushveld Complex. Earth and Planetary Science Letters, 337-338: 236-242.

Peters, M.; Strauss, H.; Farquhar, J.; Ockert, C.; Eickmann, B.; Jost, C.L. 2010. Sulfur cycling at the Mid-Atlantic Ridge: a multiple sulfur isotope approach. Chemical Geology, 269: 180-196.

Richards, M.A.; Duncan, R.A.; Courtillot, V.E. 1989. Flood basalts and hot-spot tracks; plume heads and tails. Science, 246: 103-107.

Richardson, S.H. and Shirey, S.B. 2008. Continental mantle signature of Bushveld magmas and coeval diamonds. Nature, 453: 910-913.

Rickard, D.; Mussmann, M.; Steadman, J.A. 2017. Sedimentary sulfides. Elements, 13: 117-122.

Rielli, A.; Tomkins, A.G.; Nebel, O.; Raveggi, M.; Jeon, H.; Martin, L.; Ávila, J.N. 2018. Sulfur isotope systematics of metasomatised mantle wedge. EPSl, 497: 181-192.

Ripley, E.M.; Li, C.; Moore, C.H.; Schmitt, A.K. 2010. Micro-scale S isotope studies of the Kharaelakh intrusion, Noril'sk region, Siberia: Constraints on the genesis of coexisting anhydrite and sulfide minerals. Geochimica et Cosmochimica Acta, 74: 634-644.

Sakai, H.; Des Marais, D.J.; Ueda, A.; Moore, J.G. 1984. Concentrations and isotope ratios of carbon, nitrogen, and sulfur in ocean-floor basalts. Geochimica et Cosmochimica Acta, 48: 2433-2442.

Schmitz, M.D.; Bowring, S.A.; de Wit, M.J.; Gartz, V. 2004. Subduction and terrane collision stabilize the western Kaapvaal craton tectosphere 2.9 billion years ago. Earth and Planetary Science Letters, 222: 363-376.

Schoenberg, R., Kruger, F.J., Nägler, T.F., Meisel, T., Kramers, J.D., 1999. PGE enrichment in chromitite layers and the Merensky Reef of the western Bushveld Complex; a Re-Os and Rb-Sr isotope study. Earth and Planetary Science Letters, 172: 49-64.

Selvaraja, V., Fiorentini, M.L., LaFlamme, C.K., Wing, B.A., Bui, T.-H., 2017. Anomalous sulfur isotopes trace volatile pathways in magmatic arcs. Geology, 45: 419-422.

Sharman, E.R.; Penniston-Dorland, S.C.; Kinnaird, J.A.; Nex, P.A.M.; Brown, M.; Wing, B.A. 2013. Primary origin of marginal Ni-Cu-(PGE) mineralization in layered intrusions: Δ33S evidence from the Platreef, Bushveld, South Africa. Economic Geology, 108: 365-377.

Shirey, S.B.; Harris, J.W.; Richardson, S.H.; Fouch, M.J.; James, D.E.; Cartigny, P.; Deines, P.; Viljoen, F. 2002. Diamond genesis, seismic structure, and evolution of the Kaapvaal-Zimbabwe Craton. Science, 97: 1683-1686.

Shu, Q.; Brey, G.P.; Gerdes, A.; Hoefer, H.E. 2013. Geochronological and geochemical constraints on the formation and evolution of the mantle underneath the Kaapvaal Craton: Lu-Hf and Sm-Nd systematics of subcalcic garnets from highly depleted peridotites. Geochimica et Cosmochimica Acta, 113: 1-20.

Smith, C.B.; Clark, T.C.; Barton, E.S.; Bristow, J.W. 1994. Emplacement ages of kimberlite occurrences in the Prieska region, southwest border of the Kaapvaal Craton, South Africa. Chemical Geology, 113: 149-169.

Starostin, V.I.; Sorokhtin, O.G. 2011. A new interpretation for the origin of the Norilsk type PGE-Cu-Ni sulfide deposits. Geoscience Frontiers, 2: 583-591.

Swanson, S.E. and Kearney, C.S. 2008. Anhydrite in the 1989-1990 lavas and xenoliths from Redoubt Volcano, Alaska. Journal of Volcanology and Geothermal Research, 175: 509-516.

Tappe, S.; Dongre, A.; Liu, C.-Z.; Wu, F.-Y. 2018. 'Premier' evidence for prolonged kimberlite pipe formation and its influence on diamond transport from deep Earth. Geology, 46: 843-846.

Thode, H.; Monster, J. Dunford, H. 1961. Sulphur isotope geochemistry. Geochimica et Cosmochimica Acta, 25: 159–174.

Thomassot, E.; Cartigny, P.; Harris, J.W.; Lorand, J.P.; Rollion-Bard, C.; Chaussidon, M. 2009. Metasomatic diamond growth: A multi-isotope study (13C, 15N, 33S, 34S) of sulphide inclusions and their host diamonds from Jwaneng (Botswana). Earth and Planetary Science Letters, 282: 79-90.

Tsai, H.; Shieh, Y,; Meyer, H.O.A. 1979. Mineralogy and 34S/32S ratios of sulfides associated with kimberlite, xenoliths and diamonds F.R. Boyd, H.O.A. Meyer (Eds.), The Mantle Sample. 2nd International Kimberlite Conference, American Geophysical Union, Washington, DC: 87-103

Turro, N.J. 1983. Influence of nuclear spin on chemical reactions: magnetic isotope and magnetic field effects (a review). Proceedings of the National Academy of Sciences, 80: 609-621.

Urey, H.C. 1947. The thermodynamic properties of isotopic substances, J. Chem. Soc.: 562-581.

VanTongeren, J.A.; Mathez, E.A.; Kelemen, P.B. 2010. A felsic end to Bushveld differentiation. Journal of Petrology, 51: 1891-1912.

VanTongeren, J.A. and Mathez, E.A. 2013. Incoming Magma Composition and Style of Recharge below the Pyroxenite Marker, Eastern Bushveld Complex, South Africa. Journal of Petrology, 5: 1585–1605.

VanTongeren, J.A., Zirakparvar, N.A, Mathez, E.A. 2016. Hf isotopic evidence for a cogenetic magma source for the Bushveld Complex and associated felsic magmas. Lithos, 248-251: 469-477.

Viljoen, F.; Dobbe, R.; Smit, B. 2009. Geochemical processes in peridotite xenoliths from the Premier diamond mine, South Africa: Evidence for the depletion and refertilisation of subcratonic lithosphere. Lithos, 112: 1133-1142.

Vinogradov, V.I. and Ilupin, I.P. 1972. Isotope compositions of sulfur in kimberlites of the siberian Platform Dokl. Acad. Sci. USSR, 201: 221-223

Wagner, P. 1929. The platinum deposits and mines of South Africa. Edinburgh, Oliver and Boyd, 326p.

Walraven, F. 1997. Geochronology of the Rooiberg Group, Transvaal Supergroup, South Africa. Economic Geology Research Unit, University of Witwatersrand, Information Circular 316.

Walter, M.J.; Kohn, S.C.; Araujo, D.; Bulanova, G.P.; Smith, C.B.; Gaillou, E.; Wang, J.; Steele, A.; Shirey, S.B. 2011. Deep mantle cycling of oceanic crust: evidence from diamonds and their mineral inclusions. Science, 334: 54-57.

White, W.M. 2015. Isotopes, DUPAL, LLSVPs, and Anekantavada. Chemical Geology, 419: 10-28.

Wignall, P.B. 2001. Large igneous provinces and mass extinctions. Earth-Science Reviews, 53: 1-33.

Wilson, A.H., 2012. A chill sequence to the Bushveld Complex: Insight into the first stage of emplacement and implications for the parental magmas. Journal of Petrology, 53: 1123-1168.

Wilson, A.H.; Zeh, A.; Gerdes, A. 2017. In Situ Sr isotopes in plagioclase and trace element systematics in the Lowest Part of the Eastern Bushveld Complex: Dynamic processes in an evolving magma chamber. Journal of Petrology, 58: 327-360.

Wing, B.A. and Farquhar, J. 2015. Sulfur isotope homogeneity of lunar mare basalts. Geochimica et Cosmochimica Acta, 170: 266-280.

Wu, F-Y.; Mitchell, R.H.; Li, Q.-L.; Sun, J.; Liu, C.-Z. Yang, Y.-H. 2013. In situ U-Pb age determination and Sr-Nd isotopic analysis of perovskite from Premier (Cullinan) kimberlite, South Africa. Chemical Geology, 252: 83-95.

Yudovskaya, M.A.; Sluzhenikin, S.F.; Costin, G.; Shatagin, K.N.; Dubinina, E.O.; Grobbler, D.F.; Ueckermann, H.; Kinnaird, J.A. 2018. Society of Economic Geology, 21: 177-206.

Zeh, A.; Ovtcharova, M.; Wilson, A.H.; Schaltegger, U. 2015. The Bushveld Complex was emplaced and cooled in less than one million years – results of zirconology, and geotectonics implications. EPSL, 418: 103-114.

Zirakparvar, N.A.; Mathez, E.A.; Scoates, J.S.; Wall, C.J. 2014. Zircon Hf isotope evidence for an enriched mantle source for the Bushveld Igneous Complex. Contributions to Mineralogy and Petrology, 168: 1050.